

**Design and Implementation of Observers for DFIG based Wind Energy
Conversion Systems**



Mridul Kanti Malakar



Design and Implementation of Observers for DFIG based Wind Energy Conversion Systems

A

Thesis submitted

for the award of the degree of

Doctor of Philosophy

by

Mridul Kanti Malakar



Department of Electronics and Electrical Engineering

Indian Institute of Technology Guwahati

Guwahati -781039, Assam, India

October 2019



Dedicated to

To

My Supervisors

Dr. Praveen Tripathy

and

Dr. Srinivasan Krishnaswami

and

To

My dear **parents,**

my sister for their love and support



Certificate

This is to certify that the thesis entitled “**Design and Implementation of Observers for DFIG based Wind Energy Conversion Systems**”, submitted by **Mridul Kanti Malakar** (10610217), a research scholar in the *Department of Electronics and Electrical Engineering, Indian Institute of Technology Guwahati*, for the award of the degree of **Doctor of Philosophy**, is a record of an original research work carried out by him under my supervision and guidance. The thesis has fulfilled all the requirements as per the regulations of the institute and in my opinion has reached the standard needed for submission. The results embodied in this thesis have not been submitted to any other University or Institute for the award of any degree or diploma.

Date:

Place: Guwahati.

Dr. Praveen Tripathy

Associate Professor

Dept. of Electronics and Electrical Engg

Indian Institute of Technology Guwahati

Guwahati - 781 039, Assam, India.

Date:

Place: Guwahati.

Dr. Srinivasan Krishnaswami

Assistant Professor

Dept. of Electronics and Electrical Engg

Indian Institute of Technology Guwahati

Guwahati - 781 039, Assam, India.



Acknowledgements

I wish to thank Dr. Praveen Tripathy and Dr. Srinivasan Krishnaswamy for accepting me as a research student in the area of Wind Energy Conversion System based on Doubly Fed Induction Generator. I thank my supervisor, Dr. Praveen Tripathy, for his excellent guidance and research motivation of practical relevance. I thank my co-supervisor Dr. Srinivasan Krishnaswamy, for his outstanding guidance to solve mathematical problems in the research area. I consider myself fortunate to work under them. I thoroughly enjoyed working on this project. I wish to acknowledge their inspiring guidance, continuous support and encouragement during the research work.

I would like to express my heartfelt thanks to my doctoral committee members Prof. Somnath Majhi, Dr. Ravindranath Adda and Dr. Sisir Kumar Nayak for sparing their precious time to evaluate the progress of my work. Their suggestions have been valuable.

I would also like to thank the Head of the Department and the other faculty members for their kind help in carrying out this work. I am also grateful to all the members of the research and technical staff of the department without whose help I could not have completed this thesis. My special thanks to Mr. Sanjib Das for maintaining the excellent computing facility and various resources useful for this work. I am also thankful to Mr. Ridib Bharali, Mr. Sidananda Sonowal and Mr. Dimpul Gogoi for supporting in my experimental work.

I would like to thank my colleagues, friends and juniors for their cordial assistance and lively working environment in the lab. I also wish to express my appreciation to all the research scholars of the Power and Control Laboratory as well as Electrical Machine Laboratory IIT Guwahati, for their co-operation.

I take this opportunity to acknowledge the exhaustive support and encouragement extended to my parents, sister and brother-in-law.

Mridul Kanti Malakar



Abstract

The need for energy has increased dramatically throughout the world in recent years. Renewable energy sources such as wind, solar, geothermal, biomass, etc. play a significant role in the sustainable generation of electric power for nations all around the world. Among the various renewable energy resources, the generation of power from wind energy is considered to be more friendly to the environment. The forecast for the installed capacity of the wind energy-based power system for the world is about 839 GW by 2023. Currently, most of the wind energy system in India and the world uses fixed speed type of generators. These fixed speed wind energy conversion system has low energy conversion efficiency when operated under variable wind speed. Moreover, there is a need to have a wind energy conversion system that can support the grid by supplying reactive power and actively participate in frequency regulation of the grid.

In order to extract maximum possible energy from the wind, efficient technologies, such as variable speed constant frequency (VSCF) wind energy conversion system (WECS) are needed. The commonly used variable speed generators are doubly-fed induction generator (DFIG), permanent magnet synchronous generator and synchronous reluctance generator. Among these, the DFIG is the preferred for WECS due to its low maintenance and installation cost, and robustness. Furthermore, DFIG offers various features such as four quadrant active and reactive power control, low converter cost, variable speed operation ($\pm 33\%$ slip speed variation). The controllers for DFIGs are quite complex, and accurate estimation of rotor position and speed plays a significant role in improving the performance of the controller for sensorless operation.

The instantaneous position of the rotor with respect to the stator is required for decoupled control of active and reactive power. In conventional field oriented control schemes, the

instantaneous rotor position is estimated by using an absolute encoder fitted to the shaft. A high-resolution position encoder is very expensive as well as reduces system reliability. However, in a DFIG based wind turbine system, the mounting of an encoder is not an easy task. The encoder must be mounted in such a way that the angle between rotor and stator axis can be accessed directly. Sensorless control strategies are usually used to estimate the DFIG flux and rotor position using observer design, which reduces the cost, size, and maintenance of the drive system. Due to the nonlinearity of the wind turbine dynamics and stochastic behavior of the wind, it is not so simple to estimate the rotor position and machine flux over a wide variation of slip. Sensorless control techniques use a model of a DFIG in the synchronous reference frame. Hence, there is a need to transfer the variables to this reference frame. This requires an accurate estimate of the slip position of the rotor or rotor angle. Several estimation techniques, such as flux-based observer and current-based model reference adaptive system (MRAS) observer, high-frequency injection, etc., have been introduced in literature. They have their own advantages and limitations. Rotor flux based MRAS observers show with poor performance when operated close to synchronous speed. This is due to low-level excitation from the rotor side. Stator flux based MRAS observer, on the other hand, comes with inherent integration drift problems.

Similarly, stator current based MRAS observers drift to unstable operation when the magnitude of stator current is low. Hence, the accuracy of such observers depends on the load connected to the system, i.e., it gives a more erroneous estimation of rotor position under no-load or light load connected to the system. Whereas, the rotor current based MRAS observer is affected by the variation of parameters, such as stator inductances, and mutual inductances, etc. The present thesis is mainly focused on developing algorithms to mitigate the above limitations.

The present thesis work is focused on the design and hardware implementation of robust observers for the slip position and speed of DFIG. The first estimator described in this thesis is a predictor-corrector based closed-loop rotor slip-position estimator is one of

the techniques. This method utilizes measured values of the stator voltage, stator current, rotor current, and rotor speed. Further, an analysis of its stability and the range of gain for its convergence is discussed. The next proposed estimator is a new closed-loop adaptive speed and slip position observer (ASSPE) for a standalone DFIG system. This method uses the measured value of the stator voltages, stator currents and rotor currents. The proposed ASSPE requires less number of DFIG parameters as compared to the model-based observers. The turns ratio and stator leakage inductance are considered to improve the estimation accuracy. This method avoids the stator and rotor flux estimation. Further, a new robust two-stage observer is proposed to mitigate the effects of sudden changes in speed and load, parametric uncertainty, and noise. The proposed observer estimates the rotor slip position and speed of the DFIG accurately. Finally, Extended Kalman Filter (EKF) based observer is proposed. This estimator uses an augmented state model to estimate the rotor position and speed accurately for a grid-connected DFIG system.

The aim of the research work presented in this thesis is to model, develop and implement slip position and speed observers. The developed observers are robust to load and speed disturbances, parametric uncertainties, model errors, noise interference, and estimation errors. The performance of these observers are verified through simulation and hardware implementation.



Contents

List of Figures	xxi
List of Tables	xxv
List of Acronyms	xxvii
List of Symbols	xxix
1 Introduction	1
1.1 Introduction	2
1.2 Types of Generator Configurations for WECS	3
1.3 DFIG Based Wind Energy Conversion Systems	4
1.4 Stand-alone Generators with Doubly-fed Configuration	5
1.4.1 DFIG Configuration and Modes of Operation	6
1.5 Literature Review	8
1.6 Motivation and Objective	10
1.7 Thesis Organization	12
2 Stator Flux Based Slip Angle Estimation	15
2.1 Introduction	16
2.2 Mathematical Model of DFIG	16
2.3 Rotor Slip-position Estimation Technique	17
2.4 Stability Analysis	19
2.5 Simulation Results	21
2.5.1 Case 1: Speed Change Response	23
2.5.2 Case 2: Load Change Response	27
2.6 Experimental Results:	27

2.6.1	Case 1: Constant Rotor Speed Operation	29
2.6.2	Case 2: Step Change in Speed Reference	29
2.6.3	Case 3: Sudden Change in Load Connected to the Stator Terminal	29
2.7	Conclusion	29
3	Robust Slip Angle Speed Estimation Technique Using the Measurement of Rotor Current	33
3.1	Introduction	34
3.2	Stator Voltage Oriented Reference Frame	34
3.3	Proposed Estimation Method	35
3.3.1	Rotor Slip Angle Estimation	35
3.3.2	Rotor Speed Estimation	41
3.4	Stability Analysis	44
3.5	Simulation Results	47
3.5.1	Case 1: Step Change in Reference Input Speed	47
3.5.2	Case 2: Step Changes in the Load Connected at the Stator Terminal	51
3.5.3	Case 3: Mutual Inductance Variation	56
3.6	Experimental Results	60
3.6.1	Case 1: Sub-synchronous Operation Response	60
3.6.2	Case 2: Speed Change Operation Response	62
3.6.3	Case 3: Load Change Operation Response	64
3.7	Conclusion	66
4	Robust Slip Angle and Speed Observer for Sensorless Operation of a DFIG: An LMI Approach	67
4.1	Introduction	68
4.2	Model and Standalone Operation of DFIG	68
4.3	Proposed Estimation Method	69
4.3.1	Rotor Current Observer	70
4.3.2	Slip Position and Slip Speed Observer	75

4.4	Results and Discussion	79
4.4.1	Simulation Results	79
4.4.1.1	Case 1: Step Change in Reference Input Speed	79
4.4.1.2	Case 2: Step Changes in the Load	83
4.4.2	Experimental Results	83
4.4.2.1	Case 1: Constant Rotor Speed Operation	86
4.4.2.2	Case 2: Change of the Operating Mode of the System from Super-synchronous to Sub-synchronous	88
4.4.2.3	Case 3: Operation in Sudden Load Change	89
4.5	Conclusion	90
5	State Estimation of DFIG using an Extended Kalman Filter with an Augmented State Model	91
5.1	Introduction	92
5.2	Extended Kalman Filter	92
5.3	Augmented State Model of DFIG	94
5.4	Simulation Results	96
5.4.1	Case 1: Operation at Constant Speed Reference	96
5.4.2	Case 2: Step Change of Speed Reference in Super-synchronous Mode	98
5.4.3	Case 3: Short Circuit of Stator Terminals at Super-synchronous Speed	98
5.4.4	Case 4: Step Change of Speed Reference from Super-synchronous to Sub-synchronous Mode	98
5.4.5	Case 5: Step Reduction of Turbine Torque Reference	99
5.5	Conclusion	102
6	Conclusion and Future Works	103
6.1	General	104
6.2	Summary of Important Findings	104
6.3	Scope of Future Research Work	106

A	Power Circuit Components and Specifications	109
A.1	Specification of Slip Ring Induction Machine	110
A.2	DFIG Parameters	110
A.3	Power Converters	110
A.3.1	Power Device:	110
A.3.2	Driver:	110
A.3.3	DC-link Capacitor:	111
A.4	Sensors and Signal Conditioning	111
A.4.1	Current Sensor:	111
A.4.2	Voltage Sensor:	111
A.4.3	Signal Conditioning & Sensor Interface Circuit:	111
A.5	Microcontroller:	111
A.6	Grid Filter:	112
A.7	DC Motor:	112
A.8	Starting Procedure for PSCAD/EMTDC Software Based Developed DFIG System	112
A.9	Starting Procedure for Laboratory Based Developed DFIG System	112
A.10	Experimental Setup	114
B	DFIG Model in Different Reference Frame	115
B.1	Reference Frame Transformation	116
B.2	Synchronous Reference Frame Phase Locked Loop (SRFPLL)	120
B.3	DFIG Model in α - β Reference Frame	121
B.4	DFIG Model in $d - q$ Reference Frame	123
B.5	Design of Low Pass Filter as an integrator	124
C	Calculation of DC-Link Capacitor	127
C.1	Calculation of DC-link Capacitor	128
D	Nonlinear Variable Speed Variable Pitch Wind Turbine System	131
D.1	Nonlinear Variable Speed Variable Pitch Wind Turbine System	132

Bibliography	133
List of Publications	138





List of Figures

1.1	Types of wind energy system configurations.	3
1.2	DFIG based wind energy conversion system	5
1.3	DFIG Configuration.	6
1.4	Power flow schematic diagram for all modes of operation of the DFIG system (neglecting losses).	7
2.1	Block diagram of the DFIG system with closed loop proposed predictor-corrector based observer	22
2.2	Speed profile of DFIG	23
2.3	Starting response of the algorithm: (a) Estimated rotor slip position, (b) Slip position estimation error plot during starting at 1400 RPM.	24
2.4	Speed reference changes from sub synchronous to super synchronous range	24
2.5	Speed change: (a) Slip position during sub synchronous to super synchronous speed variation, (b) The estimation error plot for speed change to supersynchronous from subsynchronous.	25
2.6	Speed change: (a) Slip position during super synchronous to sub synchronous speed variation, (b) The estimation error plot for speed change to subsynchronous from supersynchronous.	26
2.7	The estimation error plot during load change	27
2.8	Experimental results for operation at rotor speed of 1351 rpm	28
2.9	Experimental results for speed change from 1470 rpm to 1430 rpm.	30
2.10	Experimental results for load change from 300 Ω to 150 Ω	31

3.1	Angular relations of current and voltage vectors for DFIG.	35
3.2	Schematic block diagram of ASSP Estimator (Adaptive Speed a Slip Position Estimator)	37
3.3	Schematic block diagram of slip position estimator	38
3.4	Schematic block diagram of rotor speed estimator	38
3.5	Plot during step change in reference input speed (a) estimated speed of the DFIG, (b) the corresponding error plot of the estimated speed.	48
3.6	Plot during step change in reference input speed (a) estimated slip position of the DFIG (b) the corresponding error plot in the estimated slip position.	49
3.7	Plot during step change in reference input speed (a) estimated rotor current in ab reference frame, (b) estimated rotor current in xy reference frame.	50
3.8	Per phase resistive load variation connected to the stator terminals.	52
3.9	During load variation, (a) estimated and actual speed, and (b) speed error.	53
3.10	During load variation, (a) estimated slip position and (b) slip position error.	54
3.11	During load variation, (a) estimated and actual rotor current components in ab reference, (b) estimated and actual rotor current components in xy reference.	55
3.12	During L_m variation, (a) estimated speed and (b) speed error	57
3.13	During L_m variation, (a) estimated slip position and (b) slip position error.	58
3.14	During L_m variation, (a) estimated and actual rotor current components in ab reference frame and (b) estimated and actual rotor current components in xy reference frame.	59
3.15	Experiment results of ASSPE and stator flux based PCSPE when DFIG is operating with speed 1384 rpm. (a) Comparison between ASSPE and PCSPE (b) Corresponding stator voltage and current.	61
3.16	The slip position error at constant speed operation at 1384 rpm	62
3.17	Experiment results of ASSPE and stator flux based PCSPE during speed change. (a) Comparison between ASSPE and PCSPE at supersynchronous to subsynchronous speed transition and vice-versa,(b) Corresponding Stator voltage and current.	63
3.18	The slip position error during speed change from super-synchronous to sub-synchronous speed operation and vice-versa.	64

3.19	Experimental results of ASSPE and stator flux based PCSPE during load change. (a) Comparison between flux based observer, (b) Corresponding stator voltage and current.	65
3.20	The slip position error during load change.	66
4.1	Schematic diagram of H_∞ based slip position and slip speed observer for DFIG system.	70
4.2	(a) Structure of the observer with closed loop control of rotor side converter DFIG . .	71
4.3	The proposed structure of the observer for the estimation of slip position and slip speed.	72
4.4	Block Diagram of the Proposed Observer	77
4.5	Reduced block Diagram of the Proposed Observer	78
4.6	(a) Nyquist plot of $G_1(s)$ (b) Nyquist plot of $G_2(s)$	80
4.7	Estimated slip speed	81
4.8	Estimated slip speed error	81
4.9	Estimated slip position	82
4.10	Slip position estimation error	82
4.11	Estimated and actual rotor current components in ab reference frame	82
4.12	Per phase resistive load variation connected to the stator terminals during speed variation	84
4.13	Estimated slip speed during load variation	84
4.14	Slip speed estimation error during load variation	84
4.15	Estimated slip position	85
4.16	Slip position estimation error	85
4.17	Estimated and actual rotor current components in ab reference frame during load variation	85
4.18	Laboratory Experimental setup for DFIG system	86
4.19	Performance of the proposed H_∞ based observer relative to MRAS based observer at a speed of 1350 rpm	87
4.20	Error between H_∞ and MRAS observer at a speed of 1350 rpm	87
4.21	Performance of the proposed H_∞ based observer relative to MRAS based observer at a speed of 1185 rpm	88

List of Figures

4.22	Error between H_∞ and MRAS observer at a speed of 1185 rpm	88
4.23	Relative performance of the proposed H_∞ based observer at close to synchronous speed with respect to MRAS based observer and the rotor phase current.	89
4.24	Error between H_∞ and MRAS observer during changed from subsynchronous to supersynchronous	89
4.25	Slip position estimator results during sudden load variation.	90
4.26	Error between H_∞ and MRAS observer during sudden load variation	90
5.1	Speed profile of DFIG.	97
5.2	Estimated and actual rotor speeds of DFIG.	98
5.3	Turbine torque (T_t) and DFIG Torque (T_e) responses.	99
5.4	Estimated and actual rotor positions during starting of DFIG.	100
5.5	Estimated and actual rotor positions during step change of DFIG rotor speed.	100
5.6	Estimated and actual rotor positions during short circuit of stator terminals.	101
5.7	Estimated and actual rotor positions during rotor speed almost equal to the synchronous speed.	101
5.8	Estimated and actual rotor positions during step change of turbine torque.	102
A.1	Starting procedure of the DFIG system (simulation) for estimator algorithm testing.	112
A.2	Starting procedure of the DFIG system (hardware) for estimator algorithm testing.	113
A.3	Experimental setup.	114
B.1	Three phase stator and rotor coils of the DFIG.	117
B.2	Space vector representation of the reference frames.	118
B.3	Structure of SRFPLL	121
B.4	$\alpha\beta$ Model of the DFIG in stator reference frame.	121
B.5	Stator flux estimation using Low Pass Filter	125

List of Tables

1.1	Mode of operations	6
A.1	110





List of Acronyms

DFIG	Doubly-fed induction generator
MRAS	Model reference adaptive system
GWEC	Global Wind Energy Council
WECS	Wind energy conversion system
VSCF	Variable speed constant frequency
RSC	Rotor side converters
GSC	Grid side converters
WRIG	Wound rotor induction generator
PWM	Pulse width modulation
RPE	Rotor position estimation
IGBT	Insulated Gate Bipolar Transistor
IPM	Intelligent Power Module
PCSPE	Predictor Corrector based Slip Position Estimator
ASSPE	Adaptive Speed and Slip Position Estimator
SRFPLL	Synchronous Reference Frame Phase Locked Loop
LMI	Linear Matrix Inequality
ADC	Analog to Digital Converter
DAC	Digital to Analog Converter
FOC	Field Oriented Control
EKF	Extended Kalman Filter



Nomenclature

Symbol	Definition	Units
V_{as}, V_{bs}, V_{cs}	Stator phases voltages	V
V_{ar}, V_{br}, V_{cr}	Rotor phases voltages	V
I_{as}, I_{bs}, I_{cs}	Stator phases currents	A
I_{ar}, I_{br}, I_{cr}	Rotor phases currents	A
V_{dc}	Dc link bus voltage	V
I_{dc}	Dc link current	A
$V_{\alpha s}, V_{\beta s}$	α and β axis stator voltages	V
$V_{\alpha r}, V_{\beta r}$	α and β axis rotor voltages	V
V_{ar}, V_{br}	a and b axis rotor voltages	V
V_{ds}, V_{qs}	d and q axis stator voltages	V
V_{dr}, V_{qr}	d and q axis rotor voltages	V
$i_{\alpha s}, i_{\beta s}$	α and β axis stator currents	A
$i_{\alpha r}, i_{\beta r}$	α and β axis rotor currents	A
i_{ar}, i_{br}	a and b axis rotor currents	A
i_{ds}, i_{qs}	d and q axis stator currents	A
i_{dr}, i_{qr}	d and q axis rotor currents	A
$\psi_{\alpha s}, \psi_{\beta s}$	α and β axis stator flux linkages	Wb
$\psi_{\alpha r}, \psi_{\beta r}$	α and β axis rotor flux linkages	Wb
ψ_{ar}, ψ_{br}	a and b axis rotor flux linkages	Wb
ψ_{ds}, ψ_{qs}	d and q axis stator flux linkages	Wb
ψ_{dr}, ψ_{qr}	d and q axis rotor flux linkages	Wb

Nomenclature

R_s	Stator resistance	Ω
R_r	Rotor resistance	Ω
L_{ls}	Stator leakage inductance	H
L_{lr}	Rotor leakage inductance	H
L_s	Stator inductance	H
L_r	Rotor inductance	H
L_m	Mutual inductance	Wb
ω_m	Rotor mechanical speed	rad/sec
ω_r	Rotor electrical speed	rad/sec
ω_s	Stator speed	rad/sec
ω_{sl}	Slip speed	rad/sec
$\hat{\omega}_r$	Rotor electrical speed	rad/sec
$\hat{\omega}_{sl}$	Estimated slip speed	rad/sec
θ_m	Rotor mechanical position	rad
θ_r	Rotor electrical position	rad
θ_s	Stator position	rad
θ_{sl}	Slip position	rad
$\hat{\theta}_r$	Rotor electrical position	rad
$\hat{\theta}_{sl}$	Estimated slip position	rad
T_e	Electromagnetic torque	Nm
T_L	Load torque	Nm

1

Introduction

Contents

1.1	Introduction	2
1.2	Types of Generator Configurations for WECS	3
1.3	DFIG Based Wind Energy Conversion Systems	4
1.4	Stand-alone Generators with Doubly-fed Configuration	5
1.5	Literature Review	8
1.6	Motivation and Objective	10
1.7	Thesis Organization	12

1.1 Introduction

With the start of 21st century, the focus of generation gradually shifts towards the renewable sources of energy to have a green and sustainable grid. Wind and solar are the two major sources of renewable energy, and others are like fuel cell, biomass, etc. Among these, wind energy is one of the fastest growing renewable energy sources. The coastal areas and the offshore grid has a vast potential of wind energy generation. Among the various renewable energy sources, the technology associated with the generation of wind energy is considered to be more environmental friendly. Since 2010, there is a rapid expansion of the worldwide installed capacity of wind power. Global Wind Energy Council (GWEC) [1] and Electric India Magazine [2] reported that the installed capacity of wind power of the world was about 233 GW in 2011, whereas the present installed capacity of the world is about 435 GW. India, with its 14550 MW installed capacity stands 5th after China (44733 MW), US (40180MW), Germany (272156) and Spain (20676 MW). The total installed capacity for wind energy globally is 651 GW in 2019 [1]. India's 2022 vision is to increase its installed capacity by 60 GW.

To achieve this target, a more efficient technology such as variable speed constant frequency (VSCF) wind energy conversion system (WECS) is required. This technique can captures the maximum possible energy from the wind [3]. The commonly used variable speed generators are doubly-fed induction generator (DFIG), permanent magnet synchronous generator, synchronous reluctance generator, etc. Among these, the DFIG is one of the preferred choices in WECS due to its low maintenance cost, low installation cost, and high efficiency. Furthermore, DFIG offers various features such as decoupled active and reactive power control, low converter cost, variable speed operation ($\pm 33\%$ slip speed variation) [4]. The controllers of DFIGs are quite complex, and hence, accurate estimation of rotor position and speed plays a significant role in improving the performance of the controller for its sensorless operation. The present thesis work is focused towards the design and hardware implementation of robust observers for rotor or slip position, and speed of DFIG.

The different types of generator configurations and their comparative study is discussed in the subsequent section. Later, a general overview of the DFIG based WECS, which is followed by the study of standalone DFIG configuration and literature review.

1.2 Types of Generator Configurations for WECS

WECS generation systems can be broadly classified into three major categories based on their operational speed: a) Fixed Speed, b) Limited Speed and c) Full Variable speed. They are also categorized into five different types based on the types of the generator used in the WECSs. Type 1 comes under Fixed Speed, Type 2 and Type 3 under Limited Speed and Type 4 and Type 5 under Full Variable Speed. The types of WECS are summarized in Figure 1.1.

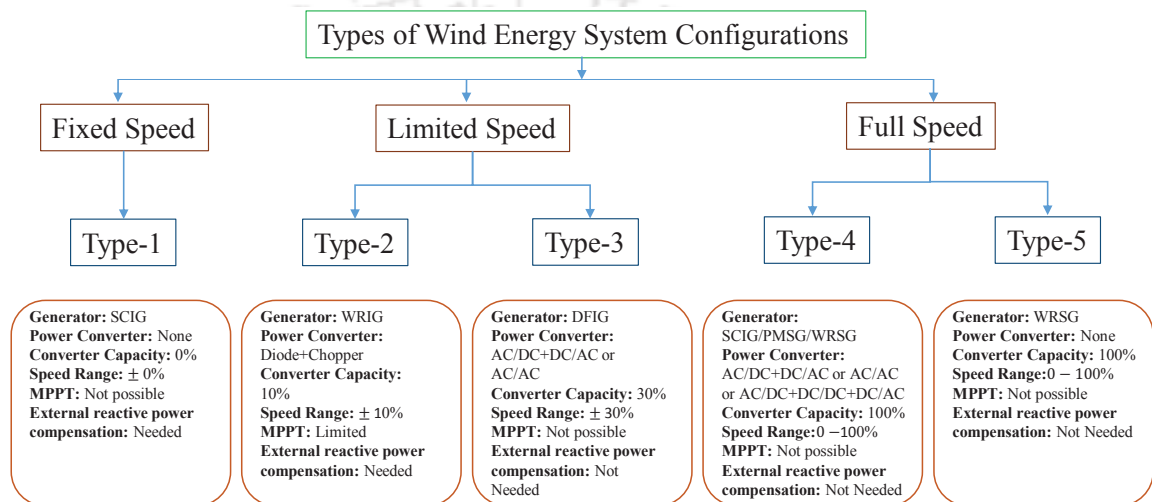


Figure 1.1: Types of wind energy system configurations.

The advantages and disadvantages of the different WECS configuration are as follows:

1) Fixed Speed Systems -

- (i) In Fixed Speed Systems, construction is reliable and has simple electrical interface. However, severe stresses come on the mechanical parts which require additional safety considerations during design.
- (ii) Continuous cut - in and cutoff of capacitors are required to maintain power factor, causing undesirable transients in line current and voltage.

2) Limited Speed Systems -

- (i) Overall converter cost is reduced since it requires to deliver only slip power instead of complete machine power.

- (ii) Rotor side converter allows positive and negative power control. It also enables the operation of machine in sub - synchronous speed and super-synchronous speed range.
 - (iii) Reactive power is supplied by DC link capacitors and hence, the power factor control on stator side is possible.
 - (iv) Line side converter works as an active filter which allow the unity power factor of the machine.
 - (v) Reduced system losses which improves the overall system efficiency.
- 3) Full Speed Systems -
- (i) Mechanical oscillations are absent in the drive train due to direct control of torque using techniques like Direct Torque Control or Field Oriented Control.
 - (ii) Gear Box requirement is absent in case of multi - pole synchronous machine.
 - (iii) Converter rating must be equal to machine rating, as the total generated power passes through the converter.
 - (iv) Filter design for Inverter output and EMI filter is difficult and expensive.
 - (v) Operation above synchronous speed is not possible at full load torque.

Among the various type of WECS, the present thesis mainly discuss the use of DFIG, which belongs to Type 3 categories. A brief overview of the DFIG based WECS is given in the following section.

1.3 DFIG Based Wind Energy Conversion Systems

A generic schematic diagram of DFIG based wind energy conversion system is shown in Figure 1.2. In this Figure 1.2, the back-to-back converters of DFIG are referred to as rotor side converter (RSC) and grid side converter (GSC), respectively. The output of the GSC is connected to the utility grid through the 3 phase grid filter. The RSC provides independent control of generator torque and stator reactive power. The active and reactive power flows between the converter and the grid are controlled by GSC by using decoupled control strategy. The flow of active power between the grid and the rotor side of the machine is controlled by maintaining the constant DC voltage.

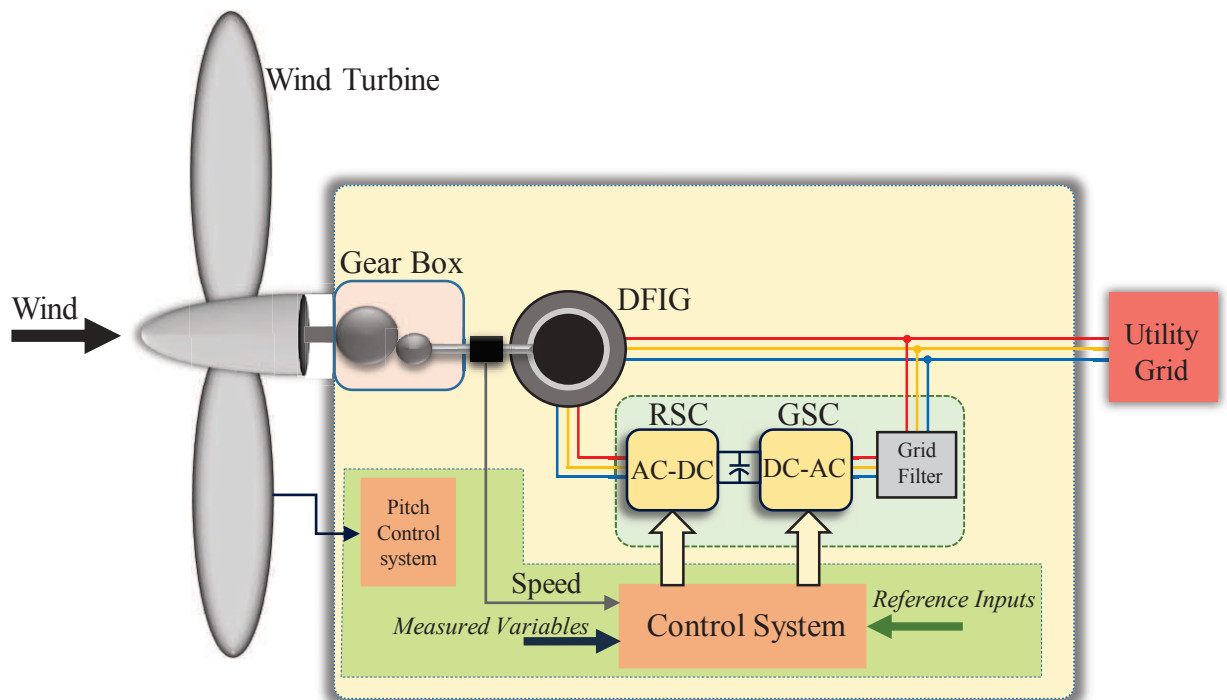


Figure 1.2: DFIG based wind energy conversion system

The shaft of the DFIG is connected to the wind turbine through the gear box assembly unit. The turbine speed is controlled to extract maximum energy from the wind by coordinating the aerodynamic torque and pitch angle, maintaining the wind turbine speed within rated limits. The speed encoder, the current and voltage sensor inputs are given as measured variables to the control system. The voltage and current reference serve as reference inputs. Based on these inputs, the control system is developed to extract maximum electrical power from the wind. Nowadays, for small scale WECS, standalone DFIG based system is widely used. In the following section, the standalone DFIG system configuration and its power flow at different speed ranges are discussed in detail.

1.4 Stand-alone Generators with Doubly-fed Configuration

A stand-alone microgrid with WECS plays an important role towards the electrification of remote or rural areas. The type of source feeding such systems are like a wind turbine, diesel turbine, etc. For the energy-efficient operation of these turbines, it is required that these turbines operate at variable speed. Hence, the control of electrical generator connected to these turbines need to be in such a way so that terminal voltage and frequency are maintained at the expectable level. DFIG is one of the generators which could be used to achieve the desired objectives.

1. Introduction

The variable and unpredictable nature of wind turbine speed lead to fluctuations in the output power of the generator affecting the generated voltage and frequency of the isolated grid system. Therefore, there is a need for stable, reliable, and robust controllers for DFIG. However, to develop such systems, there is a need for a better estimator for sensorless control of DFIG. The DFIG configuration and its power flow are presented in the following subsection.

1.4.1 DFIG Configuration and Modes of Operation

DFIG uses a wound rotor induction generator (WRIG) with the stator windings directly connected to the grid and rotor windings connected to the stator terminal through the back-to-back converter. A transformer is used to match the voltage levels between the grid and grid side converter. The arrangement of DFIG configuration is shown in Figure 1.3.

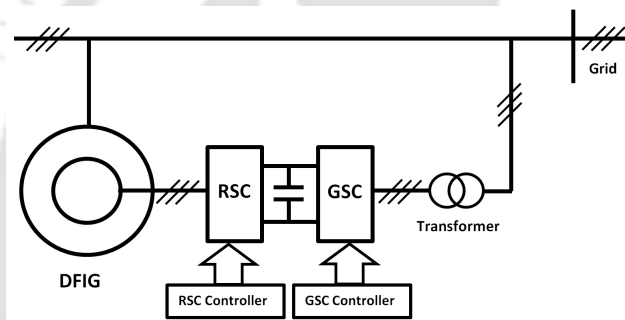


Figure 1.3: DFIG Configuration.

The DFIG system, as presented in Figure 1.3 shows enormous flexibility in terms of control of active and reactive powers. The mode of operations [4], [5] are explained in tabular form as given in Table 1.1,

Table 1.1: Mode of operations

Slip (s)	Speed	Operation mode	$Torque$	P_{mech}	P_{stator}	P_{rotor}
$0 < s < 1$	Sub-Synchronous	motor	> 0	< 0	< 0	> 0
$0 < s < 1$	Sub-Synchronous	generator	< 0	> 0	> 0	< 0
$s < 0$	Super-Synchronous	motor	> 0	> 0	< 0	< 0
$s < 0$	Super-Synchronous	generator	< 0	> 0	> 0	> 0

The bi-directional back-to-back power converter is consisting of two conventional pulse width modulation (PWM) voltage source converters and a common DC bus employing a DC-link capacitor as shown in Figure 1.3. Back-to-back converters are widely used in DFIG based system for wind

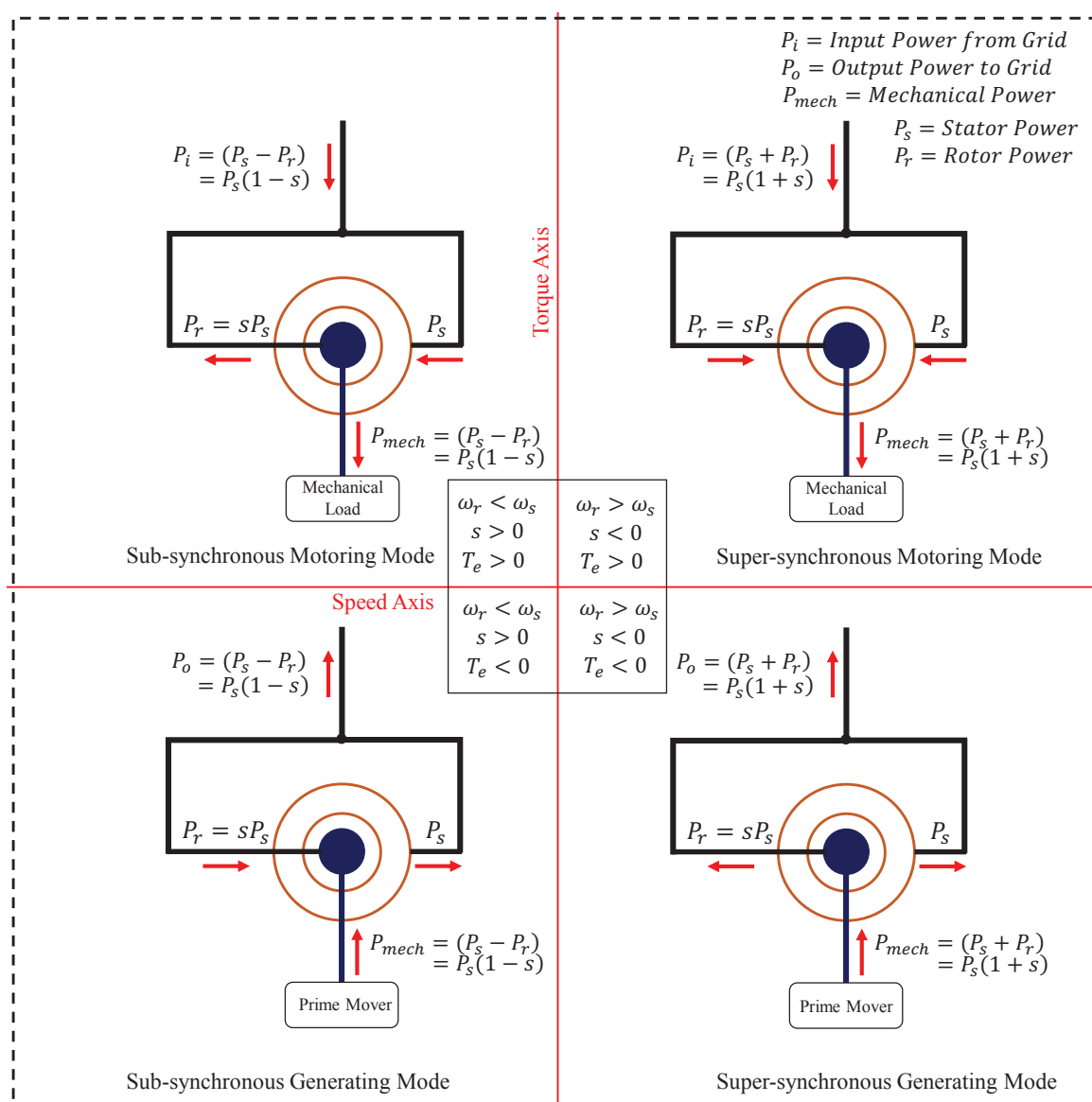


Figure 1.4: Power flow schematic diagram for all modes of operation of the DFIG system (neglecting losses).

power applications to produce more power output. Depending upon the decoupled control strategy and complexity, the DFIG can be operated in both sub-synchronous and super-synchronous speed range ($\pm 30\%$ slip). The grid side converter (GSC) is controlled to maintain constant DC-link voltage and it is responsible also for reactive power control of the DFIG and grid. The rotor side converter (RSC) control strategy basically takes care about electromagnetic torque control and the rotor excitation currents. The whole control strategy is defined in synchronous reference frame which are decomposed into d-q components. For the GSC control, d-axis voltage vector represents the DC-link voltage control and q-axis current is used to control the electromagnetic torque. The control strategy

maintains the power factor at unity. It is important to ensure that the dynamics of the speed controller are not extremely fast, else large transients in generator torque may occur. The rating of the converter is around 33% of total generator power. It is dependent on the selected speed range or the slip power produced. Due to the bi-directional power flow ability of the converter, the DFIG operates as a generator or motor in both sub-synchronous and super-synchronous speed range which is explained in Table 1.1. For the sake of simplicity neglecting all the losses, a detailed power flow diagram is shown in Figure 1.4. In the Figure 1.4, P_s and P_r refer to the active power flow at the stator and rotor terminals respectively. The P_i and P_o represent input power from grid and output power to grid, respectively. The mechanical power at the machine shaft is denoted by P_{mech} . In the motoring modes, the power required by the mechanical load at the machine shaft is fed from the utility grid. In generating modes, the direction of power flow is from the machine shaft towards the utility grid. During motoring mode, the electromagnetic torque, T_e is positive and negative for generating mode of the DFIG. The direction of slip, s depends on the rotor electrical speed, ω_r and the synchronous speed, ω_s . In sub-synchronous mode, $\omega_r < \omega_s$ and in super-synchronous mode, $\omega_r > \omega_s$.

1.5 Literature Review

Different types of WECS configuration have been discussed in literature. DFIG based WECS is an established and popular configuration. For a grid-connected DFIG based WECS, it is possible to have maximum power point tracking (MPPT) [6], variable speed constant frequency (VSCF) operation [4], independently active-reactive power regulation [7]. In a WECS, for a partially steady load, the primary objective is to maximize the turbine aerodynamic efficiency by controlling the turbine rotor speed. This can be done by manipulating the generator torque and blade pitch angle. The more difficult task is to design a controller which maximizes conversion efficiency while keeping transient load minimum. There is a trade-off between maximum conversion efficiency and minimum transient load. Due to unpredictable variations in the wind speed, it becomes a challenging task to regulate both DFIG power output and generator speed at their rated value in the presence of severe fluctuations in the turbine power under full load conditions. These fluctuations in power lead to variations in the torque and grid power. The cyclic aerodynamic torque [8] variations also increase the dynamic loads and voltage flicker. Nonlinearity in system dynamics and continuous variation of the operating point

make the process of controller designing more challenging.

Sensorless strategies are usually used to estimate the DFIG flux and rotor position [9]. This reduces the cost, size, and maintenance of the drive system. Due to the nonlinearity of the wind turbine dynamics and stochastic behavior of the wind, it is not easy to estimate the rotor position and machine flux.

[10] and [11] explain vector control techniques used for the independent control of torque and excitation current in the synchronous reference frame. [12] describes the decoupled control of active and reactive powers of the machine. In this method, the reference frame is fixed to the air-gap flux, and the rotor side is connected to the grid via a cycloconverter. Converter design and control techniques are described in [13]. [14] gives the detailed design of a DFIG using back-to-back PWM voltage-source converters in the rotor circuit and validated the system experimentally.

The instantaneous position of the rotor with respect to the stator is required for the decoupled control of active and reactive power. In conventional field oriented control schemes, the instantaneous rotor position is estimated by using an absolute encoder fitted to the shaft. A high-resolution position encoder is very expensive, and reduces system reliability. Further, in a DFIG based wind turbine system, the mounting of an encoder is not an easy task. The encoder must be mounted in such a way that the angle between rotor and stator axis can be accessed directly. [11] describes the sensorless vector control of the machine. A sensorless position estimator for rotor side field-oriented control of the machine is implemented in [15]. [16] uses the model reference adaptive system (MRAS) to estimate the same. Other techniques have also been proposed to estimate rotor position, rotor currents, and torque angle [17, 18].

Generally, open-loop observers [15], [17], [18], [19] and [20] are used to estimate the rotor position. The rotor speed is obtained by differentiating the rotor position. This introduces noise in the speed estimator. Moreover, open-loop estimators are highly dependent on machine parameters, and the accuracy of the estimator is not guaranteed.

Closed-loop model reference adaptive system (MRAS) observers [9], [21] using different output variables for speed adaptation have been analyzed and compared. MRAS observer models are based on static flux-current relations. Therefore, they are very sensitive to machine inductance. Another

drawback is that all adaptive observers are implemented in the stationary reference frame, where the electrical states are usually sinusoidal functions of time. Since the stator side is directly connected to the grid and the rotor side is connected via a back-to-back converter, the DFIG becomes very sensitive to grid faults [22]. A wind turbine must continue to supply power to the grid even when the grid voltage dips or when a fault (symmetrical/asymmetrical) occurs [22]. In other words, it must have a fault ride through (FRT) capability [23].

In literature, FRT with converter protection technology [23], low voltage ride through [24], voltage-frequency regulations [25], uninterrupted power flow operations under balanced or unbalanced grid faults [26] as well as island operations in the distributed energy generation systems are reported.

During the fault condition, the DC-link voltage must be stable and current fluctuations of the GSC must be limited. During this operation, DC-link voltage fluctuations might influence the rotor current control strategy, which is undesirable. DC-Link capacitor sizing has to be optimized for the high voltage applications because of it being heavy, expensive, and unreliable. Improved control strategies such as direct capacitor current control and current injection methods are given in [27–29]. However, these are not effective to get the desired performance.

1.6 Motivation and Objective

Designed controller must also be robust in terms of its stability. Various control strategies have been proposed to meet these objectives. These include vector control [30], [31], direct torque control [32] [33], direct power control [34] [35] [36], and decoupled P-Q control [37], [38]. A controller for a DFIG based WECS should be extremely robust to parameter variations and changes in operating points. These strategies are sensitive to the accuracy of the measured or estimated rotor slip position of the DFIG. Slip position can be obtained from a mechanical encoder or through rotor position estimation. However, mechanical encoders have several demerits, such as high system cost, wiring complexity, and reduced robustness and reliability. Alternatively, one can use sensorless rotor/slip position estimation techniques to avoid these shortcomings [39] [40] [41].

Reference [42] proposes a rotor flux based estimator, but the estimator may fail to converge in the presence of parametric uncertainty and measurement noise [43]. Further, it shows poor performance while the machine operates near the synchronous speed [44]. MRAS based observers are widely

used for rotor speed and position estimation [45], [46]. An MRAS based observer uses two models, namely, reference model and adjustable model. The error function used in an MRAS based observer is usually the cross product of the estimated and actual vector components. This is typically nonlinear and non-monotonic in nature. This causes an oscillatory transient response during fly start [47]. In [9], a modified error function using the inverse tangent function is suggested. This, however, results in an increased computational burden. Various adaptation technique have been used for MRAS observers, such as PI controller, hysteresis control [48], sliding mode control, and fuzzy logic controller [49].

Rotor flux, stator flux, stator current and rotor current based MRAS observers are widely used in DFIG systems [16], [50]. A comparative analysis of these observers is given in [50]. However, the flux-based MRAS observers are inappropriate for speed and position estimation due to the following reasons,

- (i) The rotor flux MRAS shows poor performance close to synchronous speed as magnetizing current provided from the rotor side is weak.
- (ii) Stator flux-based observers suffer from the integration drift problem. This may lead to integrator saturation. Further, the integrator is dependent on the initial condition.

The limitations of the current based observers are given below,

- (i) Stator current based MRAS observers strictly depend on the minimum load connected to the DFIG stator terminals. Such observers may become unstable for small stator currents.
- (ii) Rotor current based MRAS observers are very sensitive to machine parameters, such as change in stator inductance and mutual inductance. Moreover, it is difficult to get an accurate estimate of the mutual inductance of the machine.
- (iii) Rotor current based MRAS observers show better performance compared to other MRAS observers. However, the stability of the observer is ensured only over a small operating range.

This can be inferred that the control of active and reactive power of the machine requires a reliable and robust control of the rotor side converter. Implementation of a robust control system for the rotor

side converter needs the transformation of rotor variables to the synchronous reference frame, which requires an accurate estimation of the rotor slip position.

In view of the limitations of the existing observers, the objective behind the present thesis is to develop a robust, adaptive, and accurate observer for DFIG slip angle estimation. The observers developed in the present thesis mainly estimate the rotor slip position and speed. While designing an observer, it is important to know the range of gain for which the operation of the observer is stable. Hence, there is a need to provide a stability analysis of the proposed observer. The main criteria utilized to design the observer in this thesis are:

- Stable operation of the observer even when there is wide variation in speed.
- Stable operation of the observer near synchronous speed.
- The observer must be accurate and robust to parameter variations and changes in operating points.
- Ability to start on the fly.

Furthermore, there is a need to verify the performance of the proposed observers. Hence, a hardware setup is developed in the laboratory, which includes DFIG, synchronous reference phase locked loop (SRFPLL), and sensors and their interfacing circuit to the DSP processor.

1.7 Thesis Organization

The work carried out in this thesis is organized into six chapters.

Chapter 1 discusses the basic concepts of WECS. It also briefly talks about the various types of WECS and different modes of operation of DFIG. It briefly describes and then reviews the existing literature on rotor angle estimation and speed of a DFIG. Finally, it gives the motivation for the work presented in this thesis.

Chapter 2 presents a predictor-corrector based closed-loop rotor slip-position estimator (PCSPE). This method uses the measured values of the stator voltage, stator current, and rotor current, and rotor speed. This chapter provides a stability analysis of the proposed observer and the range of gains for its stable operation. The proposed algorithm is simulated in PSCAD Software to evaluate its dynamic

performance. The performance of the algorithm is also demonstrated in a developed laboratory-scale experimental set up of DFIG.

Chapter 3 has proposed a new closed-loop adaptive speed and slip position observer (ASSPE) for a standalone DFIG system. This method uses the measured value of the stator voltages, stator currents and rotor currents. The proposed ASSPE requires less number of DFIG parameters as compared to the model-based observers available in the literature. This ASSPE considers the turns ratio and stator leakage inductance, which improves the estimation accuracy. Further, the estimation of stator and rotor flux is avoided. The measured stator voltage and current are used to calculate the rotor current in the synchronous reference frame. At a given time instant, the previous estimate of slip speed is used to calculate an a priori estimate of slip position. This estimated position is then used to transform the calculated rotor current to the rotor reference frame. The angle of rotor current vector thus estimated is compared to that of the measured rotor current vector, and the difference between the two is used to obtain the slip angle estimate. This slip angle estimate is used to convert the measured current to the slip speed reference frame. The rotor speed estimator estimates the angular frequency of this current vector (in the slip speed reference frame). The stability of the algorithm is also analyzed in this chapter. The effectiveness of the proposed algorithm has been simulated in PSCAD software, which estimates rotor speed and slip position accurately. It also shows good performance during sudden speed and load variation, and 30% mutual inductance variation. Finally, the estimator has been implemented and validated in real-time on a hardware setup of DFIG. This work has also been compared with flux-based slip position estimator described in Chapter 2.

Chapter 4 presents a new robust two-stage observer to mitigate the effects of sudden changes in speed and load, parametric uncertainty, and noise. The proposed observer estimates the rotor slip position and speed of the DFIG accurately. It takes stator terminal voltages and currents, and the rotor currents as inputs. The structure of the proposed observer is divided into two stages. The first stage is used to estimate the rotor current vector in stator reference frame. This vector is then used in the second stage to obtain the slip position. The effects of parametric uncertainty, shift in operating point, noise and other deficiencies are modelled using a disturbance signal. It is assumed that the change in slip speed is brought about by a signal whose L_2 gain is finite. The current estimate in the first stage

is transformed to rotor reference frame using slip angle estimate in second stage. The cross product of this calculated rotor current vector and measured current rotor vector acts as the error signal for the second stage. Thus, the algorithm in the second stage is sensitive to sudden changes in current measurements. This algorithm is made robust by limiting the H_∞ gain between the error signal and slip position and speed. The gains of the proposed observer are computed by solving Linear Matrix Inequalities (LMIs). The working of the proposed observer has been simulated in PSCAD software. Moreover, the effectiveness of the proposed observer has been verified on a laboratory test bench with a 2.2 kW standalone DFIG system.

Chapter 5 proposes an Extended Kalman Filter (EKF) based observer, which uses an augmented state model to estimate the rotor position and speed accurately for a grid-connected DFIG system. We have compared three types of state models:

- without integral states (non-augmented state model),
- with integral of stator and rotor current (partially augmented state model), and
- with integral of stator and rotor current and integral of square of the stator and rotor currents (augmented state model).

The performance of the estimators has been analyzed and discussed under various dynamic conditions. The effectiveness of the proposed EKF based observer is simulated in MATLAB Simulink.

Chapter 6 presents the conclusions of the thesis and how the work presented in the thesis could be extended in the future.

2

Stator Flux Based Slip Angle Estimation

Contents

2.1	Introduction	16
2.2	Mathematical Model of DFIG	16
2.3	Rotor Slip-position Estimation Technique	17
2.4	Stability Analysis	19
2.5	Simulation Results	21
2.6	Experimental Results:	27
2.7	Conclusion	29

2.1 Introduction

Doubly fed induction generators (DFIG) are widely used in variable-speed wind energy conversion systems. The system includes a wound rotor induction machine and a back-to-back power converter, which is connected between the stator and rotor terminal of the machine. Various control strategies like vector control, direct torque control etc, require accurate position of the rotor angle. Earlier, position sensors were used to sense the rotor position, but they have many demerits such as machine size, drive cost, reliability, mounting, robustness and noise. This necessitates the use of a sensorless algorithm to accurately estimate the rotor position. Stability and a wide operating range are key requirements of such an estimator. Further, the estimation process must quickly converge to the correct position irrespective of the initial condition.

The most prominent rotor position estimation methods reported in literature are open-loop observers and model reference adaptive system (MRAS) estimators. The performance of open-loop estimation methods is unsatisfactory in the face of parametric uncertainty or measurement noise due to unavailability of error correction mechanism [31, 51, 52]. MRAS based estimator schemes have been extensively discussed in literature [43, 53–58]. However, MRAS based estimators have not been tested for fault conditions.

This chapter discusses a predictor-corrector based closed loop rotor slip position estimator. Further, it analyzes the stability of the observer and find the range of gain for which the observer converges. This method uses the measured values of the stator voltage stator current and rotor current.

2.2 Mathematical Model of DFIG

The general symmetrical ac machine is given by the following mathematical model from (2.1) to (2.6). The stator and rotor voltage components are given by

$$[V_s]^{\alpha\beta} = R_s[i_s]^{\alpha\beta} + \frac{d[\psi_s]^{\alpha\beta}}{dt} \quad (2.1)$$

$$[V_r]^{\alpha\beta} = R_r[i_r]^{\alpha\beta} + \frac{d[\psi_r]^{\alpha\beta}}{dt} - j\omega_r[\psi_r]^{\alpha\beta} \quad (2.2)$$

The stator and rotor flux components are given by

$$[\psi_s]^{\alpha\beta} = L_s[i_s]^{\alpha\beta} + L_m[i_r]^{\alpha\beta} \quad (2.3)$$

$$[\psi_r]^{\alpha\beta} = L_r[i_r]^{\alpha\beta} + L_m[i_s]^{\alpha\beta} \quad (2.4)$$

The electromagnetic torque is given by

$$T_e = \frac{3p}{2}(\psi_{\alpha s}i_{\beta s} - \psi_{\beta s}i_{\alpha s}) \quad (2.5)$$

$$\frac{d\omega_m}{dt} = \frac{1}{J}(T_e - T_l - f_\mu\omega_m) \quad (2.6)$$

where, the machine stator, rotor, and mutual inductances are denoted by L_s , L_r and L_m respectively.

The stator resistance and rotor resistance are denoted by R_s and R_r , respectively.

The detailed mathematical model of the DFIG derived using the dynamic equations explained above is given in Appendix B.

The proposed rotor position estimation (RPE) algorithm and the stability analysis of the same have been presented in this chapter. The performance of the algorithm is verified on a laboratory developed DFIG test setup.

2.3 Rotor Slip-position Estimation Technique

In this section, a simple predictor corrector based algorithm to estimate the rotor position is presented.

The proposed estimation algorithm takes the measured rotor speed, stator current, rotor current and stator voltages as inputs. The transformation matrix for 3-phase rotor current in rotor reference frame (ab) is as follows

$$\begin{bmatrix} i_{ar} \\ i_{br} \end{bmatrix} = \begin{bmatrix} 1 & -\frac{1}{2} & -\frac{1}{2} \\ 0 & \frac{\sqrt{3}}{2} & -\frac{\sqrt{3}}{2} \end{bmatrix} \begin{bmatrix} i_{Ar} \\ i_{Br} \\ i_{Cr} \end{bmatrix} \quad (2.7)$$

Using the previous estimate of the rotor position $\theta(k-1)$ and the measured rotor speed ω_r , one can

2. Stator Flux Based Slip Angle Estimation

make the following apriori estimate of the current rotor position (θ_{ap}),

$$\theta_{ap}(k) = \theta(k-1) + \omega_r(k-1)\Delta t \quad (2.8)$$

With the help of this angle estimate and the measured values of the rotor current components i_{ar} and i_{br} , the $\alpha - \beta$ components of the rotor currents can be evaluated as follows

$$\hat{i}_{\alpha r} = i_{ar} \cos \theta_{ap}(k) - i_{br} \sin \theta_{ap}(k) \quad (2.9)$$

$$\hat{i}_{\beta r} = i_{ar} \sin \theta_{ap}(k) + i_{br} \cos \theta_{ap}(k). \quad (2.10)$$

Using the above estimates of $\hat{i}_{\alpha r}$ and $\hat{i}_{\beta r}$, the stator flux components can be calculated as:

$$\hat{\psi}_{\alpha s} = L_s i_{\alpha s} + L_m \hat{i}_{\alpha r} \quad (2.11)$$

$$\hat{\psi}_{\beta s} = L_s i_{\beta s} + L_m \hat{i}_{\beta r}. \quad (2.12)$$

Now, the stator voltage equations of the machine are given by

$$V_{\alpha s} = R_s i_{\alpha s} + \frac{d\psi_{\alpha s}}{dt} \quad (2.13)$$

$$V_{\beta s} = R_s i_{\beta s} + \frac{d\psi_{\beta s}}{dt}. \quad (2.14)$$

For calculating the stator flux, (2.13) and (2.14) give rise to the following alternative expressions

$$\psi_{\alpha s} = \int (V_{\alpha s} - R_s i_{\alpha s}) dt \quad (2.15)$$

$$\psi_{\beta s} = \int (V_{\beta s} - R_s i_{\beta s}) dt. \quad (2.16)$$

The integrations in (2.15) and (2.16) are implemented using the method explained in [59].

Note that if the rotor angle estimate is accurate, the vectors $\hat{\Psi}_s = [\hat{\psi}_{\alpha s} \hat{\psi}_{\beta s}]^T$ and $\Psi_s = [\psi_{\alpha s} \psi_{\beta s}]^T$ will have the same direction. Consequently, the cross product of $\hat{\Psi}_s$ and Ψ_s will be equal to zero i.e. $\hat{\Psi}_s \times \Psi_s = 0$. Hence, an accurate rotor angle estimate implies that $\varepsilon_r = \hat{\psi}_{\alpha s} \psi_{\beta s} - \hat{\psi}_{\beta s} \psi_{\alpha s} = 0$. ε_r is therefore used as a measure for the angle estimation error. The apriori rotor angle estimate is now adjusted by an amount proportional to ε_r , resulting in the following expression for the posteriori angle

estimate $\theta(k)$

$$\theta(k) = \theta_{ap}(k) + G\varepsilon_r(k) \quad (2.17)$$

where, G is the adjustment gain. The procedure described above can be summarized in the following algorithm which is implemented once every sampling interval. Rotor angle estimation algorithm is summarized as follows

- Step 1: Calculation of stator flux linkage

$$\begin{aligned} \psi_{\alpha s} &= \int (V_{\alpha s} - R_s i_{\alpha s}) dt \\ \psi_{\beta s} &= \int (V_{\beta s} - R_s i_{\beta s}) dt \end{aligned}$$

- Step 2: Apriori estimation of rotor angle

$$\theta_{ap}(k) = \theta(k-1) + \omega_r(k-1)\Delta t$$

- Step 3: Alternative estimation of stator flux linkage

$$\begin{aligned} \hat{\psi}_{\alpha s} &= L_s i_{\alpha s}(k) + L_m (i_{ar} \cos \theta_{ap}(k) - i_{br} \sin \theta_{ap}(k)) \\ \hat{\psi}_{\beta s} &= L_s i_{\beta s}(k) + L_m (i_{ar} \sin \theta_{ap}(k) + i_{br} \cos \theta_{ap}(k)) \end{aligned}$$

- Step 4: Error calculation

$$\varepsilon_r(k) = \hat{\psi}_{\alpha s} \psi_{\beta s} - \hat{\psi}_{\beta s} \psi_{\alpha s}$$

- Step 5: Error correction

$$\theta(k) = \theta_{ap}(k) + G\varepsilon_r(k).$$

2.4 Stability Analysis

In this section, we analyze the stability of the algorithm described in the previous section and find the range of gain G , for which the algorithm converges.

2. Stator Flux Based Slip Angle Estimation

The error signal, $\varepsilon_r(k)$ can be expressed as follows

$$\varepsilon_r(k) = \hat{\Psi}_s \times \Psi_s = |\hat{\Psi}_s||\Psi_s| \sin \delta_\theta(k) \quad (2.18)$$

where $\delta_\theta(k)$ is the angle between the two estimated stator flux vectors. For small values of $\delta_\theta(k)$, Eq. (2.18) can be approximated as

$$\varepsilon_r(k) = |\hat{\Psi}_s||\Psi_s|\delta_\theta(k). \quad (2.19)$$

Since during the operation of the machine the stator flux is maintained at a constant magnitude, the product, $|\hat{\Psi}_s||\Psi_s|$ can be assumed to be a constant denoted by ρ . Therefore, $\delta_\theta(k) = \frac{\varepsilon_r(k)}{\rho}$. From (2.8) and (2.17), the value of $\theta(k+1)$ can be written as:

$$\theta_{ap}(k+1) = \theta_{ap}(k) + \omega_r(k)\Delta t + G\varepsilon_r(k) \quad (2.20)$$

Therefore,

$$\Delta\theta_{ap}(k) = G\varepsilon_r(k) + \omega_r(k)\Delta t \quad (2.21)$$

Let $\theta_{aps}(k+1)$ and $\theta_f(k+1)$ be the angles of $\hat{\Psi}_s$ and Ψ_s , respectively. Therefore, $\theta_{ap}(k+1) = (1-s)\theta_{aps}(k+1)$, where, s denotes the slip of the machine. Hence, Eq. (2.21) can be rewritten as

$$(1-s)\Delta\hat{\theta}_{aps}(k) = G\varepsilon_r(k) + \omega_r(k)\Delta t \quad (2.22)$$

where $\Delta\hat{\theta}_{aps}(k)$ is the angle error between $\hat{\Psi}_s$ and Ψ_s . Further,

$$\theta_f(k+1) = \theta_f(k) + \omega_s(k)\Delta t \quad (2.23)$$

as a result,

$$\begin{aligned} \theta_f(k+1) - \theta_f(k) &= \omega_s(k)\Delta t \\ \implies \Delta\theta_f(k) &= \omega_s(k)\Delta t \\ \implies \Delta\theta_f(k) &= \frac{\omega_r(k)}{1-s}\Delta t \\ \implies (1-s)\Delta\theta_f(k) &= \omega_r(k)\Delta t \end{aligned} \quad (2.24)$$

Subtracting (2.22) from (2.24), we get

$$\begin{aligned}
 (1-s)[\Delta\theta_f(k) - \Delta\hat{\theta}_{aps}(k)] &= -G\varepsilon_r(k) \\
 \implies (1-s)\Delta\delta_\theta(k) &= -G\varepsilon_r(k) \\
 \implies (1-s)\frac{\Delta\varepsilon_r(k)}{\rho} &= -G\varepsilon_r(k) \tag{2.25}
 \end{aligned}$$

Therefore, $\varepsilon_r(k) = 0$ is an equilibrium point of the error dynamics.

Consider the function $V[\varepsilon_r(k)] = \{\varepsilon_r(k)\}^2$. Clearly $V[\varepsilon_r(k)]$ is positive definite and is continuous as a function of $\varepsilon_r(k)$. Also, $V[\varepsilon_r(k)] = 0$ if and only if $\varepsilon_r(k) = 0$. Therefore, as a direct consequence of the Lyapunov stability theorem for discrete systems [60], the error signal, $\varepsilon_r(k)$ asymptotically goes to zero if $\Delta V[\varepsilon_r(k)] < 0 \forall k$.

Now,

$$\begin{aligned}
 \Delta\varepsilon_r^2(k) &= \varepsilon_r^2(k+1) - \varepsilon_r^2(k) \\
 &= \{\varepsilon_r(k+1) + \varepsilon_r(k)\}\{\varepsilon_r(k+1) - \varepsilon_r(k)\} \\
 &= \{\varepsilon_r(k+1) + \varepsilon_r(k)\}\Delta\varepsilon_r(k)
 \end{aligned}$$

Further, $\varepsilon_r(k+1) = \Delta\varepsilon_r(k) + \varepsilon_r(k)$.

So, $\Delta\varepsilon_r^2(k) = \{\Delta\varepsilon_r(k) + 2\varepsilon_r(k)\}\Delta\varepsilon_r(k)$

Hence, using (2.25)

$$\Delta\varepsilon_r^2(k) = \frac{\rho^2 G^2}{(1-s)^2} \left\{ 1 - \frac{2(1-s)}{\rho G} \right\} \{\varepsilon_r(k)\}^2 \tag{2.26}$$

Thus, the error asymptotically goes to zero, if $\left\{ 1 - \frac{2(1-s)}{\rho G} \right\} < 0$ i.e. $G < \frac{2(1-s)}{\rho}$. For our analysis, the range of slip s is assumed to be $\pm 30\%$.

The real-time implementation of the closed loop proposed predictor-corrector based observer schematic diagram is shown in Figure 2.1.

2.5 Simulation Results

The proposed algorithm has been tested on a developed model of DFIG in PSCAD software. The parameters of the DFIG model are given in Appendix A. The behaviour of the system has been tested

2. Stator Flux Based Slip Angle Estimation

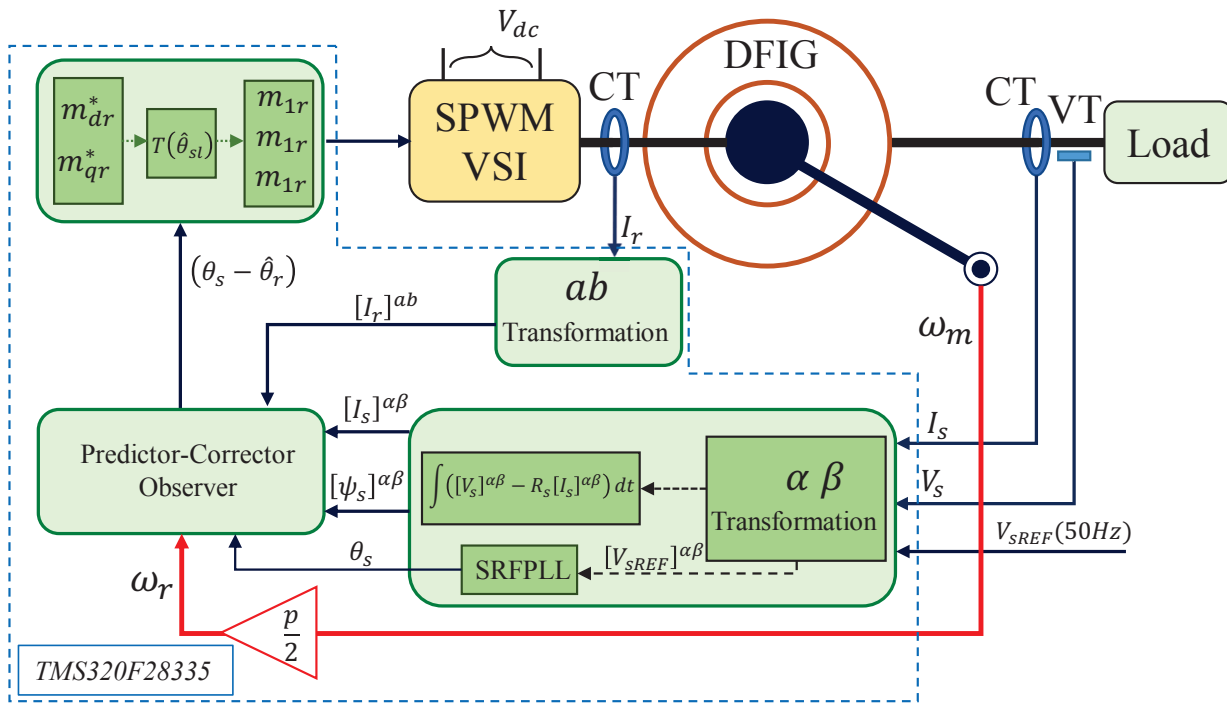


Figure 2.1: Block diagram of the DFIG system with closed loop proposed predictor-corrector based observer

for the following conditions:

- (i) Step changes in the speed reference.
- (ii) Load variation at the stator terminal.

The system was simulated with the following profile:

- The speed reference was set at electrical 293 rad/s (1400 rpm) and system was to settle at that speed.
- At time $t = 8$ s to $t = 9$ s, the resistive load is varied at the stator terminal.
- At time $t = 9$ s to $t = 12$ s, the reference is changed from electrical 293 rad/s to electrical 345 rad/s (1400 rpm to 1648 rpm) and electrical 345 rad/s to electrical 300 rad/s (1648 rpm to 1433 rpm).

The speed profile of the machine is shown in Figure 2.2.

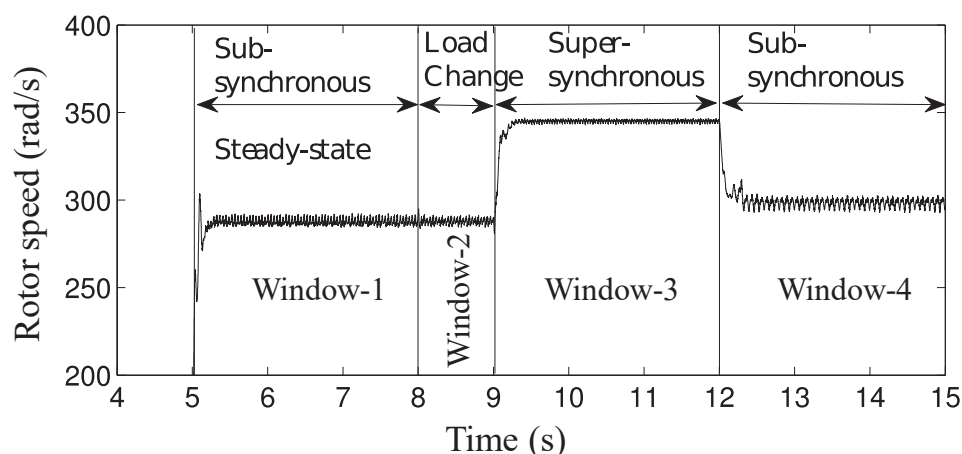


Figure 2.2: Speed profile of DFIG

Initial Phase of the Algorithm:

In response to a speed reference of 293 rad/s, the rotor speed starting from zero, reached the desired value as shown in Figure 2.2. The slip position is estimated from the difference of stator angle θ_s and estimated rotor position $\hat{\theta}_r$. The angle θ_s is obtained using SRFPLL as given in Appendix B. The rotor position is estimated using the proposed predictor - corrector based observer. The estimation algorithm is started at time $t = 5$ s. The resultant slip position is given in Figure 2.3(a). In this case, at starting, the rotor speed is 1400 rpm where slip is 0.067. At this rotor speed, it takes 0.0214 s to complete one revolution. The corresponding estimation error of the rotor position $\hat{\theta}_r$ is given in Figure 2.3(b). It is observed from the Figure 2.3(b) that the observer algorithm converges within 0.025 s.

2.5.1 Case 1: Speed Change Response

Initially, the rotor speed is maintained at 1400 rpm as shown in Window -1 of Figure 2.4. At time $t = 9$ s the speed reference was changed from 293 rad/s to 345 rad/s. At this transition, the rotor speed changes from 1400 rpm to 1648 rpm, where the slip variation is from 0.067 to -0.099. At 1648 rpm, the rotor takes 0.018 s to complete one revolution. The response of the rotor speed is shown in Window -2 of Figure 2.4. The estimated slip position is shown in Figure 2.5(a). Similarly, at $t = 12$ s, the rotor speed deviates from 1648 rpm to 1433 rpm. During this change, the slip varies from -0.099 to 0.045. At 1433 rpm, the rotor takes 0.021 s to complete one revolution. The rotor speed response is given in Window -3 of Figure 2.4. Figure 2.6(a) shows the slip angle variation with the rotor speed deviation from super- synchronous to sub-synchronous starting at $t = 12$ s. The

2. Stator Flux Based Slip Angle Estimation

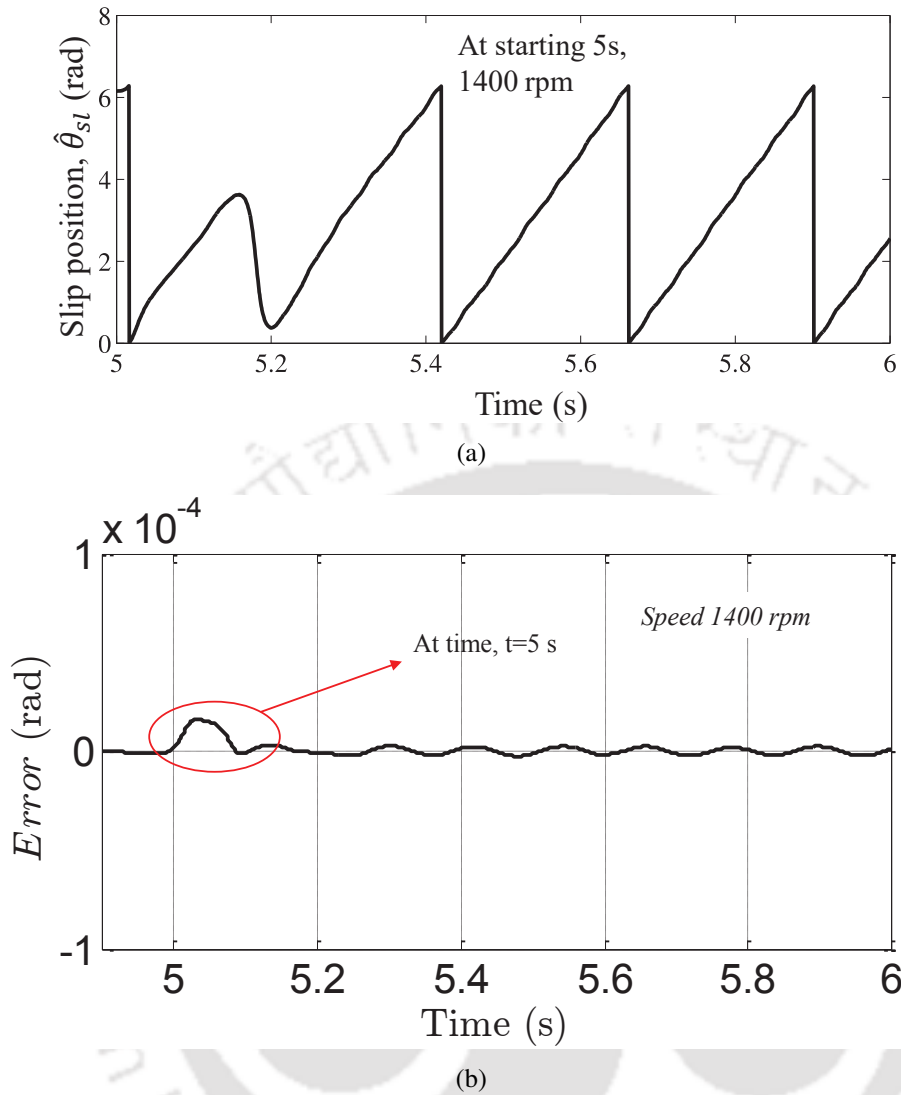


Figure 2.3: Starting response of the algorithm: (a) Estimated rotor slip position, (b) Slip position estimation error plot during starting at 1400 RPM.

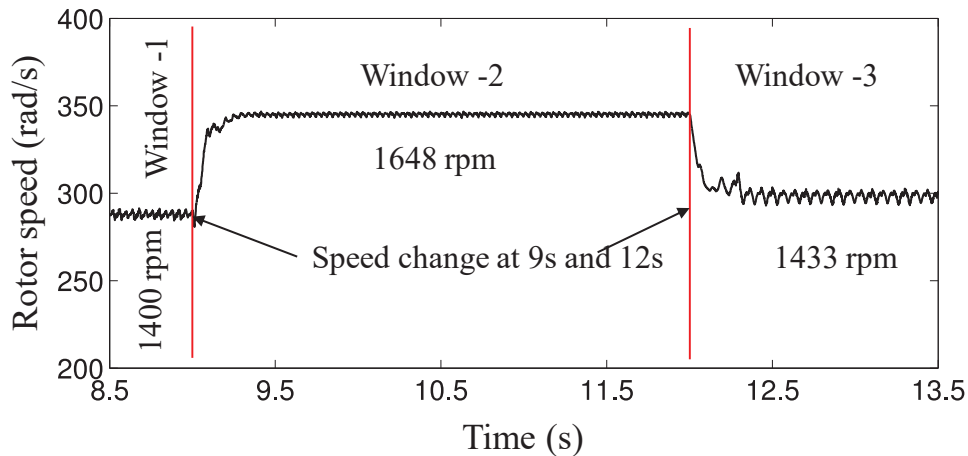
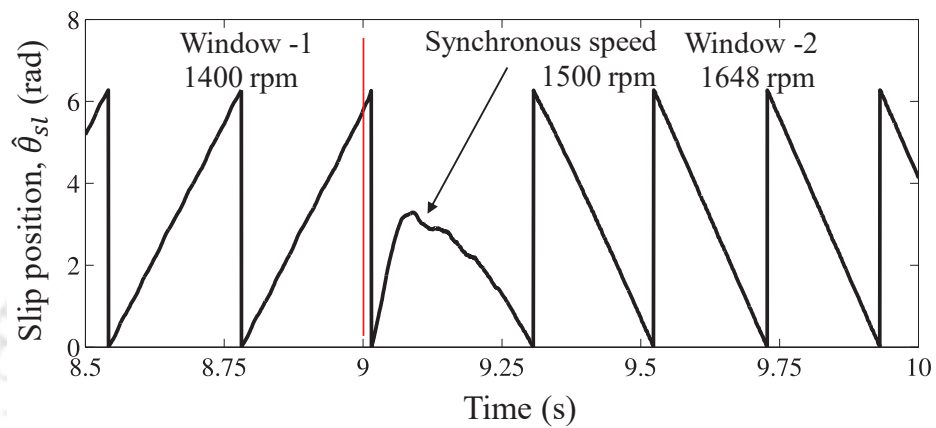
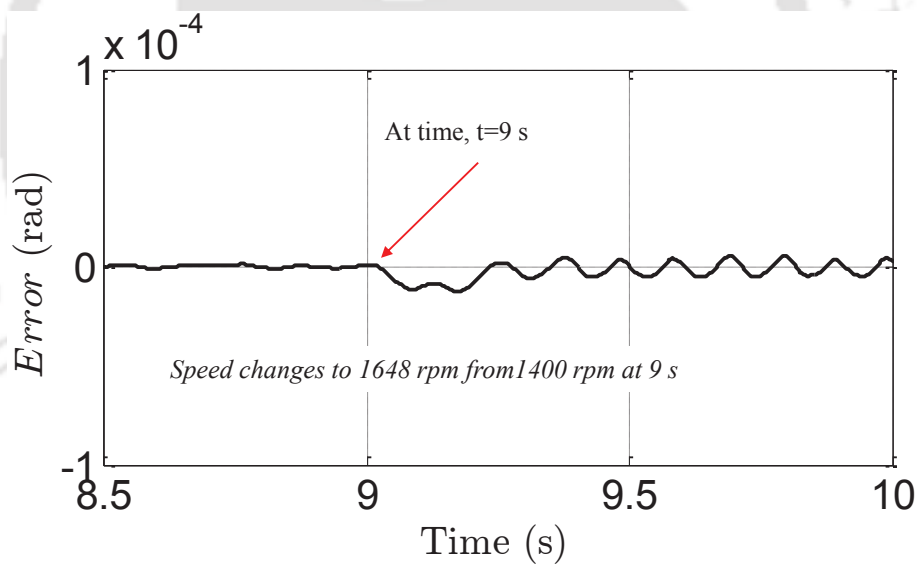


Figure 2.4: Speed reference changes from sub synchronous to super synchronous range



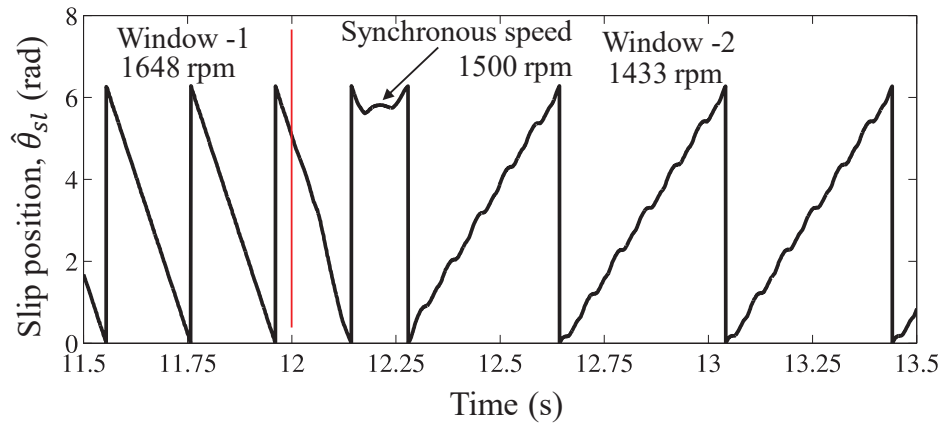
(a)



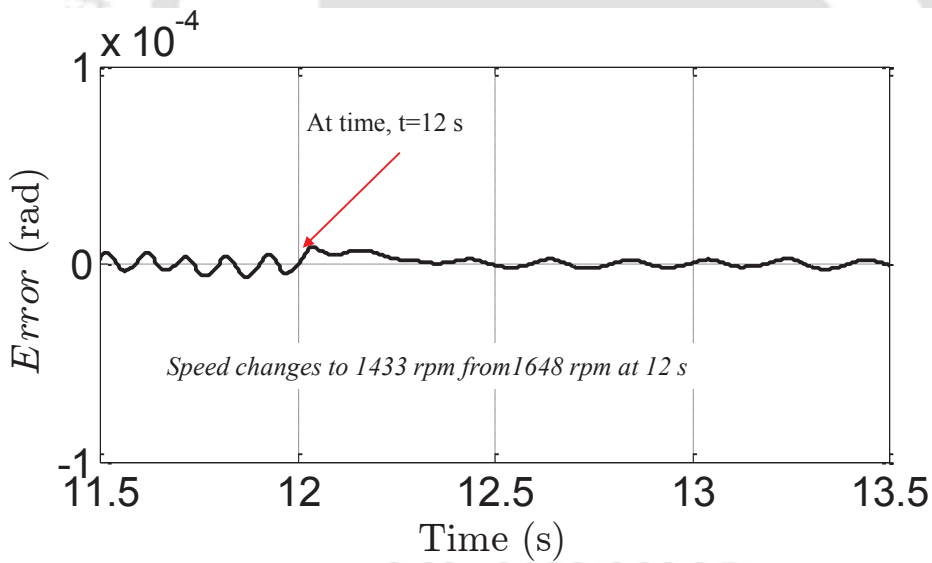
(b)

Figure 2.5: Speed change: (a) Slip position during sub synchronous to super synchronous speed variation, (b) The estimation error plot for speed change to supersynchronous from subsynchronous.

2. Stator Flux Based Slip Angle Estimation



(a)



(b)

Figure 2.6: Speed change: (a) Slip position during super synchronous to sub synchronous speed variation, (b) The estimation error plot for speed change to subsynchronous from supersynchronous.

corresponding estimation errors of the rotor position $\hat{\theta}_r$, are plotted in Figures 2.7 and 2.6(b). Here, it is observed that in both cases, the observer algorithm converges within 0.05 s.

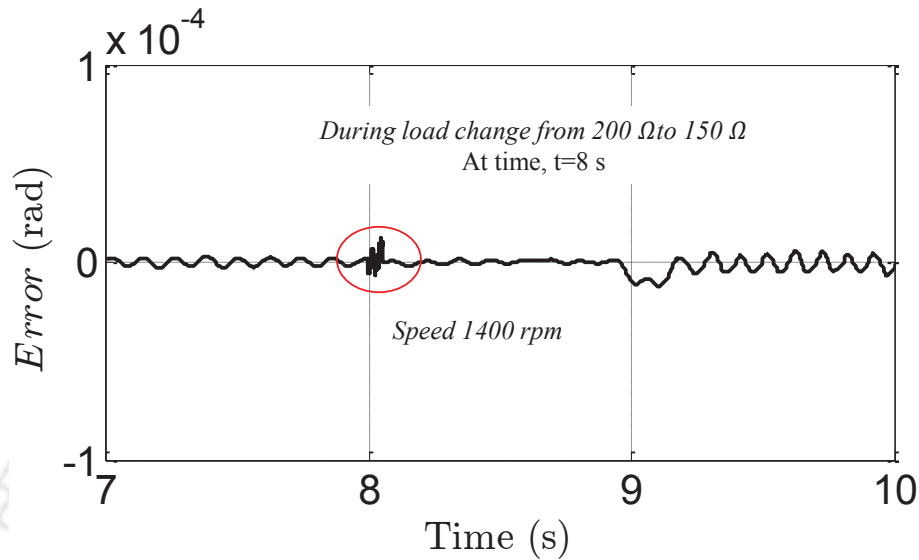


Figure 2.7: The estimation error plot during load change

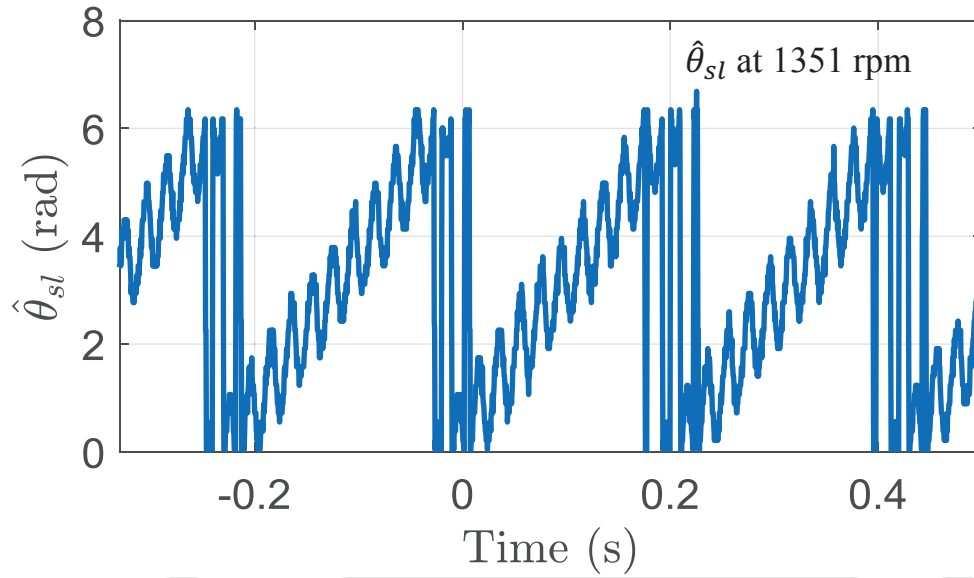
2.5.2 Case 2: Load Change Response

A three phase resistive load is connected to the stator terminal of the machine to verify the effectiveness of the observer. In this case, machine is running at 1400 rpm and at $t = 8$ s, resistive load is changed from 200 Ω to 150 Ω . The corresponding error during load change operation is plotted in Figure 2.7. The estimation error converges at less than 0.05 s.

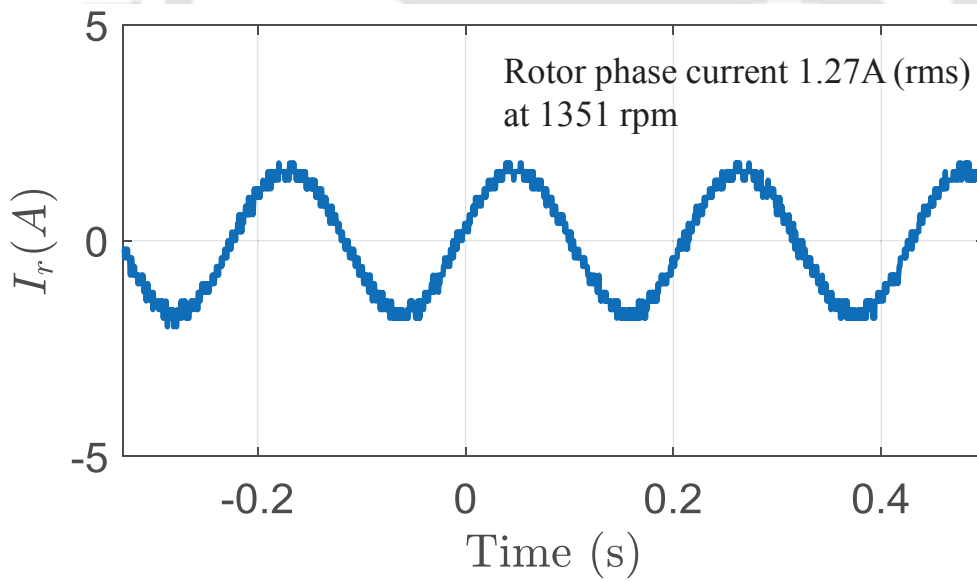
It is observed that in all the given test conditions, the estimation error of the rotor position estimation algorithm is within the range of 5×10^{-4} rad.

2.6 Experimental Results:

The suggested observer algorithm is realized with the help of TMS320F28335 DSP having a PC interface. LEM Hall-effect current sensors are utilized to sense the real time stator and rotor side currents of the DFIG. The stator voltage and dc link voltage are also measured by employing Hall-effect voltage sensor. The PWM converter is made of IGBTs (IPM) driven by optocoupler based gate driver. The necessary hardware details of the sensors circuits and related signal-conditioning circuits and the parameters of the machine are given in Appendix A. The oscilloscope data are stored in the PC. In order to test the effectiveness of the estimator, it has been tested under the following conditions:



(a)



(b)

Figure 2.8: Experimental results for operation at rotor speed of 1351 rpm

- (1) DFIG operation with constant rotor speeds of 1351 rpm.
- (2) A Step change of DFIG speed from 1470 rpm to 1430 rpm.
- (3) A sudden load change from 300 Ω to 150 Ω .

2.6.1 Case 1: Constant Rotor Speed Operation

The rotor slip position and rotor phase current at steady state with constant speed operation of DFIG is shown in Figure 2.8(a) and 2.8(b), respectively. The obtained rotor mechanical speed is 1351rpm.

2.6.2 Case 2: Step Change in Speed Reference

A step change of speed is applied to the rotor shaft by changing the DC motor shaft speed to verify the effectiveness of the algorithm. Figure 2.9(a) presents the rotor slip position with respect to the rotor speed. The corresponding rotor current waveform is given in Figure 2.9(b). The results show a stable operation during step change of the speed and also near to the synchronous speed. In both the Figures, Window -1 and Window -2 represents the operating speed of 1470 rpm and 1430 rpm, respectively.

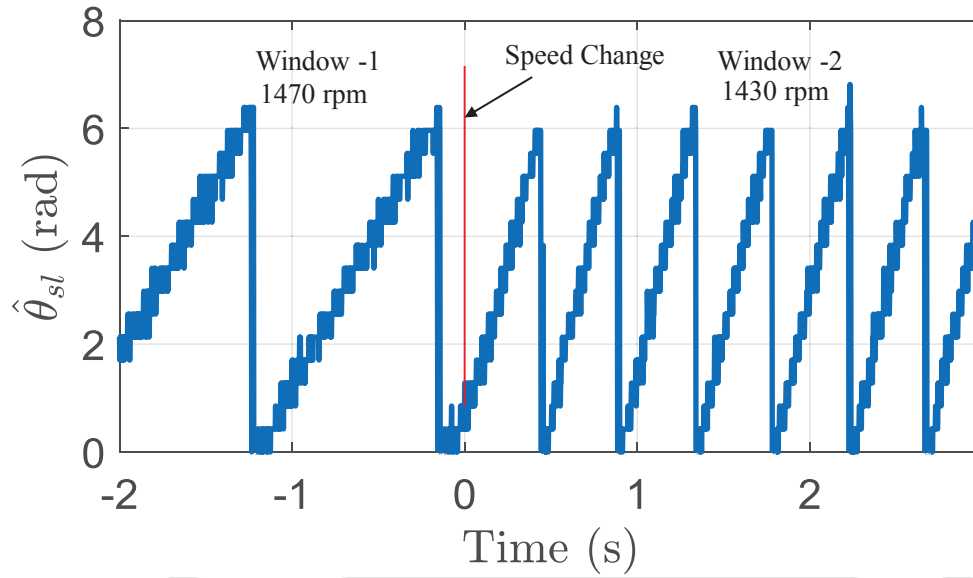
2.6.3 Case 3: Sudden Change in Load Connected to the Stator Terminal

A load change is applied from 300 Ω to 150 Ω . During load change, the slip position and rotor phase current is shown in Figure 2.10(a) and 2.10(b), respectively. In the given figures, Window -1 represents the operation at 300 Ω load and Window -2 represents the operation at 150 Ω load.

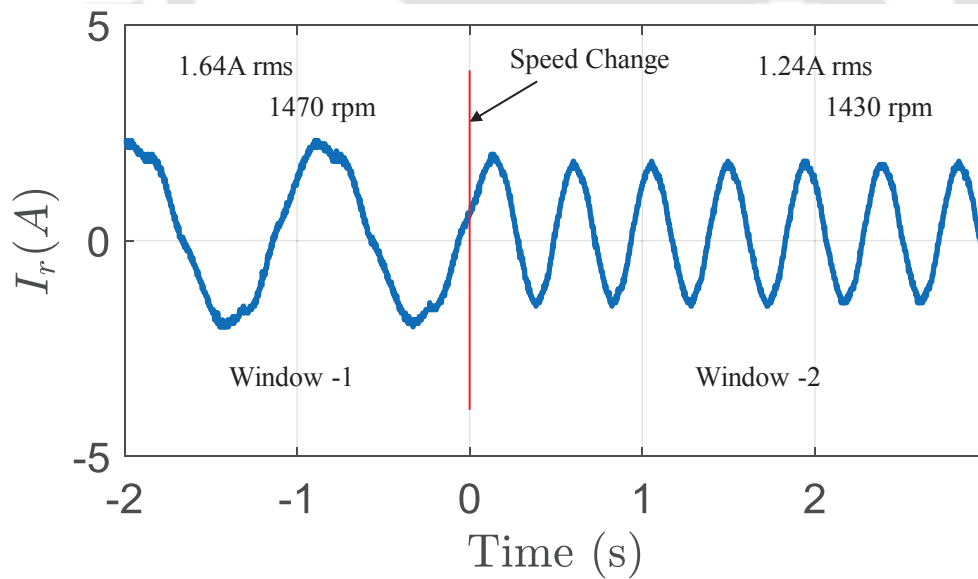
2.7 Conclusion

In this chapter a stator flux based slip position estimation algorithm is introduced. A detailed stability analysis of the above mentioned algorithm has been done and the permissible range of estimator gain is calculated. The working of the proposed estimator has been simulated in PSCAD Software. The proposed estimator shows a good response when the rotor speed is within $\pm 30\%$ of the synchronous speed. Further, the response of the algorithm appears to be stable under a sudden change of speed reference. The response of the estimator has also been simulated for the case where the load varies at the stator terminals of the machine. The performance of the estimator is found to be satisfactory therein.

2. Stator Flux Based Slip Angle Estimation



(a)



(b)

Figure 2.9: Experimental results for speed change from 1470 rpm to 1430 rpm.

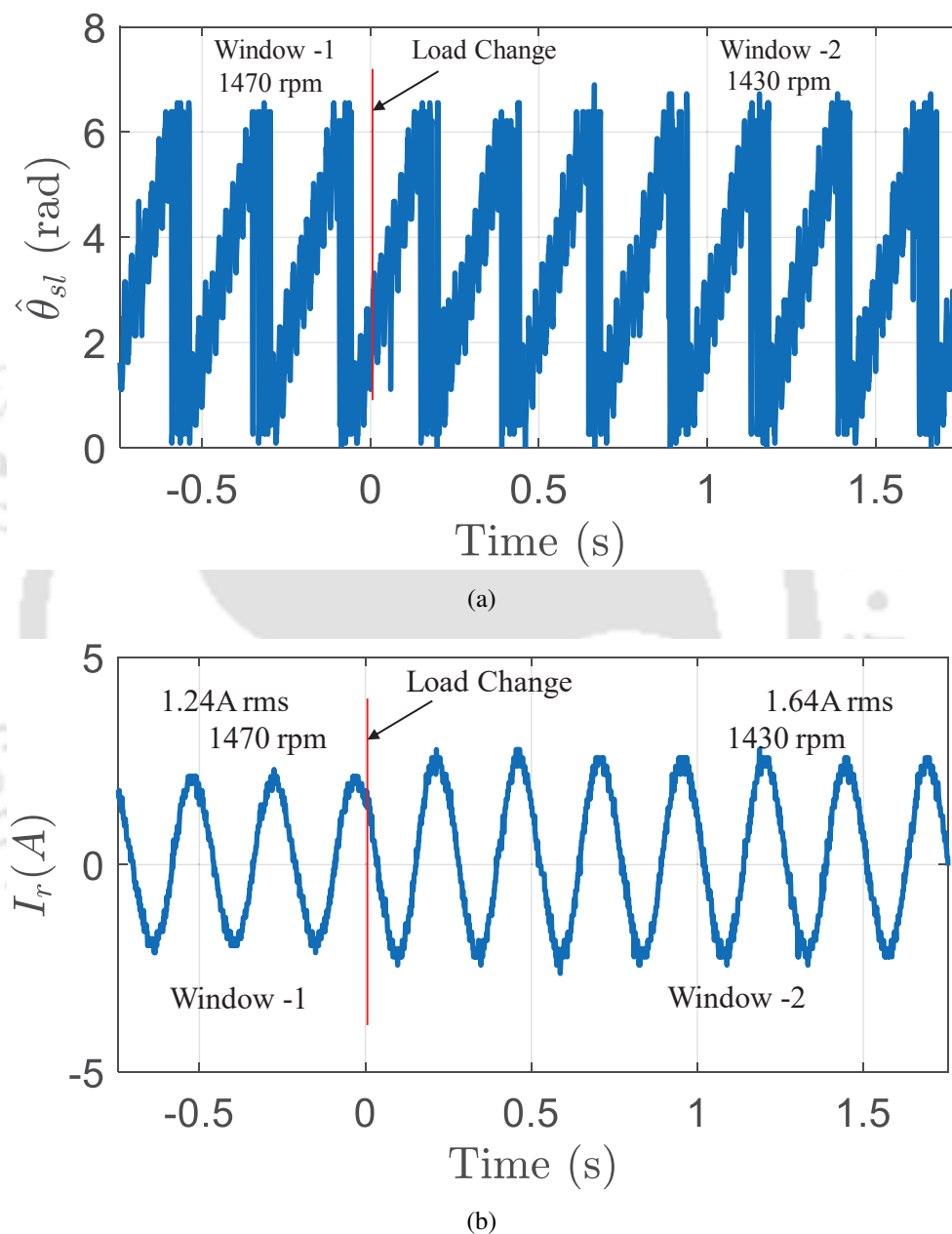


Figure 2.10: Experimental results for load change from 300 Ω to 150 Ω

2. Stator Flux Based Slip Angle Estimation

The work includes the practical implementation and testing of the proposed algorithm on an actual DFIG system.



3

Robust Slip Angle Speed Estimation Technique Using the Measurement of Rotor Current

Contents

3.1	Introduction	34
3.2	Stator Voltage Oriented Reference Frame	34
3.3	Proposed Estimation Method	35
3.4	Stability Analysis	44
3.5	Simulation Results	47
3.6	Experimental Results	60
3.7	Conclusion	66

3.1 Introduction

Chapter 2 discussed a stator flux-based rotor slip-position estimator. Though the method has less complexity, it depends on the encoder feedback. Moreover, the accuracy of the estimated slip position is less and varies with the change in speed of rotor. To overcome the above problems, this chapter proposes rotor current based an adaptive speed and slip position estimator (ASSPE) for a DFIG system.

In this chapter, a new closed loop speed and slip position observer for both standalone and grid connected DFIG system, is proposed. Unlike other schemes discussed in literature, the proposed observer does not include integration of flux and voltage. This method uses the measured values of the stator and rotor currents, and stator voltages. Moreover, the proposed method only requires the stator inductance parameter which can be easily measured from the machine. The stability of the observer is also analyzed. In order to test the proposed method, a laboratory based setup is used. The hardware details of the setup is given in Appendix A. The estimation algorithm is implemented in TMS320F28335-floating point digital signal processor. The stator voltage oriented reference frame is explained in next section.

3.2 Stator Voltage Oriented Reference Frame

The stator voltage oriented control is achieved by aligning the d-axis of the synchronous reference frame with the stator voltage vector \vec{v}_s . The resultant d- and q-axis stator voltages are $v_{ds} = V_m$ and $v_{qs} = 0$. In general, the grid voltage vector angle θ_g is calculated from the PLL which is used to transform the generated 3-phase stator voltage and current into the dq frame. The rotor position angle θ_r is measured by an encoder mounted on the shaft of the machine and the slip angle is obtained by $\theta_{sl} = \theta_s - \theta_r$. The encoder has many limitations such as reliability, mounting, robustness and noise which necessitates the use of a sensorless algorithm to accurately estimate the rotor/slip position. Figure 3.1 shows the synchronous reference frame (dq) rotates at synchronous speed, ω_s with respect to the stationary reference frame ($\alpha\beta$) and the rotor reference frame (ab) rotates at the angular velocity, ω_r .

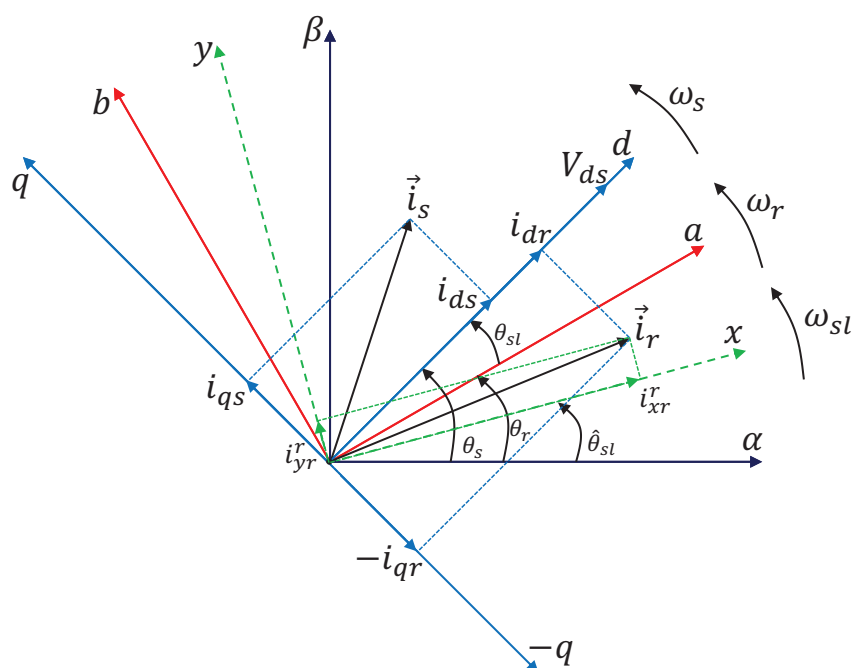


Figure 3.1: Angular relations of current and voltage vectors for DFIG.

3.3 Proposed Estimation Method

In this section, a closed-loop slip angle estimator is presented. The proposed estimation algorithm takes the stator voltages, currents, and rotor currents as inputs. The observer consists of two stages. The first stage estimates the slip position. Further, it uses the estimated slip position to transform the rotor current components into the xy reference frame from ab frame shown in Figure 3.1. Note that the xy frame rotates at slip speed and frequency of the rotor current is ω_r in xy reference frame.

The second stage takes the rotor current components (xy - reference frame) generated by the first stage and estimates its frequency. This is taken as an estimate of rotor speed.

3.3.1 Rotor Slip Angle Estimation

The first stage is implemented using the stator voltage orientated reference frame. Here, the d -axis is aligned with the stator voltage \vec{V}_s . The grid voltage vector angle is calculated using the Synchronous Reference Frame-Phase Locked Loop (SRFPLL) which is used to transform the generated 3-phase stator voltage and current into the dq frame. Once the generator is synchronized with the grid, the stator voltage vector angle θ_s and the grid voltage vector angle will be the same. Figure 3.1 shows the synchronous reference frame (dq), which rotate at synchronous speed (ω_s) with respect to the $\alpha\beta$ reference frame. The rotor reference frame, ab rotates at the speed of ω_r .

3. Robust Slip Angle Speed Estimation Technique Using the Measurement of Rotor Current

In practice, DFIG has a turns ratio, (n) and it should be included in the dynamic equations of the machine. The equivalent circuit of DFIG is shown in Appendix B. From the equivalent circuit, the stator flux-linkages in d - q axis are given by

$$\psi_{ds} = nL_s i_{ds} + L_m i_{dr} \quad (3.1)$$

$$\psi_{qs} = nL_s i_{qs} + L_m i_{qr}. \quad (3.2)$$

From (3.1) and (3.2), the d - q axis stator currents are calculated by

$$i_{ds} = \frac{\psi_{ds} - L_m i_{dr}}{nL_s} \quad (3.3)$$

$$i_{qs} = \frac{\psi_{qs} - L_m i_{qr}}{nL_s} \quad (3.4)$$

From the equivalent circuit, at steady state, the stator voltage vector of the machine is represented as

$$\vec{V}_s = R_s \vec{i}_s + j\omega_s \vec{\psi}_s. \quad (3.5)$$

Equation (3.5) in d - q axis can be written as

$$V_{ds} + jV_{qs} = \{R_s i_{ds} - \omega_s \psi_{qs}\} + j\{R_s i_{qs} + \omega_s \psi_{ds}\}. \quad (3.6)$$

Therefore, from (3.6), the steady-state d - q axis flux linkages are

$$\psi_{ds} = \frac{V_{qs} - R_s i_{qs}}{\omega_s} \quad (3.7)$$

$$\psi_{qs} = -\frac{V_{ds} - R_s i_{ds}}{\omega_s}. \quad (3.8)$$

The generated stator active and reactive power can be calculated by

$$P_s = \frac{3}{2} \{V_{ds} i_{ds} + V_{qs} i_{qs}\} \quad (3.9)$$

$$Q_s = \frac{3}{2} \{V_{qs} i_{ds} - V_{ds} i_{qs}\} \quad (3.10)$$

Applying the stator voltage oriented control [$V_{ds} = V_m$ (peak voltage of the phase), $V_{qs} = 0$], (3.9)

and (3.10) can be simplified to

$$P_s = \frac{3}{2} V_{ds} i_{ds} \quad (3.11)$$

$$Q_s = -\frac{3}{2} V_{ds} i_{qs} \quad (3.12)$$

Finally, from (3.1) to (3.12), the dq -axis rotor current components are derived as follows:

$$i_{dr} = -\frac{2}{3} \frac{nL_s}{V_{ds} L_m} P_s - \frac{R_s i_{qs}}{\omega_s L_m} \quad (3.13)$$

$$i_{qr} = \frac{2}{3} \frac{nL_s}{V_{ds} L_m} Q_s - \frac{V_{ds}}{\omega_s L_m} - \frac{R_s i_{ds}}{\omega_s L_m} \quad (3.14)$$

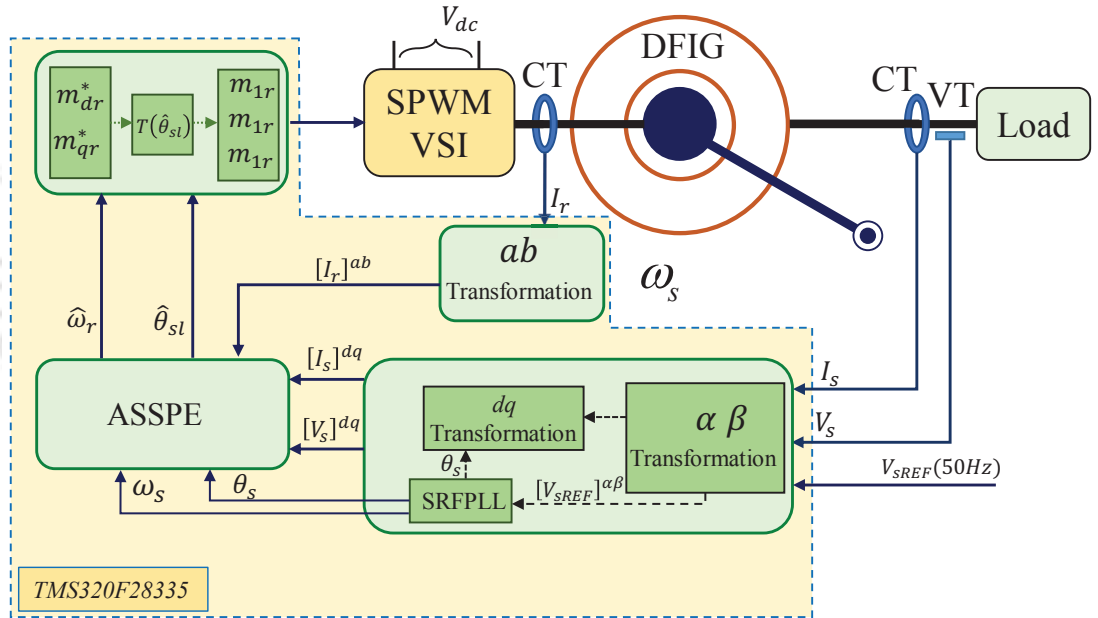


Figure 3.2: Schematic block diagram of ASSP Estimator (Adaptive Speed and Slip Position Estimator)

Neglecting the stator resistance R_s in (3.13) and (3.14), we have

$$i_{dr} = -\frac{2}{3} \frac{nL_s}{V_{ds} L_m} P_s \quad (3.15)$$

$$i_{qr} = \frac{2}{3} \frac{nL_s}{V_{ds} L_m} Q_s - \frac{V_{ds}}{\omega_s L_m} \quad (3.16)$$

Negative sign of the P_s and Q_s in (3.17) and (3.18), signifies the direction of power flow from the

3. Robust Slip Angle Speed Estimation Technique Using the Measurement of Rotor Current

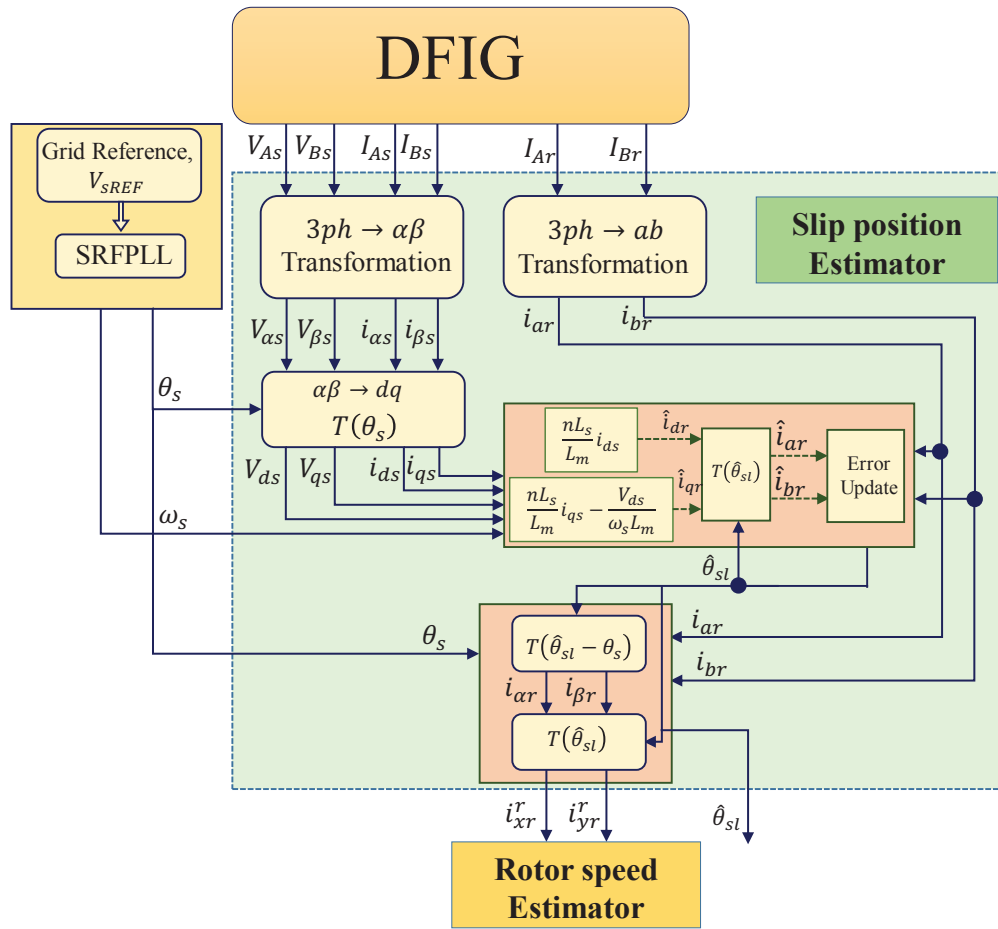


Figure 3.3: Schematic block diagram of slip position estimator

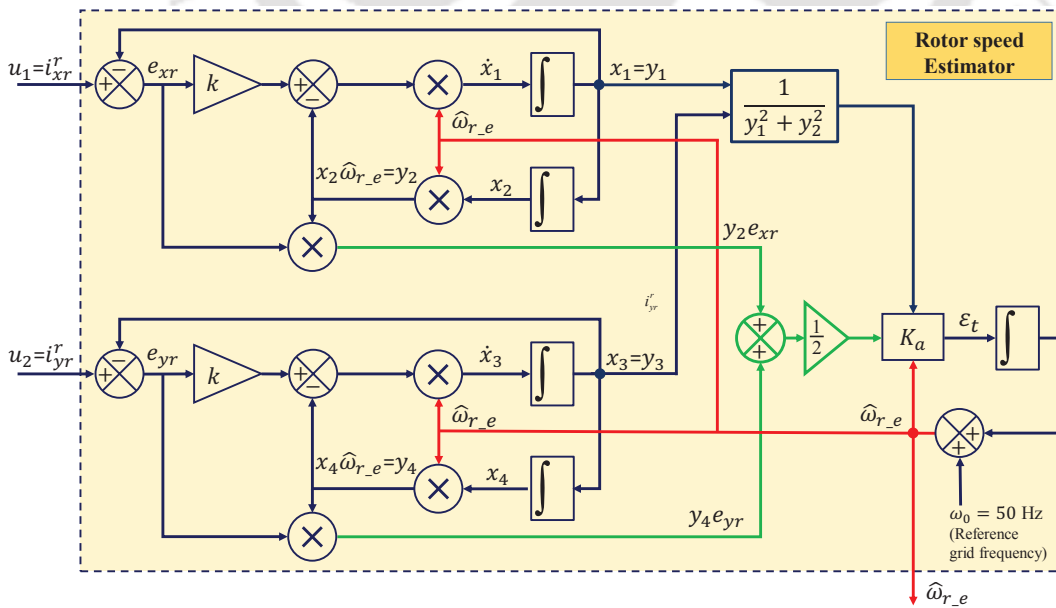


Figure 3.4: Schematic block diagram of rotor speed estimator

stator to grid. Therefore, equations (3.15) and (3.16) are rewritten as,

$$\begin{aligned}
 i_{dr} &= -\frac{2}{3} \frac{nLs}{V_{ds}L_m} (-P_s) \\
 &= -\frac{2}{3} \frac{nLs}{V_{ds}L_m} \left\{ -\frac{3}{2} V_{ds} i_{ds} \right\} \\
 &= \frac{nLs}{L_m} i_{ds}
 \end{aligned} \tag{3.17}$$

$$\begin{aligned}
 i_{qr} &= \frac{2}{3} \frac{nLs}{V_{ds}L_m} (-Q_s) - \frac{V_{ds}}{\omega_s L_m} \\
 &= \frac{2}{3} \frac{nLs}{V_{ds}L_m} \left\{ -\frac{3}{2} V_{ds} i_{qs} \right\} - \frac{V_{ds}}{\omega_s L_m} \\
 &= \frac{nLs}{L_m} i_{qs} - \frac{V_{ds}}{\omega_s L_m}
 \end{aligned} \tag{3.18}$$

The dq -axis rotor current components (i_{dr}, i_{qr}) are transformed into the rotor reference frame (ab) using inverse Park transformation. The rotor current components (i_{ar}, i_{br}) in ab frame are given by

$$\begin{bmatrix} i_{ar} \\ i_{br} \end{bmatrix} = \begin{bmatrix} \cos \theta_{sl} & -\sin \theta_{sl} \\ \sin \theta_{sl} & \cos \theta_{sl} \end{bmatrix} \begin{bmatrix} i_{dr} \\ i_{qr} \end{bmatrix} \tag{3.19}$$

Substituting i_{dr} and i_{qr} into (3.19) gives

$$i_{ar} = \frac{nLs}{L_m} i_{ds} \cos \theta_{sl} - \left\{ \frac{nLs}{L_m} i_{qs} - \frac{V_{ds}}{\omega_s L_m} \right\} \sin \theta_{sl} \tag{3.20}$$

$$i_{br} = \frac{nLs}{L_m} i_{ds} \sin \theta_{sl} + \left\{ \frac{nLs}{L_m} i_{qs} - \frac{V_{ds}}{\omega_s L_m} \right\} \cos \theta_{sl} \tag{3.21}$$

Thus, the rotor current components are determined in (3.20) and (3.21) depend on the measured stator voltage and current.

Further, based on the measured actual rotor current and using Clark transformation, the rotor

3. Robust Slip Angle Speed Estimation Technique Using the Measurement of Rotor Current

current components in rotor reference frame are given by

$$i_{ar} = I_{Ar} \quad (3.22)$$

$$i_{br} = \frac{1}{\sqrt{3}}(I_{Ar} + 2I_{Br}) \quad (3.23)$$

Given an estimated slip angle equations (3.20) and (3.21) can be used to estimate the rotor current components. If the slip angle estimate is accurate then the estimated rotor current vector $\hat{\mathbf{i}}_r = [\hat{i}_{ar} \hat{i}_{br}]^T$ and the measured rotor current vector $\mathbf{i}_r = [i_{ar} i_{br}]^T$ will have the same direction. Consequently, the cross product of $\hat{\mathbf{i}}_r$ and \mathbf{i}_r will be equal to zero, i.e. $\hat{\mathbf{i}}_r \times \mathbf{i}_r = 0$. Therefore, $e = \hat{\mathbf{i}}_r \times \mathbf{i}_r$ is used as a measure for the angle estimation error. Further, e can be written as follows,

$$e = \hat{i}_{ar}i_{br} - \hat{i}_{br}i_{ar} \quad (3.24)$$

$$= |\hat{I}_r| |I_r| \sin(\theta_{sl} - \hat{\theta}_{sl}) \quad (3.25)$$

The slip angle is estimated using a predictor-corrector scheme. At time instant k , the predicted and corrected values of slip angle are denoted by $\hat{\theta}_{slp}(k)$ and $\hat{\theta}_{sl}(k)$ respectively. The estimated slip and rotor velocities are denoted by $\hat{\omega}_{sl,e}(k)$ and $\hat{\omega}_{r,e}(k)$, respectively. Using the estimates of the slip angle and velocity at the previous time instant, the predicted value of slip angle is given as

$$\hat{\theta}_{slp}(k) = \hat{\theta}_{sl}(k-1) + \hat{\omega}_{sl,e}(k-1)\Delta t. \quad (3.26)$$

where Δt is the sampling time. This predicted slip angle is used to estimate the rotor current in the ab reference frame.

$$\hat{i}_{ar}(k) = \frac{nLs}{L_m} i_{ds} \cos(\hat{\theta}_{slp}(k)) - \left\{ \frac{nLs}{L_m} i_{qs} - \frac{v_{ds}}{\omega_s L_m} \right\} \sin(\hat{\theta}_{slp}(k)) \quad (3.27)$$

$$\hat{i}_{br}(k) = \frac{nLs}{L_m} i_{ds} \sin(\hat{\theta}_{slp}(k)) + \left\{ \frac{nLs}{L_m} i_{qs} - \frac{v_{ds}}{\omega_s L_m} \right\} \cos(\hat{\theta}_{slp}(k)) \quad (3.28)$$

An error signal is then generated by taking a cross product of the estimated and measured rotor current vectors.

$$e(k) = \hat{\mathbf{i}}_r(\mathbf{k}) \times \mathbf{i}_r(\mathbf{k}) \quad (3.29)$$

This error is used to correct the predicted slip angle and generate the slip angle estimate at that time instant. The corrected value of slip angle is given by:

$$\hat{\theta}_{sl}(k) = \hat{\theta}_{slp}(k) + K_{sp}e(k) \quad (3.30)$$

where K_{sp} is the correction gain.

The proposed predictor-corrector algorithm can be summarized as follows:

Algorithm

$$\begin{aligned} \hat{\theta}_{slp}(k) &= \hat{\theta}_{sl}(k-1) + \hat{\omega}_{sl.e}(k-1)\Delta t. \\ \hat{i}_{ar}(k) &= \frac{nL_s}{L_m}i_{ds} \cos(\hat{\theta}_{slp}(k)) - \left\{ \frac{nL_s}{L_m}i_{qs} - \frac{v_{ds}}{\omega_s L_m} \right\} \sin(\hat{\theta}_{slp}(k)) \\ \hat{i}_{br}(k) &= \frac{nL_s}{L_m}i_{ds} \sin(\hat{\theta}_{slp}(k)) + \left\{ \frac{nL_s}{L_m}i_{qs} - \frac{v_{ds}}{\omega_s L_m} \right\} \cos(\hat{\theta}_{slp}(k)) \\ e(k) &= \hat{\mathbf{i}}_r(\mathbf{k}) \times \mathbf{i}_r(\mathbf{k}) \\ \hat{\theta}_{sl}(k) &= \hat{\theta}_{slp}(k) + K_{sp}e(k) \end{aligned}$$

3.3.2 Rotor Speed Estimation

In this section, we present a closed loop rotor speed estimation technique. This technique uses the estimated slip position, $\hat{\theta}_{sl}$ and the measured rotor current components as inputs. The estimated slip position, $\hat{\theta}_{sl}$ is used to generate the rotor position estimate, $\hat{\theta}_r$ as follows,

$$\hat{\theta}_r = \theta_s - \hat{\theta}_{sl}. \quad (3.31)$$

The structure of the proposed estimation technique is shown in Figure 3.4. The measured rotor currents are transformed to rotor rotating frame using $\hat{\theta}_r$, as follows,

$$i_{dr} = i_{ar} \cos \hat{\theta}_{sl} + i_{br} \sin \hat{\theta}_{sl} \quad (3.32)$$

$$i_{qr} = -i_{ar} \sin \hat{\theta}_{sl} + i_{br} \cos \hat{\theta}_{sl} \quad (3.33)$$

$$i_{\alpha r} = i_{dr} \cos \hat{\theta}_r - i_{qr} \sin \hat{\theta}_r \quad (3.34)$$

$$i_{\beta r} = i_{dr} \sin \hat{\theta}_r + i_{qr} \cos \hat{\theta}_r \quad (3.35)$$

3. Robust Slip Angle Speed Estimation Technique Using the Measurement of Rotor Current

The rotor current components in rotor electrical speed reference frame can be computed as follows,

$$i_{xr}^r = i_{\alpha r} \cos \hat{\theta}_{sl} + i_{\beta r} \sin \hat{\theta}_{sl} \quad (3.36)$$

$$i_{yr}^r = -i_{\alpha r} \sin \hat{\theta}_{sl} + i_{\beta r} \cos \hat{\theta}_{sl} \quad (3.37)$$

From Figure 3.4, we get the following space-state equations for rotor speed estimator:

$$\dot{x}_1 = -k\hat{\omega}_{r,e}x_1 - \hat{\omega}_{r,e}^2x_2 + k\hat{\omega}_{r,e}u_1 \quad (3.38)$$

$$\dot{x}_2 = x_1 \quad (3.39)$$

$$\dot{x}_3 = -k\hat{\omega}_{r,e}x_3 - \hat{\omega}_{r,e}^2x_4 + k\hat{\omega}_{r,e}u_2 \quad (3.40)$$

$$\dot{x}_4 = x_3 \quad (3.41)$$

$$y_1 = x_1 \quad (3.42)$$

$$y_2 = \hat{\omega}_{r,e}x_2 \quad (3.43)$$

$$y_3 = x_3 \quad (3.44)$$

$$y_4 = \hat{\omega}_{r,e}x_4 \quad (3.45)$$

where $x_1 = \hat{i}_{xr}^r$ and $x_3 = \hat{i}_{yr}^r$ are the estimates of input u_1 and u_2 respectively. The inputs $u_1 = i_{xr}^r$ and $u_2 = i_{yr}^r$, respectively. Equations (3.38)-(3.45) describe the dynamic behaviour of the rotor speed estimator. The errors can be written as

$$e_{xr} = u_1 - x_1 \quad (3.46)$$

$$e_{yr} = u_2 - x_3 \quad (3.47)$$

In steady-state, from (3.38) and (3.40), the errors can be written as

$$e_{xr} = u_1 - x_1 = \frac{1}{k\hat{\omega}_{r,e}}(\dot{x}_1 + \hat{\omega}_{r,e}^2x_2) \quad (3.48)$$

$$e_{yr} = u_2 - x_3 = \frac{1}{k\hat{\omega}_{r,e}}(\dot{x}_3 + \hat{\omega}_{r,e}^2x_4). \quad (3.49)$$

The x_1 and x_3 are sinusoidal at the frequency $\hat{\omega}_r$ ($\hat{\omega}_r \neq \hat{\omega}_{r,e}$), from (3.38) and (3.40) the state

variables can be written as

$$\dot{x}_1 = -\hat{\omega}_r^2 x_2 \quad (3.50)$$

$$\dot{x}_3 = -\hat{\omega}_r^2 x_4 \quad (3.51)$$

Substituting (3.50) and (3.51) into (3.48) and (3.49), respectively, the phase error e_{xr} and e_{yr} can be written as

$$e_{xr} = \frac{x_2}{k\hat{\omega}_{r,e}}(\hat{\omega}_{r,e}^2 - \hat{\omega}_r^2) \quad (3.52)$$

$$e_{yr} = \frac{x_4}{k\hat{\omega}_{r,e}}(\hat{\omega}_{r,e}^2 - \hat{\omega}_r^2) \quad (3.53)$$

Therefore,

$$y_2 e_{xr} = \frac{x_2^2}{k}(\hat{\omega}_{r,e}^2 - \hat{\omega}_r^2) \quad (3.54)$$

$$y_4 e_{yr} = \frac{x_4^2}{k}(\hat{\omega}_{r,e}^2 - \hat{\omega}_r^2). \quad (3.55)$$

where, $y_2 = x_2 \hat{\omega}_{r,e}$ and $y_4 = x_4 \hat{\omega}_{r,e}$. The average frequency error signal can be calculated as

$$\varepsilon_t = \frac{y_2 e_{xr} + y_4 e_{yr}}{2} \quad (3.56)$$

From Figure 3.4, the $\hat{\omega}_{r,e}$ is given by,

$$\begin{aligned} \dot{\hat{\omega}}_{r,e} &= -K_a \varepsilon_t \\ &= -\frac{K_a(x_2^2 + x_4^2)}{2k}(\hat{\omega}_{r,e}^2 - \hat{\omega}_r^2) \\ &= -\frac{K_a(x_1^2 + x_3^2)}{2k\hat{\omega}_{r,e}^2}(\hat{\omega}_{r,e}^2 - \hat{\omega}_r^2) \end{aligned} \quad (3.57)$$

If $\hat{\omega}_{r,e}$ is sufficiently close to $\hat{\omega}_r$, then $(\hat{\omega}_{r,e}^2 - \hat{\omega}_r^2)$ can be approximated by $2(\hat{\omega}_{r,e} - \hat{\omega}_r)\hat{\omega}_{r,e}$. Therefore,

$$\begin{aligned} \dot{\hat{\omega}}_{r,e} &= -\frac{K_a I_r^2}{k\hat{\omega}_{r,e}^2}(\hat{\omega}_r - \hat{\omega}_r)\hat{\omega}_{r,e} \\ &= -\frac{K_a I_r^2}{k\hat{\omega}_{r,e}}(\hat{\omega}_{r,e} - \hat{\omega}_r) \end{aligned} \quad (3.58)$$

where the gain $K_a = \frac{k\hat{\omega}_{r,e}}{I_r^2} G$. Therefore, the transfer function of the first-order frequency estimation

loop can be written by

$$\frac{\hat{\omega}_{r,e}}{\hat{\omega}_r} = \frac{G}{s + G} \quad (3.59)$$

Thus, if $\hat{\omega}_{r,e}$ is initialized to a value close to $\hat{\omega}_r$, then $\hat{\omega}_{r,e}$ will asymptotically approach $\hat{\omega}_r$ at a rate which depends on G . This in turn will cause e_{xr} and e_{yr} to asymptotically go to zero (from (3.52) and (3.53)). For a first order closed loop system, the settling time t_s , can be set to 4 times of the time constant for practical implementation, as shown in Figure 3.4.

3.4 Stability Analysis

In this section, we analyze the stability of the proposed algorithm. We prove that the convergence of the rotor velocity algorithm leads to the convergence of the slip position estimation algorithm.

The error signal, $e(k)$ is given by

$$e(k) = \hat{\mathbf{i}}_r(\mathbf{k}) \times \mathbf{i}_r(\mathbf{k}) = |\hat{I}_r| |I_r| \sin(\theta_\Delta(k)) \quad (3.60)$$

where, $\theta_\Delta(k) = \theta_{sl}(k) - \hat{\theta}_{sl}(k)$. Therefore, $\theta_\Delta(k) = \frac{e(k)}{\lambda}$, where $\lambda = |\hat{I}_r| |I_r|$. From (3.26) and (3.30), the value of $\hat{\theta}_{sl}(k)$ can be written as:

$$\hat{\theta}_{sl}(k) = \hat{\theta}_{sl}(k-1) + \hat{\omega}_{sl,e}(k)\Delta t + K_{sp}e(k) \quad (3.61)$$

$$\therefore \Delta \hat{\theta}_{sl}(k) = \hat{\omega}_{sl,e}(k)\Delta t + K_{sp}e(k) \quad (3.62)$$

where $\hat{\omega}_{sl,e} = \omega_s - \hat{\omega}_{r,e}$. Let $\hat{\omega}_{sl}$ be the angular frequency of the signal, $\hat{\theta}_{sl}$. Therefore, $\Delta t \hat{\omega}_{sl} = \hat{\omega}_{sl}(k)\Delta t + O\{(\Delta t)^2\}$. Equation (3.62) can be rewritten as

$$\begin{aligned} \hat{\omega}_{sl}(k)\Delta t + O\{(\Delta t)^2\} &= \hat{\omega}_{sl,e}(k)\Delta t + K_{sp}e(k) \\ \{\hat{\omega}_{sl}(k) - \hat{\omega}_{sl,e}(k)\}\Delta t + O\{(\Delta t)^2\} &= K_{sp}e(k) \end{aligned} \quad (3.63)$$

For sufficiently small Δt , the $O\{(\Delta t)^2\}$ can be neglected. As a result, equation (3.63) becomes

$$[\{\omega_s(k) - \hat{\omega}_r(k)\} - \{\omega_s(k) - \hat{\omega}_{r,e}(k)\}]\Delta t = K_{sp}e(k) \quad (3.64)$$

$$\tilde{\omega}_{r,e}(k)\Delta t = K_{sp}e(k) \quad (3.65)$$

where $\tilde{\omega}_{r,e}$ is the rotor speed error, and ω_s is the grid frequency (50 Hz). Thus, the slip position error is proportional to the error in the second stage of the observer. This can be reduced by choosing a sufficiently high value for G from (3.59). Further, the slip position estimation error can be reduced by increasing the value of K_{sp} . However, as the error signal depends on the amplitude of measured current, a high value of K_{sp} will also amplify any noise in the signal. This trade off should be taken into account while tuning K_{sp} .

Second Stage: We now show that if input to the 2nd stage is sinusoidal with frequency $\hat{\omega}_r$, then the $\hat{\omega}_{r,e}$ will converge to $\hat{\omega}_r$.

Let $u_1 = \dot{\ell}_x = A \sin \hat{\omega}_r t$ and $u_2 = \dot{\ell}_y = -A \cos \hat{\omega}_r t$, where A is the peak magnitude of the rotor current. From (3.38),

$$\ddot{x}_2 + k\hat{\omega}_{r,e}\dot{x}_2 + \hat{\omega}_{r,e}^2 x_2 = k\hat{\omega}_{r,e}\dot{\ell}_x \quad (3.66)$$

and

$$\ddot{\ell}_x + k\hat{\omega}_r\dot{\ell}_x + \hat{\omega}_r^2 \ell_x = k\hat{\omega}_r\dot{\ell}_x \quad (3.67)$$

Subtracting (3.67) from (3.66), we get,

$$\ddot{x}_2 - \ddot{\ell}_x + k\hat{\omega}_{r,e}\dot{x}_2 - k\hat{\omega}_r\dot{\ell}_x + \hat{\omega}_{r,e}^2 x_2 - \hat{\omega}_r^2 \ell_x = k\hat{\omega}_{r,e}\dot{\ell}_x - k\hat{\omega}_r\dot{\ell}_x \quad (3.68)$$

$$(\ddot{x}_2 - \ddot{\ell}_x) + k\hat{\omega}_{r,e}(\dot{x}_2 - \dot{\ell}_x) + (\hat{\omega}_{r,e}^2 - \hat{\omega}_r^2)x_2 + \hat{\omega}_r^2(x_2 - \ell_x) = 0 \quad (3.69)$$

Let, $x_2 - \ell_x = e_x$ and $x_4 - \ell_y = e_y$, then

$$\ddot{e}_x + k\hat{\omega}_{r,e}^2 \dot{e}_x + (\hat{\omega}_{r,e}^2 - \hat{\omega}_r^2)e_x + \hat{\omega}_r^2 e_x = 0 \quad (3.70)$$

and similarly,

$$\ddot{e}_y + k\hat{\omega}_{r,e}^2 \dot{e}_y + (\hat{\omega}_{r,e}^2 - \hat{\omega}_r^2)e_y + \hat{\omega}_r^2 e_y = 0 \quad (3.71)$$

Now, multiplying \dot{e}_x with (3.70), and \dot{e}_y with (3.71), we get,

$$\overbrace{\dot{e}_x \ddot{e}_x + \dot{e}_y \ddot{e}_y + \hat{\omega}_r^2 (e_x \dot{e}_x + e_y \dot{e}_y)} + \overbrace{(\hat{\omega}_{r,e}^2 - \hat{\omega}_r^2) (x_2 \dot{e}_x + x_4 \dot{e}_y)} = -k\hat{\omega}_{r,e}^2 (\dot{e}_x^2 + \dot{e}_y^2) \quad (3.72)$$

3. Robust Slip Angle Speed Estimation Technique Using the Measurement of Rotor Current

Adding the term, $\left\{ \frac{(\hat{\omega}_{r,e} - \hat{\omega}_r)^2}{kG\hat{\omega}_{r,e}} (x_1\dot{x}_1 + x_3\dot{x}_3) \right\}$ in both side, we get

$$\overbrace{\dot{e}_x\ddot{e}_x + \dot{e}_y\ddot{e}_y + \hat{\omega}_r^2(e_x\dot{e}_x + e_y\dot{e}_y)} + \overbrace{(\hat{\omega}_{r,e}^2 - \hat{\omega}_r^2)(x_2\dot{e}_x + x_4\dot{e}_y) + \frac{(\hat{\omega}_{r,e} - \hat{\omega}_r)^2}{kG\hat{\omega}_{r,e}}(x_1\dot{x}_1 + x_3\dot{x}_3)} = -k\hat{\omega}_{r,e}^2(\dot{e}_x^2 + \dot{e}_y^2) \quad (3.73)$$

$$+ \frac{(\hat{\omega}_{r,e} - \hat{\omega}_r)^2}{kG\hat{\omega}_{r,e}}(x_1\dot{x}_1 + x_3\dot{x}_3)$$

Therefore,

$$p + q = -k\hat{\omega}_{r,e}^2(\dot{e}_x^2 + \dot{e}_y^2) + \frac{(\hat{\omega}_{r,e} - \hat{\omega}_r)^2}{kG\hat{\omega}_{r,e}}(x_1\dot{x}_1 + x_3\dot{x}_3) \quad (3.74)$$

where

$$p = \dot{e}_x\ddot{e}_x + \dot{e}_y\ddot{e}_y + \hat{\omega}_r^2(e_x\dot{e}_x + e_y\dot{e}_y) \quad (3.75)$$

$$= \frac{d}{dt} \left\{ (\dot{e}_x)^2 + (\dot{e}_y)^2 + \omega_r^2(e_x^2 + e_y^2) \right\}$$

$$q = (\hat{\omega}_{r,e}^2 - \hat{\omega}_r^2)(x_2\dot{e}_x + x_4\dot{e}_y) + \frac{(\hat{\omega}_{r,e} - \hat{\omega}_r)^2}{kG\hat{\omega}_{r,e}}(x_1\dot{x}_1 + x_3\dot{x}_3) \quad (3.76)$$

$$= \frac{1}{kG} \left\{ \frac{(\hat{\omega}_{r,e}^2 - \hat{\omega}_r^2)\hat{\omega}_{r,e}(x_1^2 + x_3^2)}{\hat{\omega}_{r,e}^2} + \frac{(\hat{\omega}_{r,e} - \hat{\omega}_r)^2}{\hat{\omega}_{r,e}}(x_1\dot{x}_1 + x_3\dot{x}_3) \right\}$$

$$= \frac{1}{kG} \frac{d}{dt} \left\{ \frac{(\hat{\omega}_{r,e} - \hat{\omega}_r)^2(x_1^2 + x_3^2)}{\hat{\omega}_{r,e}} \right\} \quad (3.77)$$

Let us consider, the Lyapunov function V is given by

$$V = v_1 + v_2 \quad (3.78)$$

where

$$v_1 = (\dot{e}_x)^2 + (\dot{e}_y)^2 + \hat{\omega}_r^2(e_x^2 + e_y^2) > 0 \quad (3.79)$$

$$v_2 = \frac{(\hat{\omega}_{r,e} - \hat{\omega}_r)^2(x_1^2 + x_3^2)}{\hat{\omega}_{r,e}} > 0. \quad (3.80)$$

The first derivative of the function V, is

$$\dot{V} = \dot{v}_1 + \dot{v}_2. \quad (3.81)$$

If $\hat{\omega}_{r,e}$ value is initialized to value sufficiently near $\hat{\omega}_r$, and the value of G is sufficiently high, then

$\left\{ \frac{(\hat{\omega}_{r,e} - \hat{\omega}_r)^2}{kG\hat{\omega}_{r,e}} (x_1\dot{x}_1 + x_3\dot{x}_3) \right\}$ can be considered negligible as compared to $-k\hat{\omega}_{r,e}^2(\dot{e}_x^2 + \dot{e}_y^2)$. Therefore, $\dot{v}_1 + \dot{v}_2 = p + q < 0$. This ensures the error asymptotically goes to zero.

3.5 Simulation Results

The performance of the proposed rotor speed and slip angle estimator is validated through simulation using the power system analysis software, PSCAD/EMTDC. The parameters of the machine, along with the systematic diagram of the simulation setup, are given in Appendix A. The results obtained from the simulation of the proposed estimator are compared with the actual value to know the accuracy of the proposed estimator under various test cases such as step change in rotor speed reference, and step changes in the load connected at the stator terminal. Further, the performance of the proposed algorithm has been tested with variation of mutual inductance, L_m to show its effectiveness.

3.5.1 Case 1: Step Change in Reference Input Speed

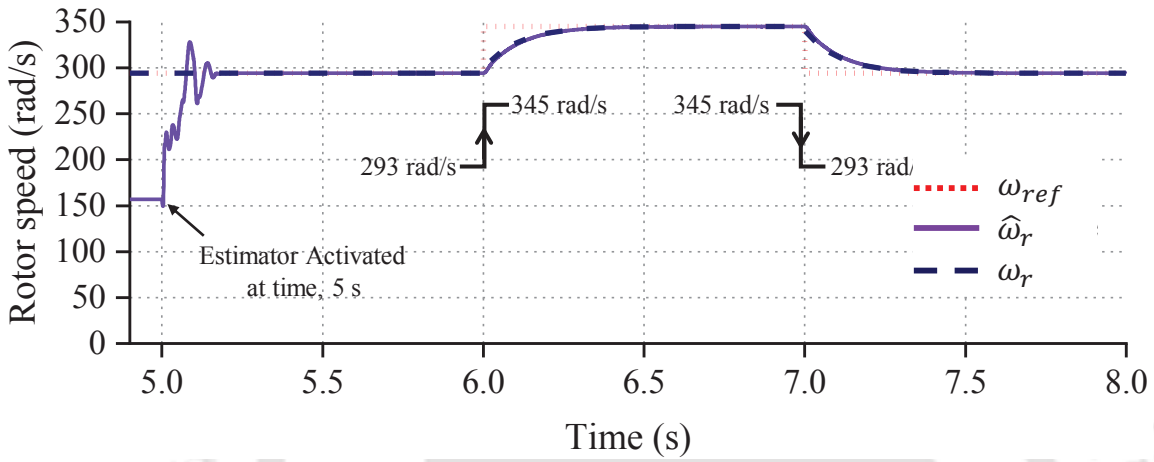
Initially, the machine runs at a sub-synchronous speed of 1400 rpm (293 rad/s electrical). A step-change in the reference speed is applied at $t = 6.0$ s in reference speed to change the machine speed from sub-synchronous to super-synchronous i.e., from 1400 rpm (293 rad/s electrical) to 1648 rpm (345 rad/s electrical). Similarly, at time $t = 7.0$ s, reference speed of the DFIG is changed from 1648 rpm (345 rad/s electrical) to 1400 rpm (293 rad/s), i.e., from super-synchronous to sub-synchronous. The reference speed (ω_{ref}), actual speed (ω_r) and estimated speed ($\hat{\omega}_r$) are shown in Figure 3.5(a). The corresponding error in the estimated speed is plotted in Figure 3.5(b). It is observed that the error in the estimated speed is less than 3% of the synchronous speed.

During the transition of the speed of DFIG from sub-synchronous to super-synchronous and vice versa, the estimated rotor slip position is shown in Figure 3.6(a). The corresponding error in the estimated rotor slip position is shown in Figure 3.6(b). It is observed that the error in the estimated rotor slip position is not more than ± 0.005 rad.

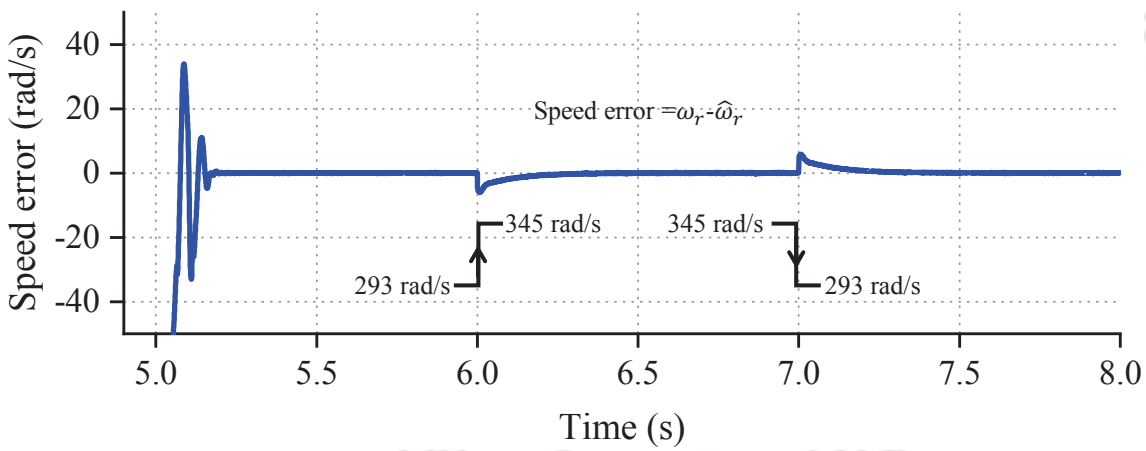
Further, to validate the accuracy of the proposed estimator, the estimated rotor current is compared with the actual rotor current in both ab and xy reference frame, and their corresponding plots are shown in Figures 3.7(a) and 3.7(b).

It is observed from Figure 3.7(a) that estimated \hat{i}_{ar} and \hat{i}_{br} converges to the measured rotor i_{ar} and

3. Robust Slip Angle Speed Estimation Technique Using the Measurement of Rotor Current



(a)



(b)

Figure 3.5: Plot during step change in reference input speed (a) estimated speed of the DFIG, (b) the corresponding error plot of the estimated speed.

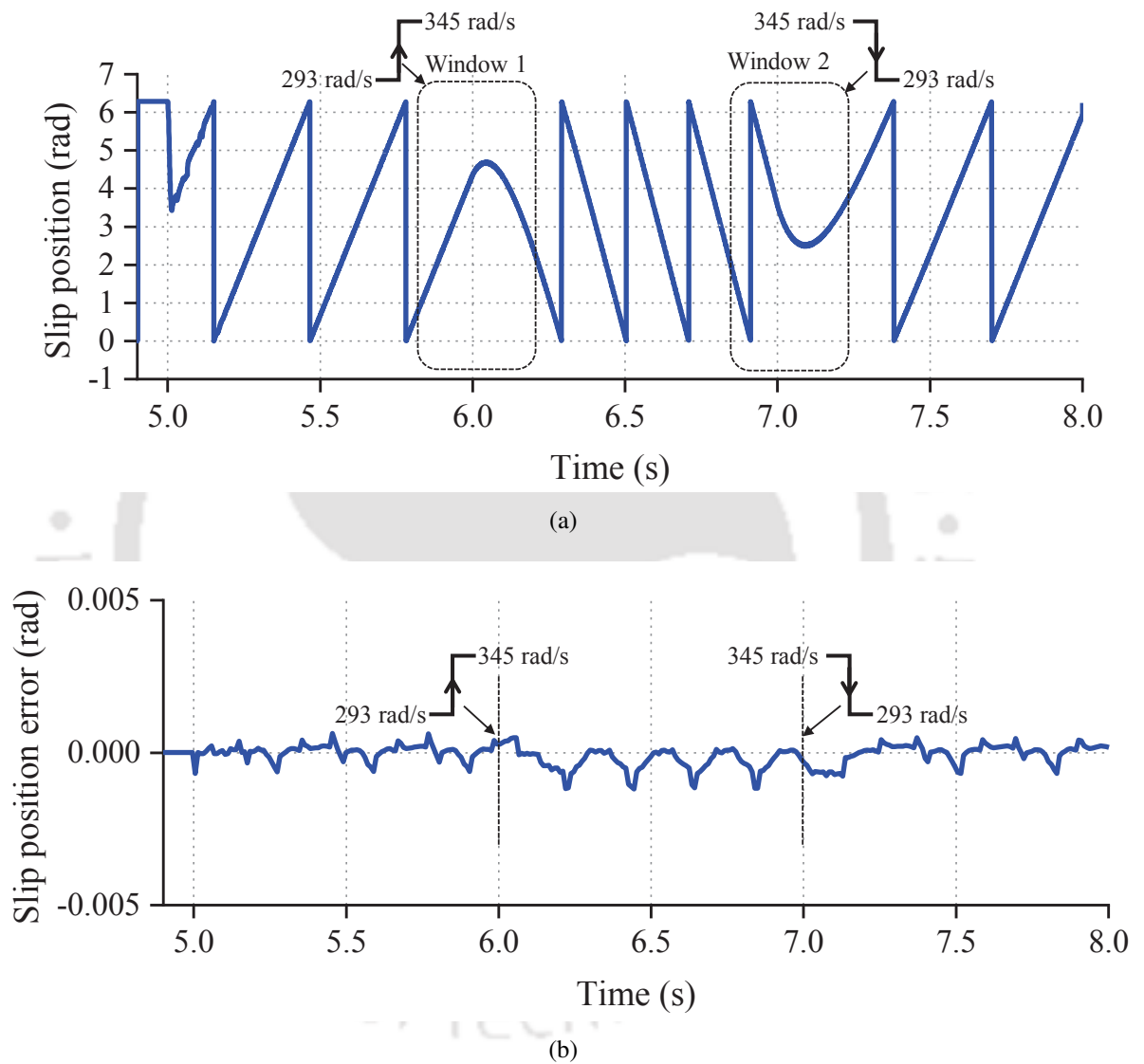
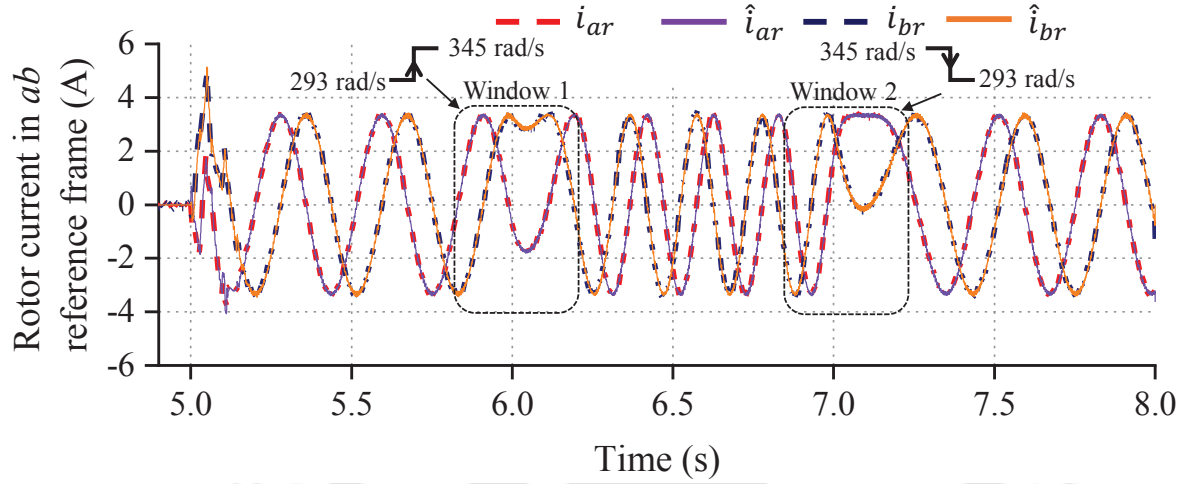
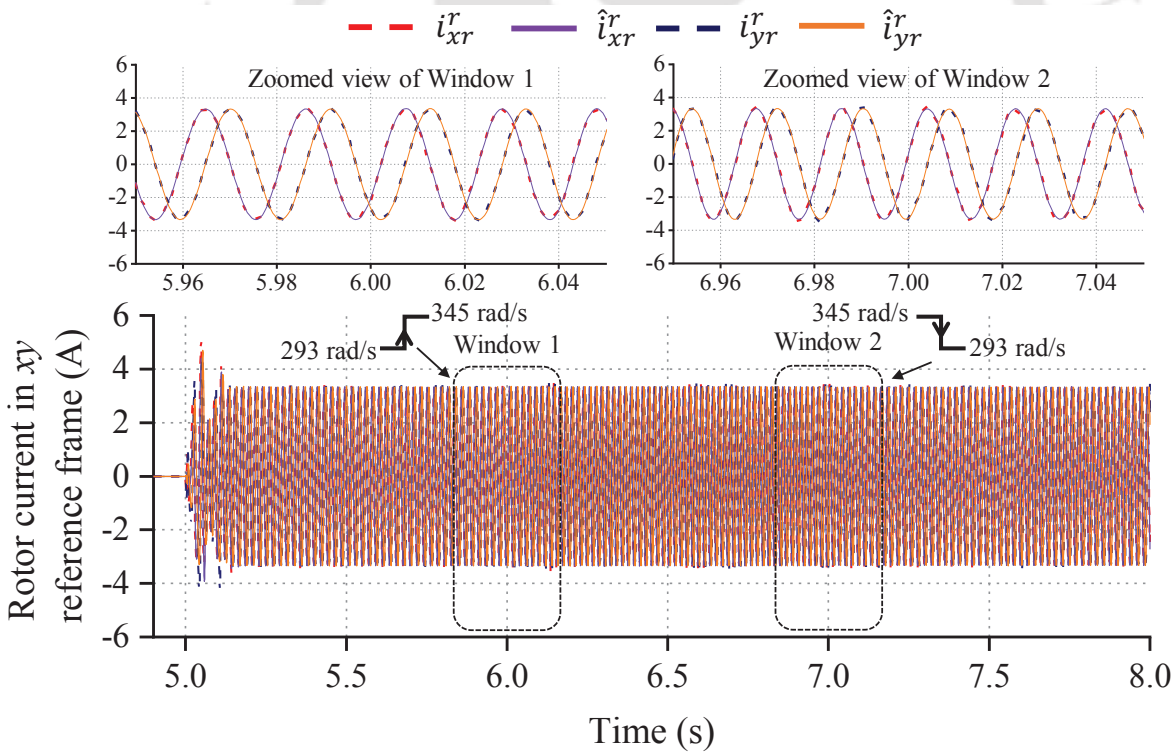


Figure 3.6: Plot during step change in reference input speed (a) estimated slip position of the DFIG (b) the corresponding error plot in the estimated slip position.

3. Robust Slip Angle Speed Estimation Technique Using the Measurement of Rotor Current



(a)



(b)

Figure 3.7: Plot during step change in reference input speed (a) estimated rotor current in ab reference frame, (b) estimated rotor current in xy reference frame.

i_{br} respectively, which ensures the correct estimation of the slip position. Note that i_{ar} leads i_{br} in the super-synchronous mode, but relation reverses in the sub-synchronous mode. This is observed as the direction of slip speed changes from sub-synchronous to super-synchronous zone or vice-versa.

Further, the comparison of the measured rotor current and the estimated rotor current in xy reference frame, which is rotating at slip speed is shown in Figure 3.7(b). Figure 3.7(b) shows the estimated \hat{i}_{xr}^r and \hat{i}_{yr}^r , converging to i_{xr}^r and i_{yr}^r , respectively. This demonstrates the effectiveness of the proposed estimator in estimating the rotor slip position.

From the above simulation, it can be observed that the performance of the proposed estimator is satisfactory during the transition of the speed of DFIG from sub-synchronous to super-synchronous and vice-versa. Also, the performance of the estimator is satisfactory near the synchronous speed.

3.5.2 Case 2: Step Changes in the Load Connected at the Stator Terminal

In this case, per phase resistive load with three load setting of 250 Ω , 50 Ω , 150 Ω is connected at the stator terminal of the machine. Initially, a load of 250 Ω is connected, and at $t = 8$ s, the resistive load is switched to 50 Ω . Then, at $t = 9$ s, the resistive load is switched to 150 Ω . The profile of the connected resistive load is shown in Figure 3.8.

Figure 3.9(a)(a) shows the plot of reference rotor speed (ω_{ref}), actual rotor speed (ω_r), and estimated rotor speed ($\hat{\omega}_r$). From Figure, 3.9(a)(a), a small overshoot and undershoot are noticed in the estimated speed. The corresponding error plot is shown in Figure 3.9(a)(b). It is observed that the speed variation higher at time $t = 8$ s. This is due to the load change being more drastic at observation seems to be obvious as more change in step load occurs at time $t = 8$ s.

Figure 3.10(a) shows the estimated rotor slip angle ($\hat{\theta}_{sl}$). The corresponding error is plotted in Figure 3.10(b). From Figure 3.10(a), it is observed that a sudden phase jump accompanies a step change in load (at both $t = 8$ s and $t = 9$ s. Figure 3.10(b) shows that the deviation in the rotor slip position is less than 0.001 rad. Hence, it can be said that the performance of the proposed slip position estimator is satisfactory.

The estimated and actual rotor current components in ab and xy reference frame are shown in Figures 3.11(a) and 3.11(b), respectively. It is observed from Figure 3.11(a) and 3.11(b) that the sudden load variation (80%) brings about an abrupt change in i_{ar} and i_{br} , and i_{xr}^r and i_{yr}^r .

3. Robust Slip Angle Speed Estimation Technique Using the Measurement of Rotor Current

The settling time of the i_{ar} and i_{br} is almost 0.08 s. The estimated \hat{i}_{ar} and \hat{i}_{br} also converges within 0.08 s. Similarly, the estimated \hat{i}_{xr}^r and \hat{i}_{yr}^r also converges within 0.08 s. At time $t = 9$ s, the load resistance increases from 50Ω to 150Ω . The settling time of actual and estimated rotor current components is less than 0.02 s. This fast setting time of estimated rotor currents ensures the accurate estimation of $\hat{\theta}_{sl}$ and rotor speed $\hat{\omega}_r$.

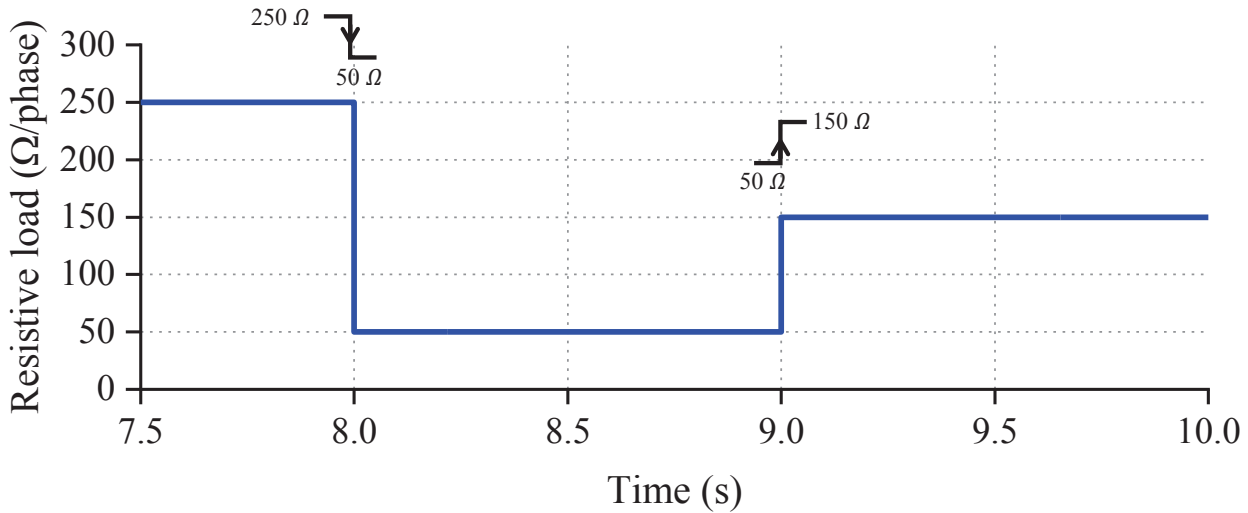


Figure 3.8: Per phase resistive load variation connected to the stator terminals.

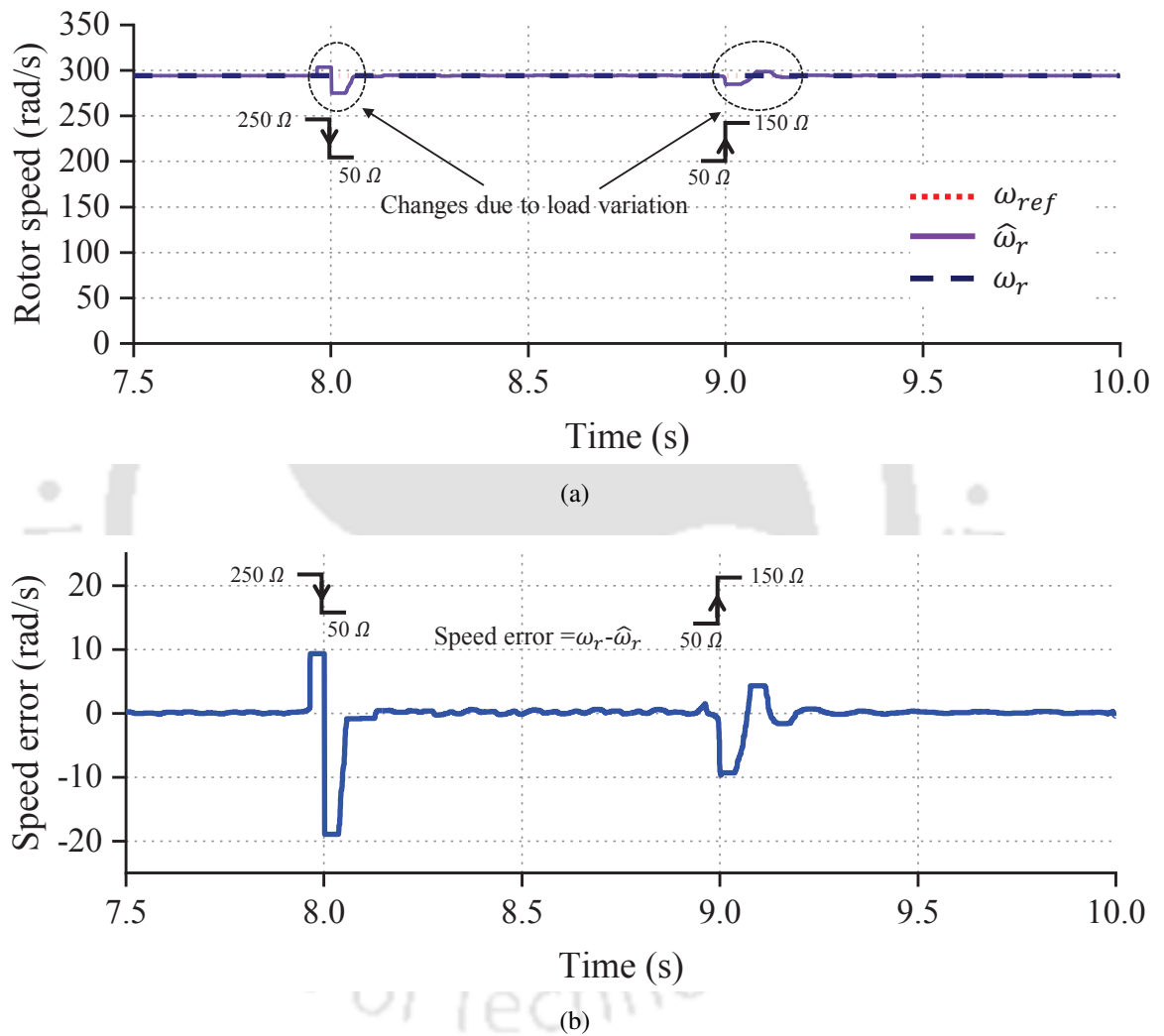


Figure 3.9: During load variation, (a) estimated and actual speed, and (b) speed error.

3. Robust Slip Angle Speed Estimation Technique Using the Measurement of Rotor Current

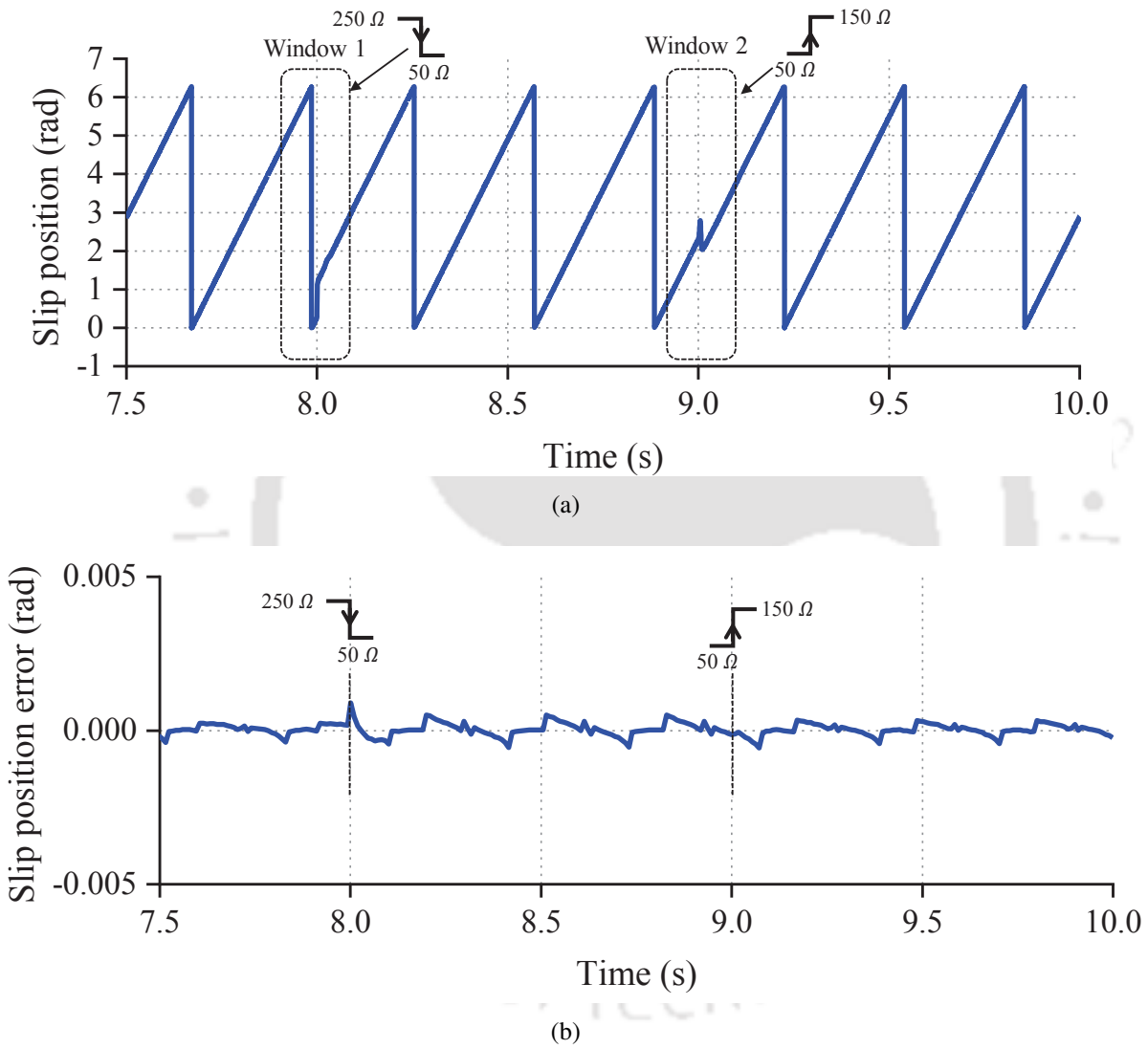
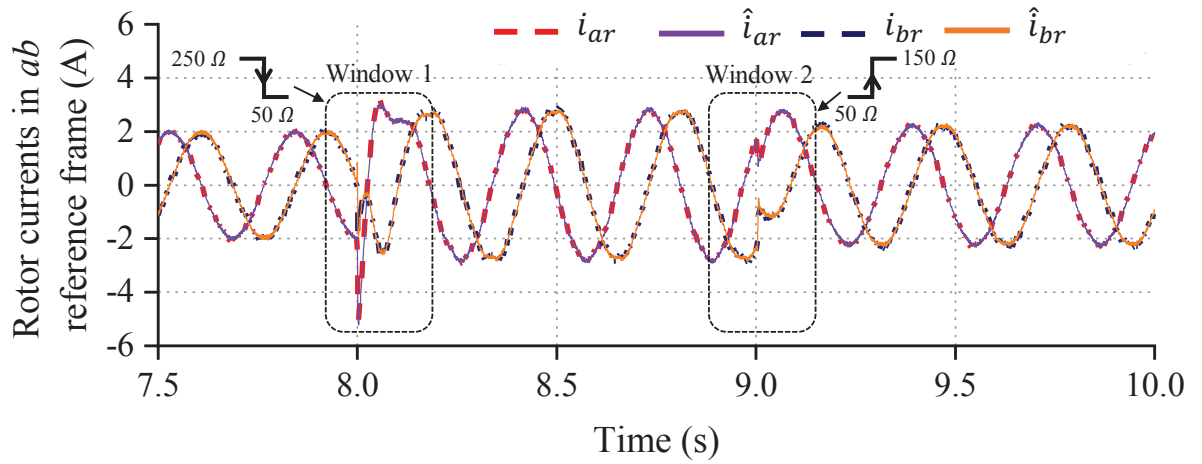
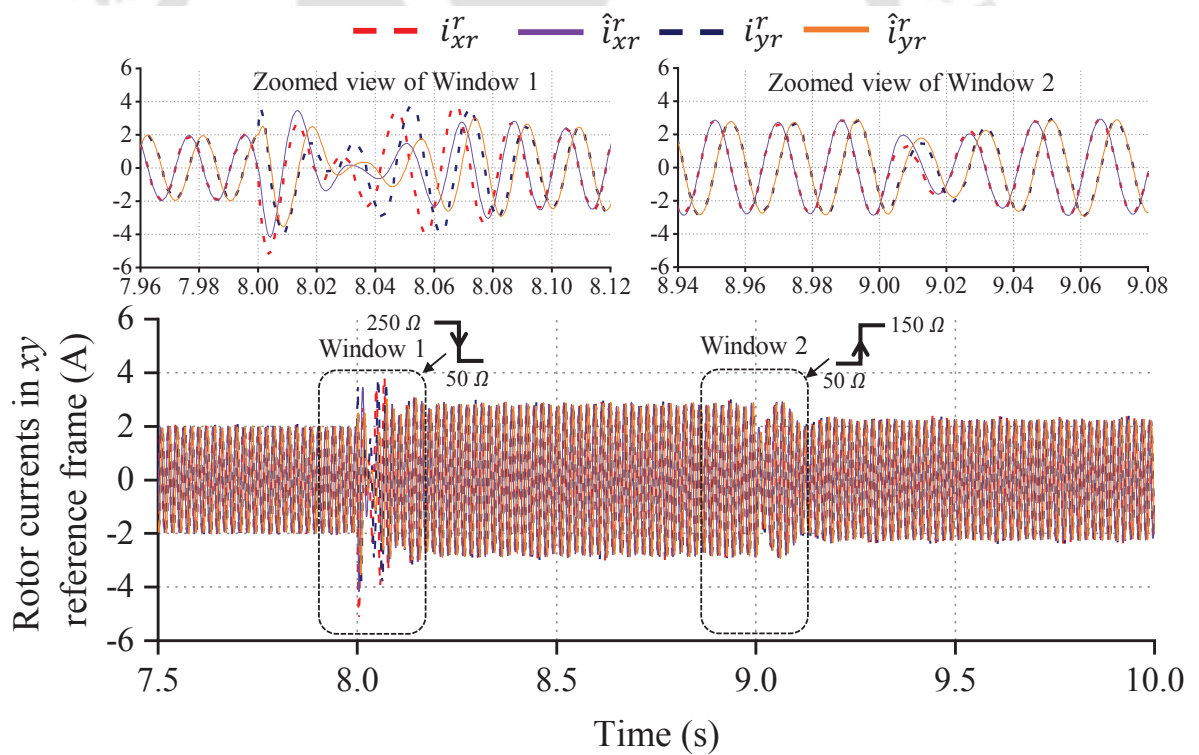


Figure 3.10: During load variation, (a) estimated slip position and (b) slip position error.



(a)



(b)

Figure 3.11: During load variation, (a) estimated and actual rotor current components in ab reference, (b) estimated and actual rotor current components in xy reference.

3.5.3 Case 3: Mutual Inductance Variation

Typically, it is difficult to get an exact estimate of the mutual inductance, L_m of a DFIG. Hence, there can be error in the value of L_m used while designing the slip position estimator. The present simulation analyzes the effect of variations of L_m on the estimated slip position and rotor speed. To perform the simulation, the L_m is reduced by 30% of its nominal value.

The estimation of $\hat{\theta}_r$ and corresponding speed error are shown in Figure 3.12(a) and 3.12(b), respectively. From Figure 3.12(b), it is clear that the speed estimation error is not effected by the 30% change of L_m .

The estimated slip position and corresponding error are shown in Figure 3.13(a) and 3.13(b), respectively. In Figure 3.13(b), it is seen that the magnitude of phase error is small (less than ± 0.0005 rad). Therefore, the effect of the L_m variation is negligible in slip position estimation.

It is observed from Figure 3.14(a) that there is a magnitude deviation in rotor current components i_{ar} and i_{br} . The rotor current components in the xy frame are given in Figure 3.14(b).

All the simulation results shows that the proposed estimator is robust to speed variation, load changes and L_m variation. Thus the proposed estimator fulfill two major requirements: a) ability to accurately track slip position and speed on the fly, and b) stability near the synchronous speed.

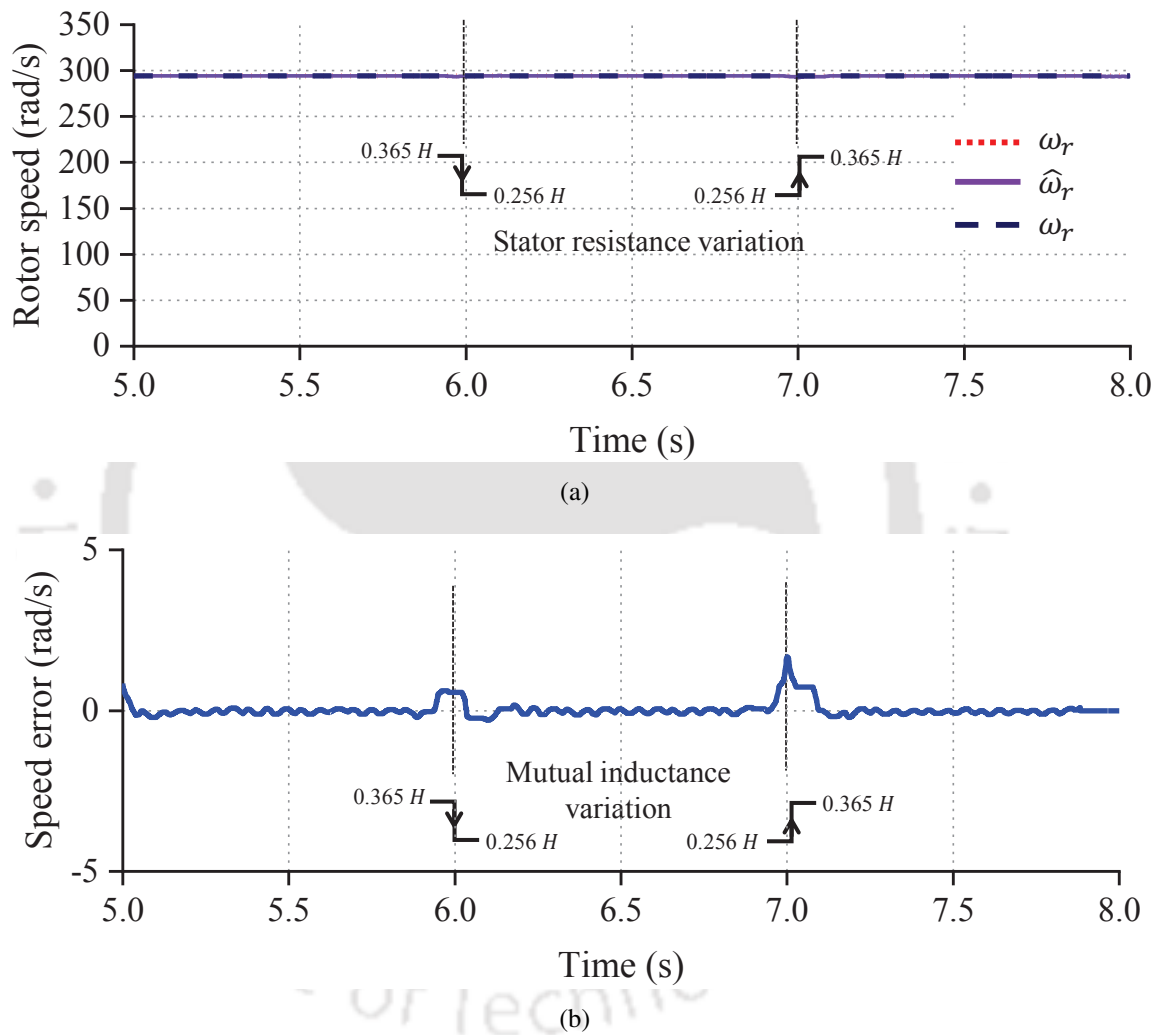


Figure 3.12: During L_m variation, (a) estimated speed and (b) speed error

3. Robust Slip Angle Speed Estimation Technique Using the Measurement of Rotor Current

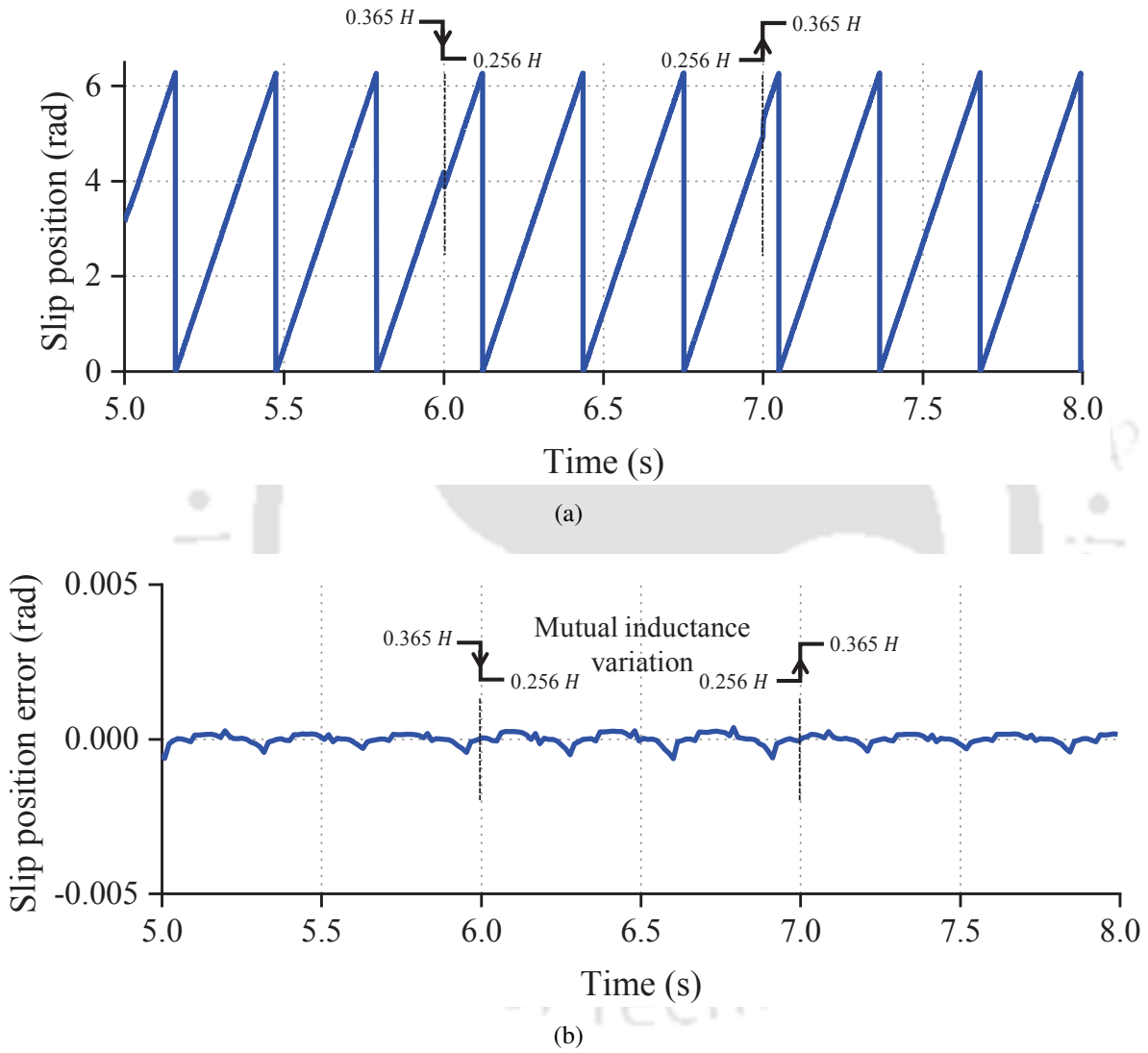


Figure 3.13: During L_m variation, (a) estimated slip position and (b) slip position error.

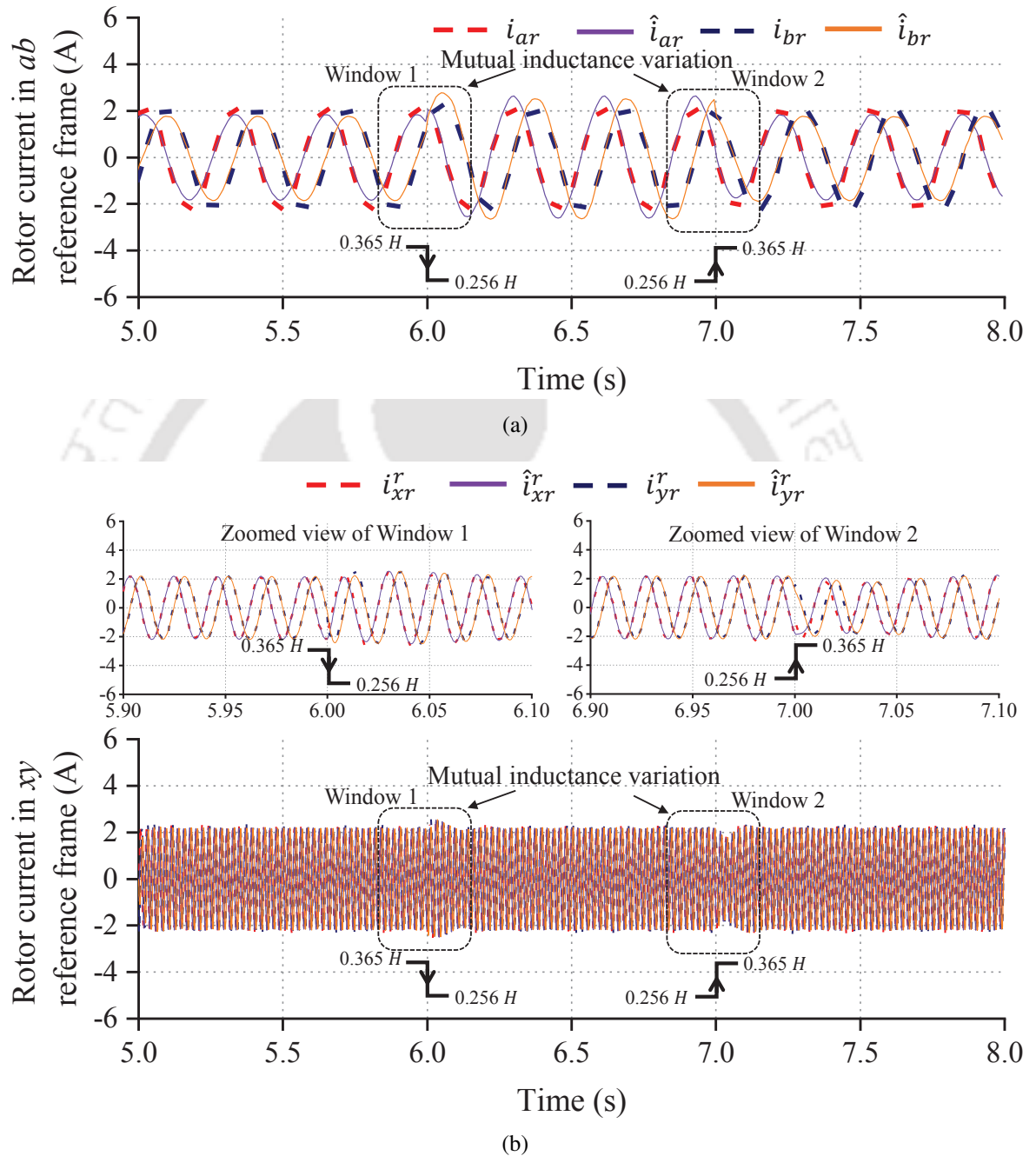


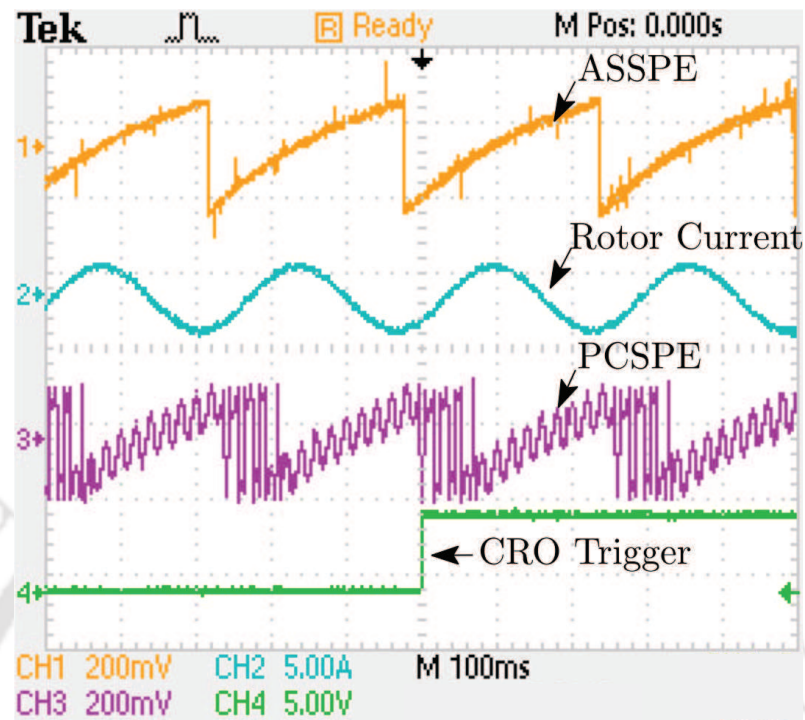
Figure 3.14: During L_m variation, (a) estimated and actual rotor current components in ab reference frame and (b) estimated and actual rotor current components in xy reference frame.

3.6 Experimental Results

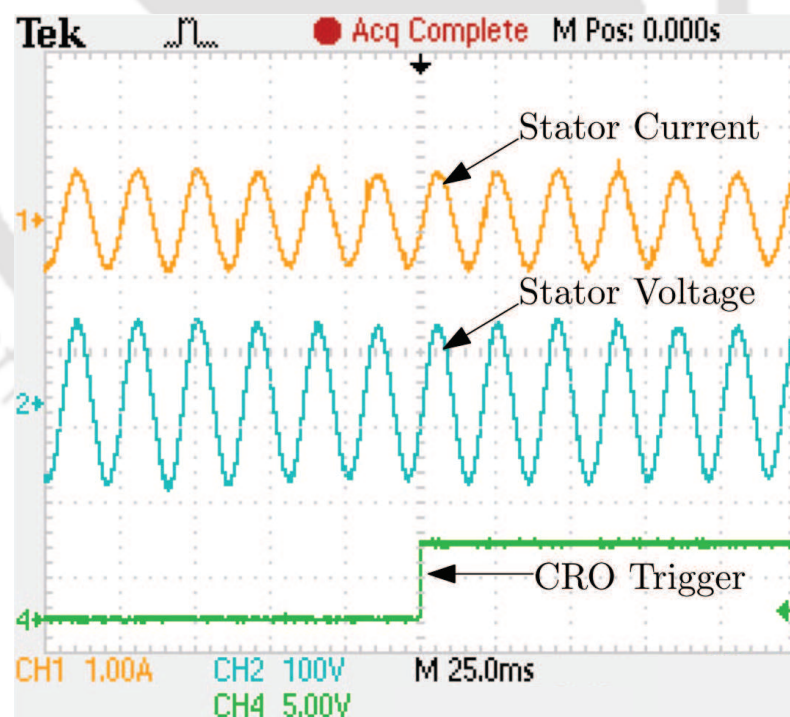
The performance of the estimator has been tested under operation of the DFIG in following conditions: 1) sub-synchronous speed of 1384 rpm, 2) transition from super-synchronous speed of 1535 rpm to sub-synchronous speed of 1490 rpm and back to super-synchronous speed, and 3) a sudden change of load connected at the stator terminal of the DFIG from 300 Ω to 150 Ω (per-phase values). The starting procedure of the experimental setup for algorithm testing is explained in Appendix A.

3.6.1 Case 1: Sub-synchronous Operation Response

Sub-synchronous operation of DFIG at 1380 rpm constant rotor speed is shown in Figure 3.15(a). The performance of the proposed observer i.e., adaptive speed and slip position estimator (ASSPE) is compared with the stator flux based observer discussed in chapter 2 i.e., a predictor corrector based slip position estimator (PCSPE). It can be observed from Figure 3.15(a) that the estimated slip position obtained by ASSPE, is more accurate than that obtained by the PCSPE observer. Moreover, the estimated slip position by PCSPE has large oscillation. The corresponding stator voltage and stator current is captured in Figure 3.15(b). The slip position estimation error of ASSPE and PCSPE are plotted in Figure 3.16. It is observed from Figure 3.16 that the error for PCSPE (represented in dotted line) has more oscillation in comparison to the error in ASSPE (represented in solid line). The peak to peak error magnitudes are 0.047 rad and 0.057 rad for ASSPE and PCSPE, respectively.



(a)



(b)

Figure 3.15: Experiment results of ASSPE and stator flux based PCSPE when DFIG is operating with speed 1384 rpm. (a) Comparison between ASSPE and PCSPE (b) Corresponding stator voltage and current.

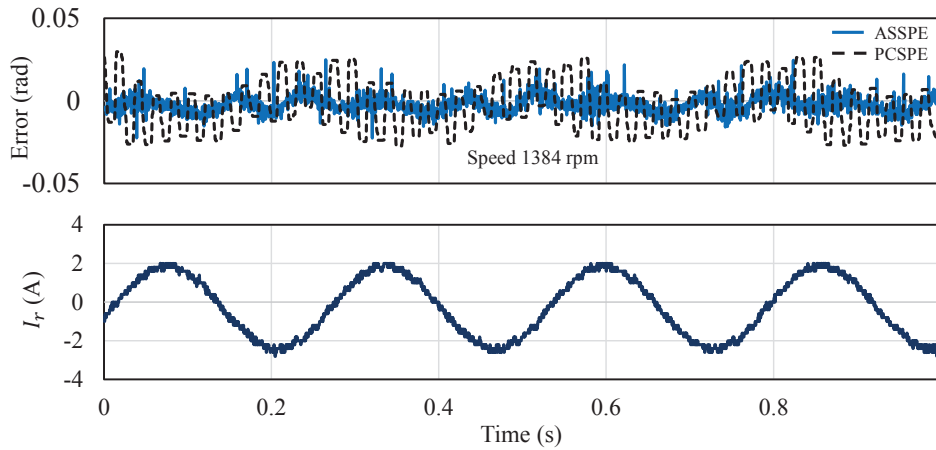
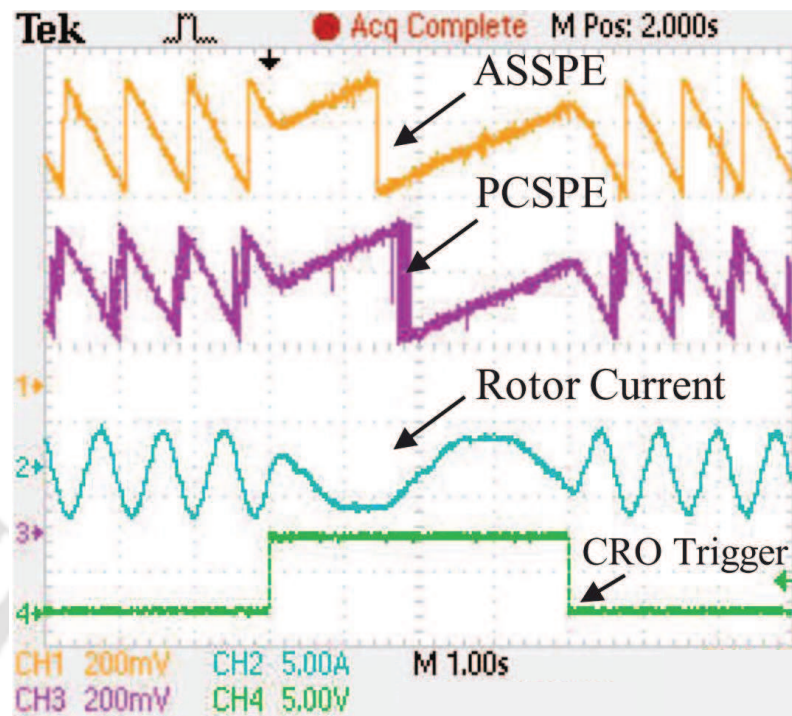


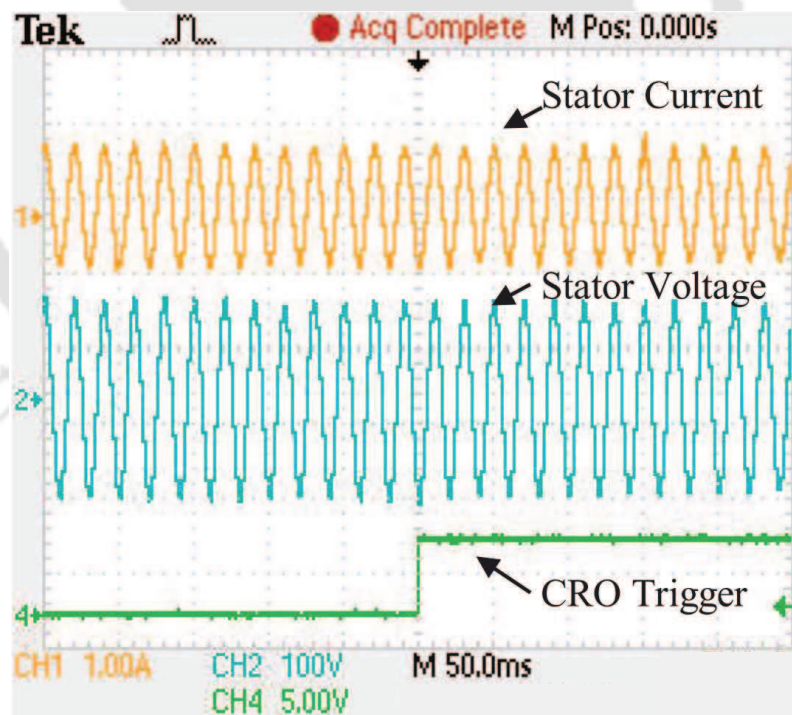
Figure 3.16: The slip position error at constant speed operation at 1384 rpm

3.6.2 Case 2: Speed Change Operation Response

The performance of the proposed ASSPE at super-synchronous speed of 1535 rpm is shown in Figure 3.17(a). The performance is compared with that of the flux based observer at a low operating slip of 0.023. It is observed in Figure 3.17(a) that the slip position estimation is more accurate than that of the flux based observer when the machine operates close to synchronous speed. Figure 3.17(b) shows the corresponding stator voltage and current. At $t = 3.2$ s, the speed reference is changed from 1535 rpm (super-synchronous speed) to 1490 rpm (sub-synchronous speed), and again at $t = 7.1$ s, the speed command is changed to 1535 rpm from 1490 rpm. The slip position estimation error of ASSPE and PCSPE are plotted in Figure 3.18. It is observed from Figure 3.18, at super-synchronous speed ranges, the peak to peak error magnitudes are 0.028 rad (0 s to 3.2 s) and 0.039 rad (7.1 to 10 s) for ASSPE, respectively. The peak to peak error magnitudes are 0.081 rad (0 s to 3.2 s) and 0.077 rad (7.1 s to 10 s) for PCSPE, respectively. At sub-synchronous speed range (3.2 s to 7.1 s), the peak to peak error magnitudes are 0.018 rad and 0.068 rad for ASSPE and PCSPE, respectively. An oscillation is also observed in the error plot for the PCSPE.



(a)



(b)

Figure 3.17: Experiment results of ASSPE and stator flux based PCSPE during speed change. (a) Comparison between ASSPE and PCSPE at supersynchronous to subsynchronous speed transition and vice-versa, (b) Corresponding Stator voltage and current.

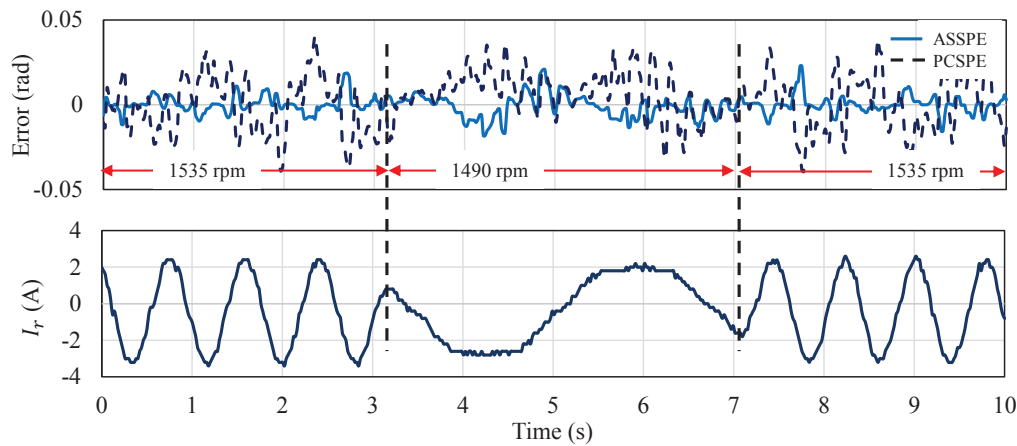
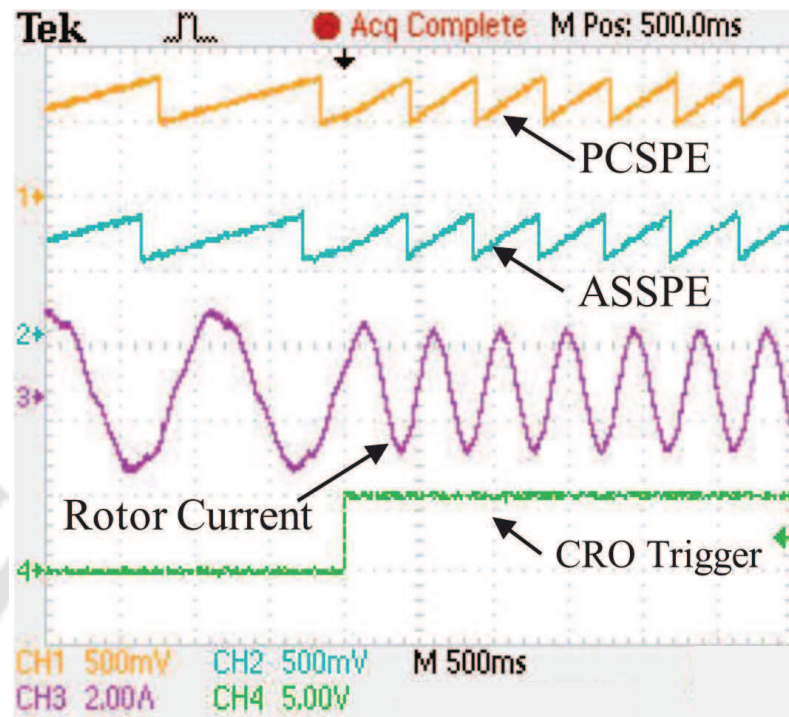


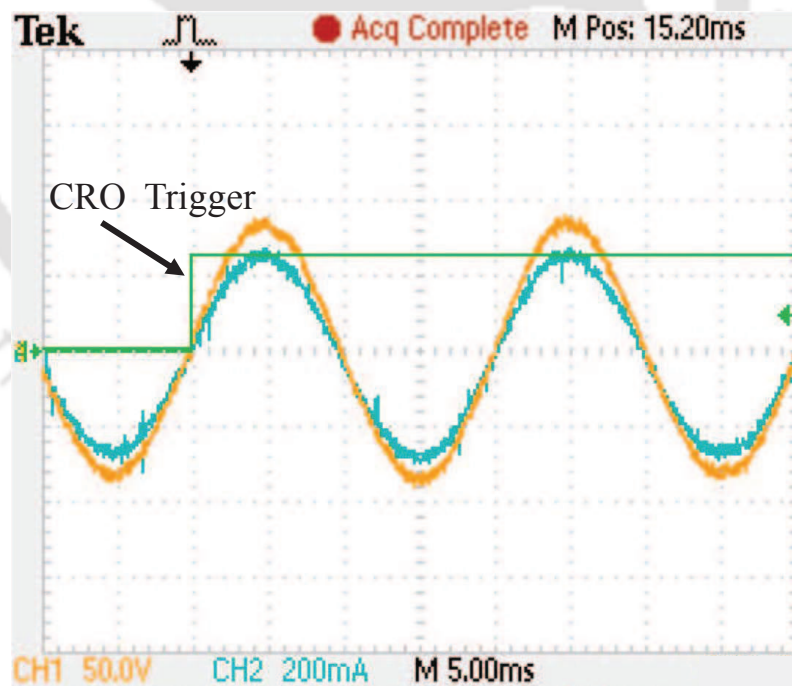
Figure 3.18: The slip position error during speed change from super-synchronous to sub-synchronous speed operation and vice-versa.

3.6.3 Case 3: Load Change Operation Response

A per phase resistive load (300Ω) is connected to the stator terminal of the machine. The resistive load is subjected to a sudden reduction from 300Ω to 150Ω . Figure 3.19(a) shows the comparative performance of the proposed ASSPE and the PCSPE (discussed in the Chapter 2). The generated stator voltage and current is shown in Figure 3.19(b). The frequency of the stator voltage and current is 50 Hz. The corresponding slip position error plot is shown in Figure 3.20. A sudden load change occurred at $t = 2$ s. It can be seen from Figure 3.20 that the peak to peak magnitudes of the slip position errors are 0.024 rad and 0.043 rad for ASSPE and PCSPE, respectively. During sudden load variation, it is observed from the rotor current plot that there is a small speed deviation (40 rpm). This is due to the change in the shaft of the coupled DC motor. The performance of the proposed slip position estimator is found to be robust during load transitions, as given Figure 3.19.



(a)



(b)

Figure 3.19: Experimental results of ASSPE and stator flux based PCSPE during load change. (a) Comparison between flux based observer, (b) Corresponding stator voltage and current.

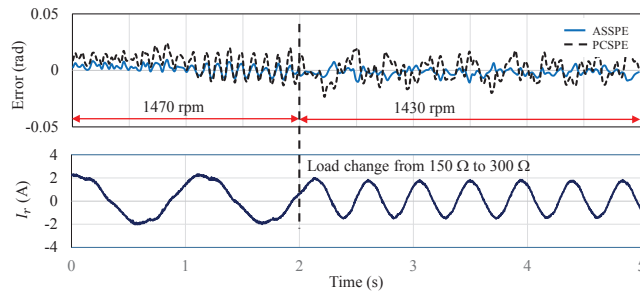


Figure 3.20: The slip position error during load change.

3.7 Conclusion

A new slip angle and rotor speed estimator for a standalone variable speed DFIG system has been presented in this chapter. The proposed estimator requires a fewer number of DFIG parameters as compared to the model-based estimators available in the literature. Further, the estimator takes into account the stator leakage inductance and turn ratio, which improves the estimation accuracy. Moreover, the proposed scheme does not need a stator flux estimation. The working of the proposed estimator has been simulated in PSCAD software under various test conditions. The simulation results were found to be satisfactory. The estimator has also been implemented and validated on a hardware setup of the DFIG system. The performance of the scheme has been compared to that of a flux-based slip position estimator.

4

Robust Slip Angle and Speed Observer for Sensorless Operation of a DFIG: An LMI Approach

Contents

4.1	Introduction	68
4.2	Model and Standalone Operation of DFIG	68
4.3	Proposed Estimation Method	69
4.4	Results and Discussion	79
4.5	Conclusion	90

4.1 Introduction

In this Chapter, we aim to design an observer which is robust to sudden load and speed changes, noise and parametric uncertainty. For achieving the objective, we have designed a two-stage slip position and speed estimator. The corresponding observer gains are calculated by solving Linear Matrix Inequality (LMI). This LMI is solved using the MATLAB LMI toolbox. The working of the proposed observer is simulated in MATLAB Simulink. Further, the observer is validated on a laboratory test bench of the DFIG system.

4.2 Model and Standalone Operation of DFIG

In the synchronous reference frame, the mathematical model of the DFIG is given by the following set of equations:

The stator and rotor voltage components are given by

$$[v_s]^{dq} = R_s[i_s]^{dq} + \frac{d[\psi_s]^{dq}}{dt} + j\omega_s[\psi_s]^{dq} \quad (4.1)$$

$$[v_r]^{dq} = R_r[i_r]^{dq} + \frac{d[\psi_r]^{dq}}{dt} + j(\omega_s - \omega_r)[\psi_r]^{dq} \quad (4.2)$$

The stator and rotor flux components are given by

$$[\psi_s]^{dq} = L_s[i_s]^{dq} + L_m[i_r]^{dq} \quad (4.3)$$

$$[\psi_r]^{dq} = L_r[i_r]^{dq} + L_m[i_s]^{dq} \quad (4.4)$$

The electromagnetic torque is given by

$$T_e = \frac{3p}{2}(\psi_{ds}i_{qs} - \psi_{qs}i_{ds}) \quad (4.5)$$

$$\frac{d\omega_m}{dt} = \frac{1}{J}(T_e - T_t - f_\mu\omega_m) \quad (4.6)$$

where $[v_s]^{dq} = v_{ds} + jv_{qs}$, $[v_r]^{dq} = v_{dr} + jv_{qr}$, $[i_s]^{dq} = i_{ds} + ji_{qs}$ and $[i_r]^{dq} = i_{dr} + ji_{qr}$ are the stator voltage vector, rotor voltage vector, stator current vector and rotor current vector respectively. The stator and rotor flux linkage vectors are denoted by $[\psi_s]^{dq} = \psi_{ds} + j\psi_{qs}$ and $[\psi_r]^{dq} = \psi_{dr} + j\psi_{qr}$ respectively. The rotor electrical speed and stator electrical speed are denoted by ω_r and ω_s , R_s , R_r are the stator and rotor resistances, L_s , L_r are the stator and rotor inductances, L_m is the magnetizing

inductance, T_t is the turbine torque, J and f_μ are the moment of inertia and frictional co-efficient and ω_m is the mechanical rotor speed.

During standalone operation, the control system is designed to achieve desired grid voltage magnitude and constant frequency.

An additional load, Z_L is connected at the generator terminal. The voltage across the load at the stator terminals is given by

$$[v_s]^{dq} = -Z_L[i_s]^{dq} = -(R_L + j\omega_s L_L)[i_s]^{dq} \quad (4.7)$$

where R_L and L_L are the load resistance and load inductance respectively.

At steady state condition, the voltage equation in dq reference frame is given by

$$[v_s]^{dq} = (R_s + j\omega_s L_s)[i_s]^{dq} + j\omega_s L_m [i_r]^{dq}. \quad (4.8)$$

Substituting (4.7) into (4.8), the steady state model of DFIG obtained is given by

$$[v_s]^{dq} = \frac{j\omega_s L_m Z_L [i_r]^{dq}}{R_s + j\omega_s L_s + Z_L}. \quad (4.9)$$

The stator voltage magnitude and angle are independently controlled by regulating the rotor current and angle respectively as obtained in (4.9). From (4.7)-(4.9), it is clear that the stator current $[i_s]^{dq}$ is susceptible to disturbances caused by changes in load.

4.3 Proposed Estimation Method

In order to make slip position and velocity estimation robust to changes in operating point and parametric variations, an H_∞ based observer is proposed. The inputs to the proposed observer are the stator terminal voltages and currents, and the rotor currents. The observer consists of two parts (a) Rotor current observer and (b) Slip speed and position observer. The rotor current observer estimates the rotor current in the $\alpha\beta$ frame using the measured stator voltages and currents. The slip speed and position observer uses this estimated rotor current along with the measured value of rotor current, which is in the rotor reference frame, to estimate the slip speed and position. The cross product of the measured rotor current vector with the estimated rotor current vector transformed to the rotor reference, is used as a measure of the slip estimation error. The complete structure of the proposed scheme

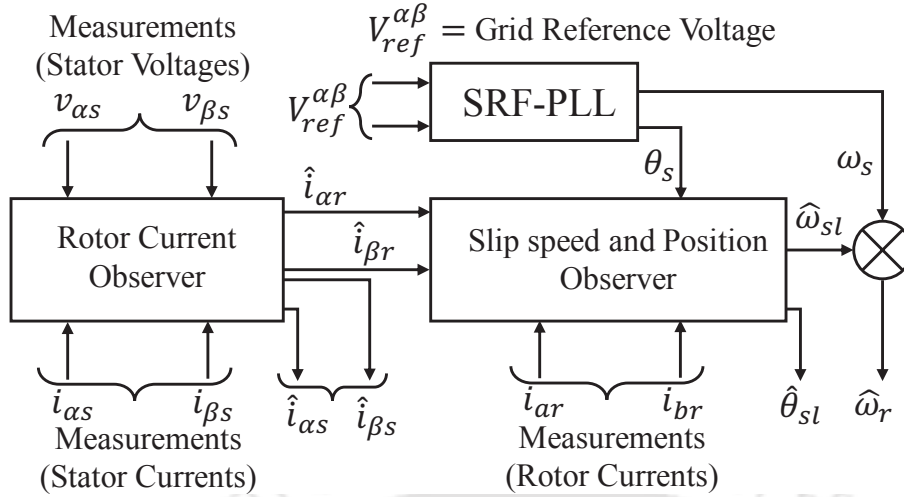


Figure 4.1: Schematic diagram of H_∞ based slip position and slip speed observer for DFIG system.

is shown in Figure 4.1. To test the proposed estimation algorithm, PI based rotor current controller is implemented, as shown in Figure 4.2. This controller regulates the output frequency (at 50 Hz) of the generated stator voltage and current. Discrepancies such as parametric uncertainties, noise and changes in the operating point are modeled by means of a ‘disturbance’ signal. The estimation process is made robust by limiting the H_∞ gain between this ‘disturbance’ and the estimation error. The structure of the proposed robust observer system is given in the Figure 4.3, where the estimated rotor current components are used to estimate the slip position and speed of the DFIG system.

The details of a) rotor current, and b) slip speed and position observers is given in the subsection below.

4.3.1 Rotor Current Observer

The measured rotor current vector is transformed to the stationary ($\alpha\beta$) reference frame using the following equation:

$$[i_r]^{\alpha\beta} = [i_r]^{ab} \exp(-j\theta_r) \quad (4.10)$$

where $[i_r]^{\alpha\beta} = i_{\alpha r} + ji_{\beta r}$ and $[i_r]^{ab} = i_{ar} + ji_{br}$. Taking derivative on both sides of (4.10), we get

$$\frac{di_{\alpha r}}{dt} = -\omega_s i_{\beta r} \quad (4.11)$$

$$\frac{di_{\beta r}}{dt} = \omega_s i_{\alpha r} \quad (4.12)$$

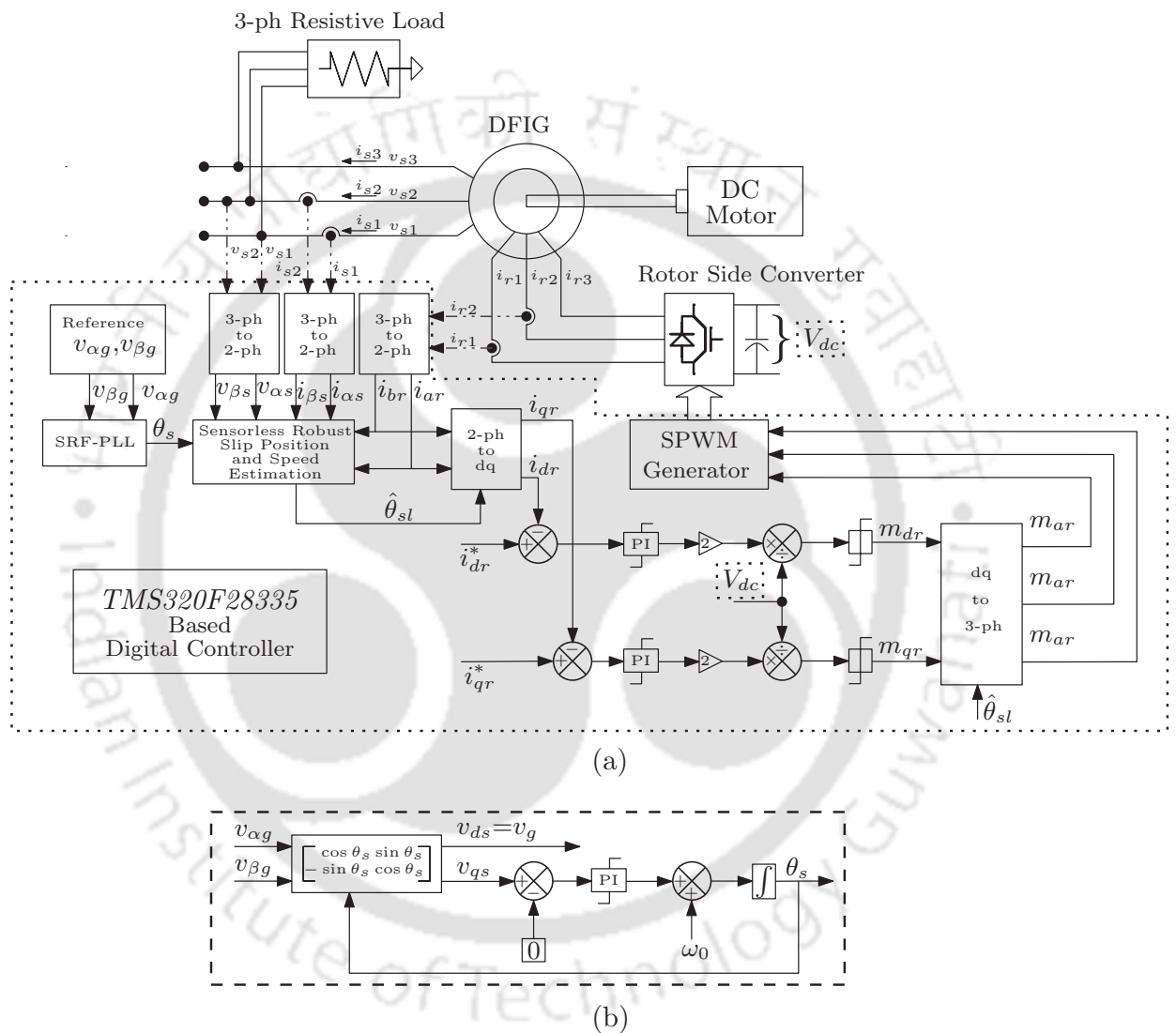


Figure 4.2: (a) Structure of the observer with closed loop control of rotor side converter DFIG . (b) Structure of the SRFPLL system.

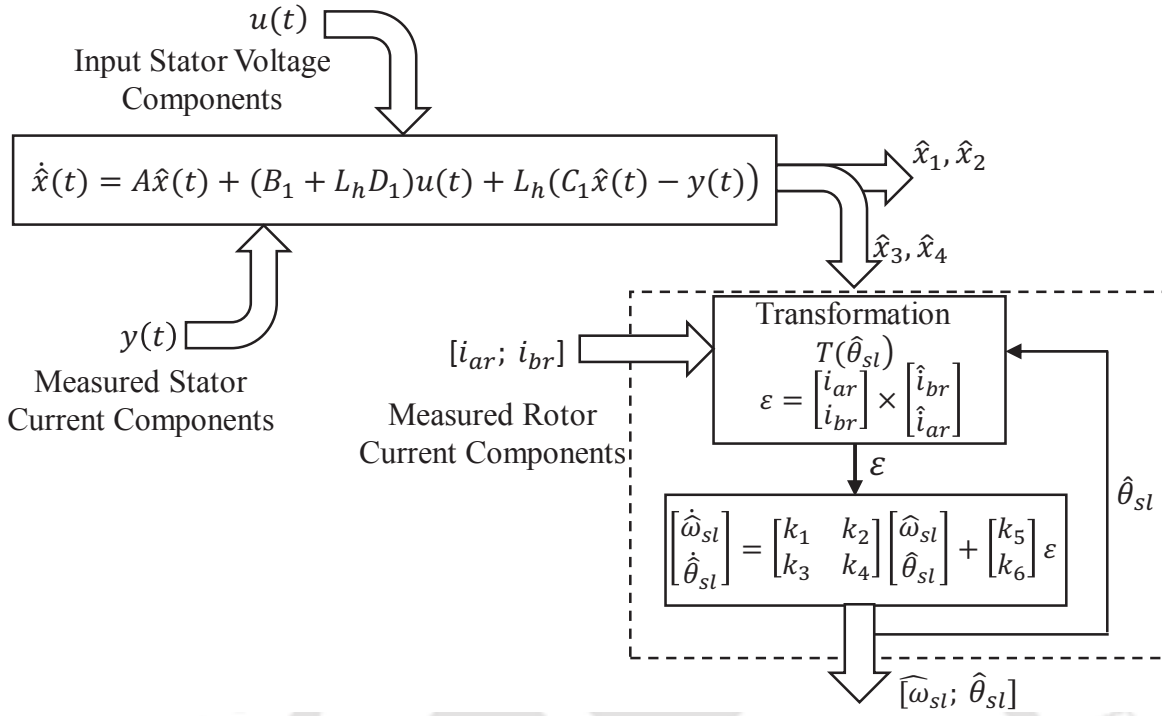


Figure 4.3: The proposed structure of the observer for the estimation of slip position and slip speed.

The stator flux in the stationary reference frame is given by

$$[\psi_s]^{\alpha\beta} = L_s [i_s]^{\alpha\beta} + L_m [i_r]^{\alpha\beta} \quad (4.13)$$

Now, the stator voltage vector in the stationary reference frame is given by

$$[v_s]^{\alpha\beta} = R_s [i_s]^{\alpha\beta} + \frac{d[\psi_s]^{\alpha\beta}}{dt} \quad (4.14)$$

where $[i_s]^{\alpha\beta} = i_{\alpha s} + j i_{\beta s}$, $[i_s]^{ab} = i_{as} + j i_{bs}$, $[v_s]^{\alpha\beta} = v_{\alpha s} + j v_{\beta s}$ and $[\psi_s]^{\alpha\beta} = \psi_{\alpha r} + j \psi_{\beta r}$.

From (4.11), (4.12), (B.27) and (4.14), we get the following

$$\frac{di_{\alpha s}}{dt} = \frac{1}{L_s} (v_{\alpha s} - R_s i_{\alpha s} + L_m \omega_s i_{\beta r}) \quad (4.15)$$

$$\frac{di_{\beta s}}{dt} = \frac{1}{L_s} (v_{\beta s} - R_s i_{\beta s} - L_m \omega_s i_{\alpha r}) \quad (4.16)$$

Equations (4.11), (4.12), (4.15) and (4.16) give rise to the following state space representation:

$$\frac{d}{dt} \begin{bmatrix} i_{\alpha s} \\ i_{\beta s} \\ i_{\alpha r} \\ i_{\beta r} \end{bmatrix} = A_s \begin{bmatrix} i_{\alpha s} \\ i_{\beta s} \\ i_{\alpha r} \\ i_{\beta r} \end{bmatrix} + B_s \begin{bmatrix} v_{\alpha s} \\ v_{\beta s} \end{bmatrix}$$

and,

$$y(t) = \begin{bmatrix} i_{\alpha s} \\ i_{\beta s} \end{bmatrix} = C_1 \begin{bmatrix} i_{\alpha s} \\ i_{\beta s} \\ i_{\alpha r} \\ i_{\beta r} \end{bmatrix} \quad (4.17)$$

where

$$A_s = \begin{bmatrix} -\frac{R_s}{L_s} & 0 & 0 & \frac{L_m \omega_s}{L_s} \\ 0 & -\frac{R_s}{L_s} & -\frac{L_m \omega_s}{L_s} & 0 \\ 0 & 0 & 0 & -\omega_s \\ 0 & 0 & \omega_s & 0 \end{bmatrix}$$

$$B_s = \begin{bmatrix} \frac{1}{L_s} & 0 \\ 0 & \frac{1}{L_s} \\ 0 & 0 \\ 0 & 0 \end{bmatrix}$$

$$C_1 = \begin{bmatrix} 1 & 0 & 0 & 0 \\ 0 & 1 & 0 & 0 \end{bmatrix}.$$

Clearly, any change in system parameters will effect the matrices A and B_1 . In order to account for these variations, we consider A_s and B_s to be equal to $(A + \Delta A)$ and $(B_1 + \Delta B_1)$, respectively. Here, A and B_1 are the mean values of A_s and B_s while ΔA and ΔB_1 represent the corresponding deviations.

Thus equation (4.17) can be written as

$$\left. \begin{aligned} \dot{x}(t) &= (A + \Delta A)x(t) + (B_1 + \Delta B_1)u(t) \\ &= Ax(t) + B_1u(t) + (\Delta Ax(t) + \Delta B_1u(t)) \\ y(t) &= C_1x(t) \end{aligned} \right\} \quad (4.18)$$

where $x(t) = \begin{bmatrix} i_{\alpha s} \\ i_{\beta s} \\ i_{\alpha r} \\ i_{\beta r} \end{bmatrix} \in \mathbb{R}^4$ and $y(t) \in \mathbb{R}^2$ are the state vector and the measured output vector respectively.

We add a signal $w_1(t)$ ($w_1(t) \in \mathbb{R}^4$) in the state transition equation to account for $\Delta Ax + \Delta B_1u$ and any other disturbance. Further, in order to account for the measurement noise, we introduce a signal $w_2(t)$ ($w_2(t) \in \mathbb{R}^2$). The modified state space equations are as follows

$$\left. \begin{aligned} \dot{x}(t) &= Ax(t) + B_1u(t) + w_1(t) \\ y(t) &= C_1x(t) + w_2(t) \end{aligned} \right\} \quad (4.19)$$

Equation (4.19) can be rewritten in terms of $w(t)$ as follows:

$$\left. \begin{aligned} \dot{x}(t) &= Ax(t) + B_1u(t) + B_2w(t) \\ y(t) &= C_1x(t) + Dw(t) \end{aligned} \right\} \quad (4.20)$$

where $B_2 = \begin{bmatrix} I & 0 \end{bmatrix} \in \mathbb{R}^{4 \times 6}$ and $D = \begin{bmatrix} 0 & I \end{bmatrix} \in \mathbb{R}^{2 \times 6}$, and $w(t) = \begin{bmatrix} w_1(t) \\ w_2(t) \end{bmatrix} \in \mathbb{R}^6$.

In order to estimate the states of the system described by (4.20), we employ an observer having the following dynamic equation

$$\dot{\hat{x}}(t) = A\hat{x}(t) + B_1u(t) + L_h(C_1\hat{x}(t) - y) \quad (4.21)$$

where $\hat{x}(t) \in \mathbb{R}^4$ is the estimated state vector and $L_h \in \mathbb{R}^{4 \times 2}$ is the observer gain. The dynamics of the state estimation error $e(t) = x(t) - \hat{x}(t)$ given by the following state space equations

$$\left. \begin{aligned} \dot{e}(t) &= (A + L_hC_1)e(t) + (B_2 + L_hD)w(t) \\ \tilde{z}(t) &= e. \end{aligned} \right\} \quad (4.22)$$

Therefore, the transfer function matrix between the error vector $e(t)$ and the disturbance vector $w(t)$ is given by

$$G_{\bar{z}w}(S) = (SI - A - L_h C_1)^{-1}(B_2 + L_h D).$$

The impact of $w(t)$ on the error dynamics can be limited by limiting the H_∞ gain of $G_{\bar{z}w}(S)$ below a predefined attenuation level γ_1 . The H_∞ gain of $G_{\bar{z}w}(S)$ is a measure of the impact of $w(t)$ on the error dynamics. Thus, by limiting this gain below a predefined attenuation level γ_1 , the observer can be made robust to disturbances.

Thus, the problem of observer design reduces to finding a gain matrix L_h such that

$$\|G_{\bar{z}w}(S)\|_\infty < \gamma_1. \quad (4.23)$$

One can find such an L_h satisfying the above inequality if and only if there exist a matrix $W \in \mathbb{R}^{2 \times 4}$ and a symmetric positive definite matrix $P \in \mathbb{R}^{4 \times 4}$ such that

$$\begin{bmatrix} A^T P + C_1^T W^T + PA + WC_1 & PB_2 + WD & I \\ B_2^T P^T + D^T W^T & -\gamma_1 I & 0 \\ I & 0 & -\gamma_1 I \end{bmatrix} < 0 \quad (4.24)$$

Further, if a pair of matrices W and P satisfy the above linear matrix inequality [61], the gain matrix $L_h = WP^{-1}$ satisfies Inequality (4.23).

4.3.2 Slip Position and Slip Speed Observer

This observer uses the rotor current estimates generated in the rotor current observer along with the measured rotor current values to estimate the slip position and slip speed of the system.

As we have seen in the previous subsection, the rotor current observer estimates the rotor current components in the stationary reference frame viz. $\hat{i}_{\alpha r}$ and $\hat{i}_{\beta r}$. Let $\hat{\theta}_{sl}$ be the estimated slip angle. Using $\hat{\theta}_{sl}$, the estimated rotor current is transformed to the rotor reference frame as follows:

$$\begin{bmatrix} \hat{i}_{ar} \\ \hat{i}_{br} \end{bmatrix} = \begin{bmatrix} \cos(\theta_s - \hat{\theta}_{sl}) & -\sin(\theta_s - \hat{\theta}_{sl}) \\ \sin(\theta_s - \hat{\theta}_{sl}) & \cos(\theta_s - \hat{\theta}_{sl}) \end{bmatrix} \begin{bmatrix} \hat{i}_{\alpha r} \\ \hat{i}_{\beta r} \end{bmatrix}$$

where θ_s is the angle of the stator voltage vector which is estimated using a synchronous reference

frame PLL (SRF PLL) as shown in Figure 4.2.

The cross product of the estimated and measured rotor current values is given as

$$\varepsilon = i_{ar}\hat{i}_{br} - i_{br}\hat{i}_{ar} \quad (4.25)$$

$$= |\hat{i}_r||i_r| \sin(\theta_{sl} - \hat{\theta}_{sl}) \quad (4.26)$$

where θ_{sl} is the actual slip position. When the magnitudes of estimated and actual rotor currents are constant the value of ε is approximately proportional to the slip position estimation error (For low values of error magnitude). Moreover, ε goes to zero when the slip position estimation error is zero. ε is therefore used as a measure of slip position estimation error.

In order to model slip dynamics, we assume the rate of change of velocity is equal to a disturbance signal d_n . Under this assumption, the slip dynamics are given as follows

$$\dot{\omega}_{sl} = d_n \quad (4.27)$$

$$\dot{\theta}_{sl} = \omega_{sl}. \quad (4.28)$$

The proposed slip speed and position observer dynamics are as follows

$$\begin{bmatrix} \dot{\hat{\omega}}_{sl} \\ \dot{\hat{\theta}}_{sl} \end{bmatrix} = \begin{bmatrix} k_1 & k_2 \\ k_3 & k_4 \end{bmatrix} \begin{bmatrix} \hat{\omega}_{sl} \\ \hat{\theta}_{sl} \end{bmatrix} + \begin{bmatrix} k_5 \\ k_6 \end{bmatrix} \varepsilon \quad (4.29)$$

where $\hat{\theta}_{sl}$ and $\hat{\omega}_{sl}$ are the estimated values of slip angle and velocity respectively. Note that ε depends on the measured current. Therefore, any sudden change in this measurement (either due to noise or change in operating conditions) will be reflected in ε . Therefore, we limit the H_∞ gain between ε and the estimated speed and position. While doing this we need to ensure that no instability is introduced in the system. Let the error in slip position estimation be denoted by $\tilde{\theta}_{sl} = \theta_{sl} - \hat{\theta}_{sl}$. For small values of $\tilde{\theta}_{sl}$, $\varepsilon \approx |\hat{i}_r||i_r|\tilde{\theta}_{sl}$. Therefore, equation (4.29) can be rewritten as follows

$$\begin{bmatrix} \dot{\hat{\omega}}_{sl} \\ \dot{\hat{\theta}}_{sl} \end{bmatrix} = \begin{bmatrix} k_1 & k_2 \\ k_3 & k_4 \end{bmatrix} \begin{bmatrix} \hat{\omega}_{sl} \\ \hat{\theta}_{sl} \end{bmatrix} + \begin{bmatrix} k_5|\hat{i}_r||i_r| \\ k_6|\hat{i}_r||i_r| \end{bmatrix} \tilde{\theta}_{sl}. \quad (4.30)$$

Equation (4.30) can be represented by the block diagram given in Figure 4.4.

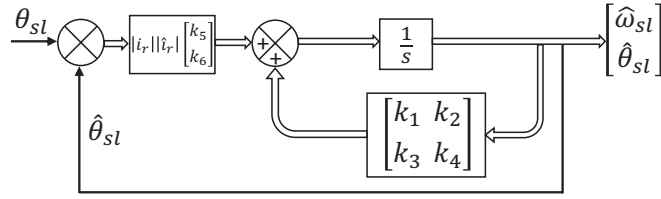


Figure 4.4: Block Diagram of the Proposed Observer

The constants in (4.29) must be chosen such that

- (i) The observer is robust to changes in i_r .
- (ii) The observer system shown in Figure 4.4 is stable.
- (iii) The slip position and velocity errors are within acceptable limits.

The effect of variation in rotor current is contained by ensuring that the H_∞ gain between the vector $\begin{bmatrix} k_5|i_r||\hat{i}_r| \\ k_6|i_r||\hat{i}_r| \end{bmatrix} \tilde{\theta}_{sl}$ and the estimated state vector $\begin{bmatrix} \hat{\omega}_{sl} \\ \hat{\theta}_{sl} \end{bmatrix}$ is below a suitable value γ_2 . Stability is guaranteed by choosing constants such that the system shown in Figure 4.4 is passive. From the set of values which satisfy the above mentioned stability and H_∞ gain conditions, the gains in equation (4.30) are tuned to achieve acceptable estimation errors.

In order to find a set of constants which satisfy the H_∞ gain condition mentioned above, we rewrite equation (4.30) as follows

$$\begin{bmatrix} \dot{\hat{\omega}}_{sl} \\ \dot{\hat{\theta}}_{sl} \end{bmatrix} = (F + K_s) \begin{bmatrix} \hat{\omega}_{sl} \\ \hat{\theta}_{sl} \end{bmatrix} + d \quad (4.31)$$

where $F = \begin{bmatrix} 0 & 0 \\ 1 & 0 \end{bmatrix}$, $K_s = \begin{bmatrix} k_1 & k_2 \\ k_3 - 1 & k_4 \end{bmatrix}$ and $d = \begin{bmatrix} k_5|i_r||\hat{i}_r| \\ k_6|i_r||\hat{i}_r| \end{bmatrix} \tilde{\theta}_{sl}$. There exists a matrix K_s such that the

H_∞ gain between d and $\begin{bmatrix} \dot{\hat{\omega}}_{sl} \\ \dot{\hat{\theta}}_{sl} \end{bmatrix}$ is less than γ_2 if and only there are positive definite matrices P_s and W_s which satisfy the following LMI (from Theorem 9.3 in [61])

$$\begin{bmatrix} (FP_s + W_s)^T + FP_s + W_s & I & P_s^T \\ I & -\gamma_2 I & 0 \\ P_s & 0 & -\gamma_2 I \end{bmatrix} < 0, \quad (4.32)$$

4. Robust Slip Angle and Speed Observer for Sensorless Operation of a DFIG: An LMI Approach

Further, if P_s and W_s are solutions to the above LMI, then choosing $K_s = W_s P_s^{-1}$ ensures that the H_∞ gain between d and $\begin{bmatrix} \hat{\omega}_{sl} \\ \hat{\theta}_{sl} \end{bmatrix}$ is less than γ . The choice of K_s determines the values of k_1, k_2, k_3 and k_4 .

Using standard block diagram reduction techniques, Figure 4.4 can be reduced to the block diagram shown in Figure 4.5.

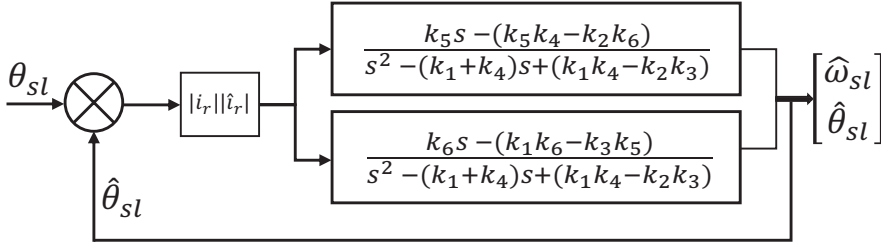


Figure 4.5: Reduced block Diagram of the Proposed Observer

If the maximum possible amplitude of i_r is $|i_r|_{max}$, then $|i_r|/|\hat{i}_r|$ varies from 0 to $|i_r|_{max}^2$. Hence, the block with gain $|i_r|/|\hat{i}_r|$ is passive and takes values in a sector of the first quadrant. The system shown in Figure 4.5 is passive if the following transfer functions are passive

$$G_1(s) = \frac{k_5s - (k_5k_4 - k_2k_6)}{s^2 - (k_1 + k_4)s + (k_1k_4 - k_2k_3)}$$

$$G_2(s) = \frac{1}{|i_r|_{max}^2} + \frac{k_6s - (k_1k_6 - k_3k_5)}{s^2 - (k_1 + k_4)s + (k_1k_4 - k_2k_3)}$$

Therefore, the gains are chosen such that the Nyquist plots of $G_1(s)$ and $G_2(s)$ are completely contained in the right half of the complex plane (this is equivalent to passivity.) Once the constants k_1, k_2, k_3 and k_4 are determined by solving the LMI (4.32), k_5 and k_6 are adjusted to ensure the passivity of $G_1(s)$ and $G_2(s)$. Further, k_5 and k_6 are chosen as high as possible in order to reduce the estimation error.

Note 1. The term $\frac{1}{|i_r|_{max}^2}$ is added in $G_2(s)$ to compensate for the fact that the variable gain $|i_r|/|\hat{i}_r|$ does not occupy the whole of the first quadrant. This is similar to what is commonly done in the analysis of systems with sector non-linearities.

The process of tuning the gains of the observer can be summarised as follows:

- (i) Solve the LMI given in equation (4.32). Choose a feasible point of the LMI and calculate the matrix K_s . The choice must be such that values of $k_3 - 1$ and k_4 are considerably smaller than 1.

- (ii) Corresponding to the matrix K_s calculated in the previous step, choose k_5 and k_6 such that the transfer functions $G_1(s)$ and $G_2(s)$ are passive.
- (iii) Simulate the system with an observer having the above calculated gains and check if the estimation errors are within acceptable limits. If not then repeat the procedure with a different feasible point of the LMI.

4.4 Results and Discussion

The performance of proposed robust slip angle and speed observer are simulation and experimentally verified. The machine parameters are given in the Appendix A.

LMIs (4.24) and (4.32) have been solved using the LMI toolbox in MATLAB. The calculated values of the matrices L_h and K_s are as given below:

$$L_h = \begin{bmatrix} -5.7150 & 0.0139 \\ -0.0139 & -5.7150 \\ 4.8206 & 0.4365 \\ -0.4365 & 4.8206 \end{bmatrix}$$

$$K_s = \begin{bmatrix} -1.0297 & -0.0013 \\ -0.0004 & -0.1030 \end{bmatrix}$$

The values of k_5 and k_6 are chosen as 1 and 10, respectively, so as to ensure passivity and reduction in estimation error. These calculated gain values are used in both simulation and experiment.

4.4.1 Simulation Results

In order to test the robustness of the proposed observer, the DFIG system has been simulated in the power system CAD software, PSCAD/EMTDC. A change in the mode of operation of the machine from sub-synchronous to super-synchronous speed ranges has been simulated. Further, a sudden load change has also been simulated.

4.4.1.1 Case 1: Step Change in Reference Input Speed

Initially, the machine runs in the sub-synchronous generating mode where the rotor circuit is excited with RSC. At $t = 6.0$ s, speed reference is changed from 1404.5 rpm to 1643.2 rpm. Again,

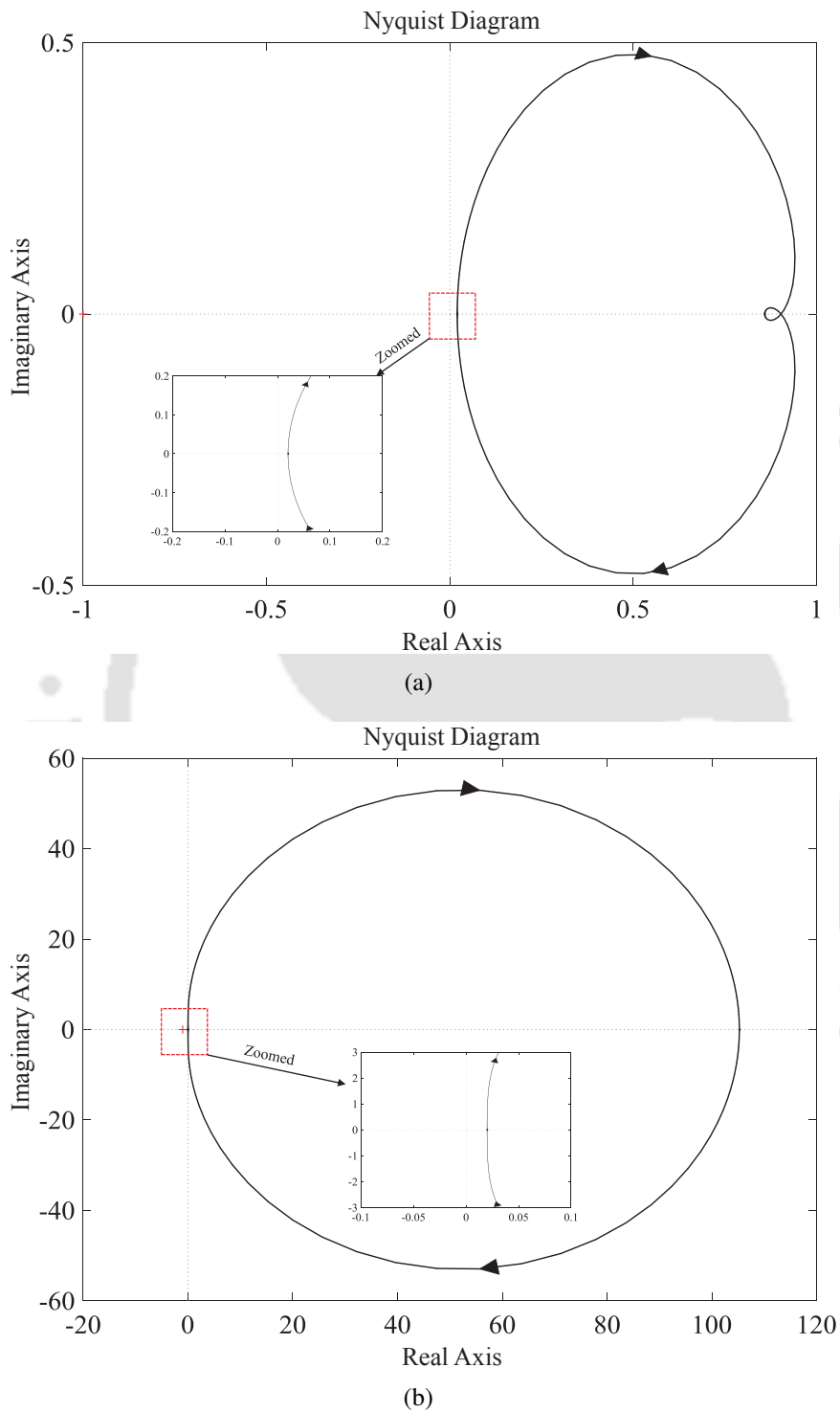


Figure 4.6: (a) Nyquist plot of $G_1(s)$ (b) Nyquist plot of $G_2(s)$.

at $t = 7.0$ s, a step command applied to change the rotor shaft speed from 1643.2 rpm to 1404.5 rpm. The corresponding slip changes from 20 rad/s to -30 rad/s and vice-versa. The Figure 4.7 shows the actual and estimated slip speed during speed variation of the rotor shaft. The estimated slip speed error is plotted in Figure 4.8. It is observed from the Figure 4.8 that the magnitude of the error is 0.11 rad/s. A small overshoot of ± 2.5 rad/s is also present in the slip speed error during speed variations. The estimated slip position during rotor shaft speed transition is given in Figure 4.9. Here, Window 1 and Window 2 represent the sub-synchronous to super-synchronous speed transition and super-synchronous to sub-synchronous speed transition respectively. The corresponding slip position estimation error is given in Figure 4.10. The magnitude of the slip position error is less than 0.5×10^{-3} rad during the same transition in speed. It is observed that estimated \hat{i}_{ar} and \hat{i}_{br} are converged to the

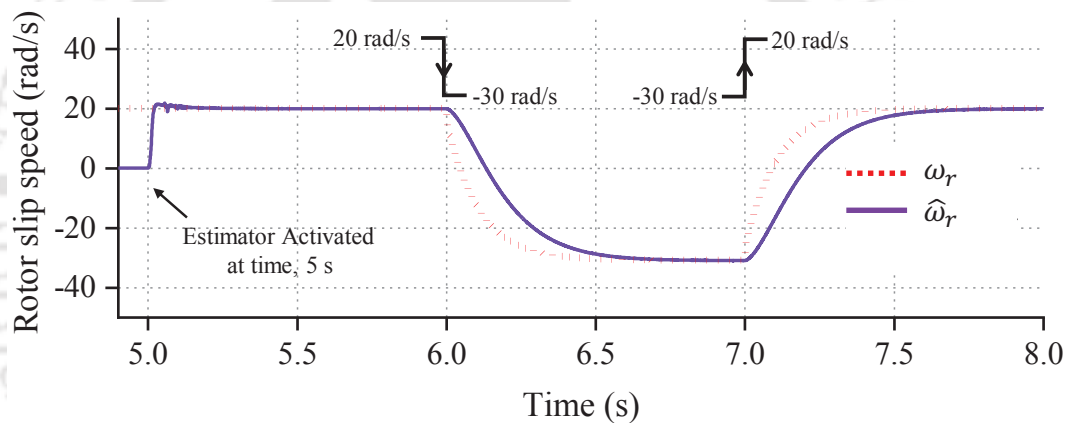


Figure 4.7: Estimated slip speed

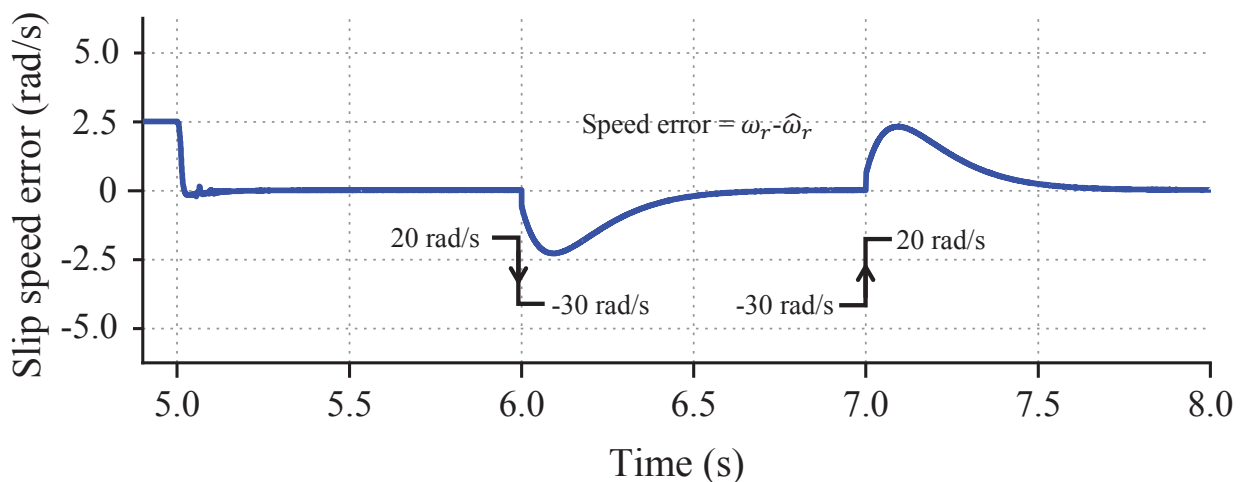


Figure 4.8: Estimated slip speed error

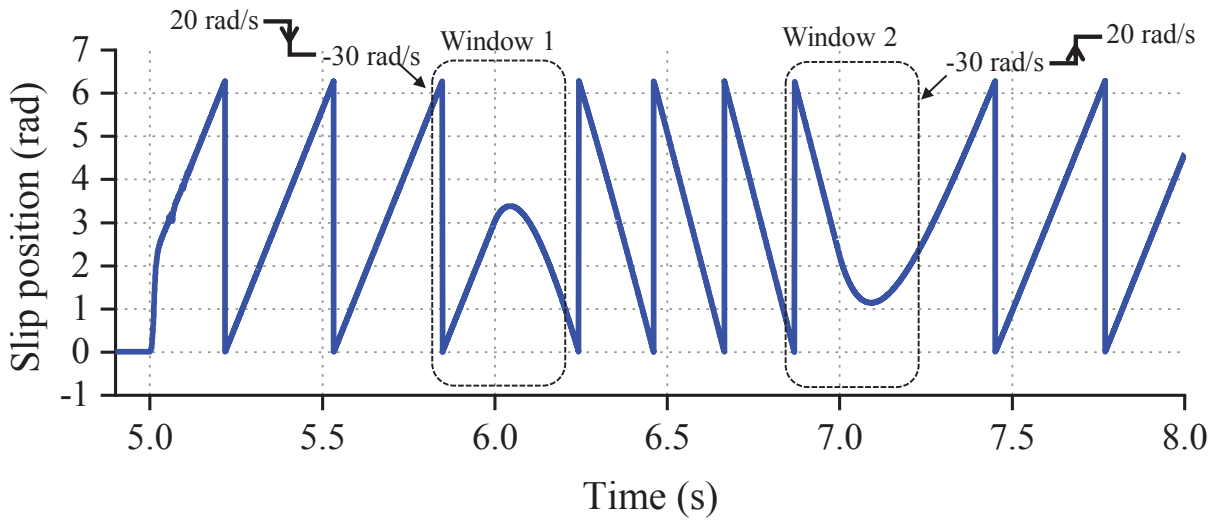


Figure 4.9: Estimated slip position

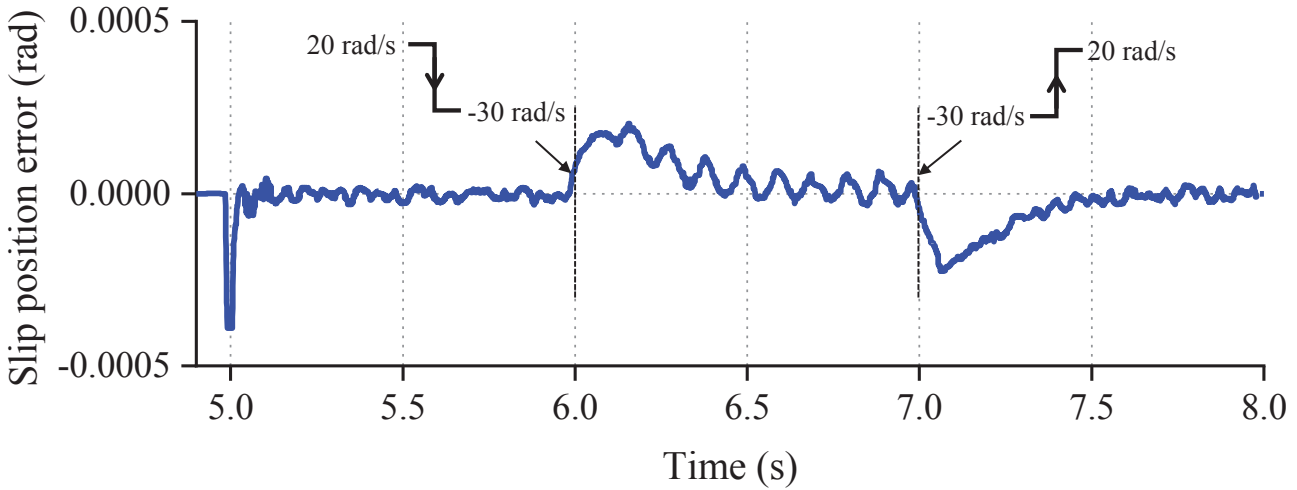


Figure 4.10: Slip position estimation error

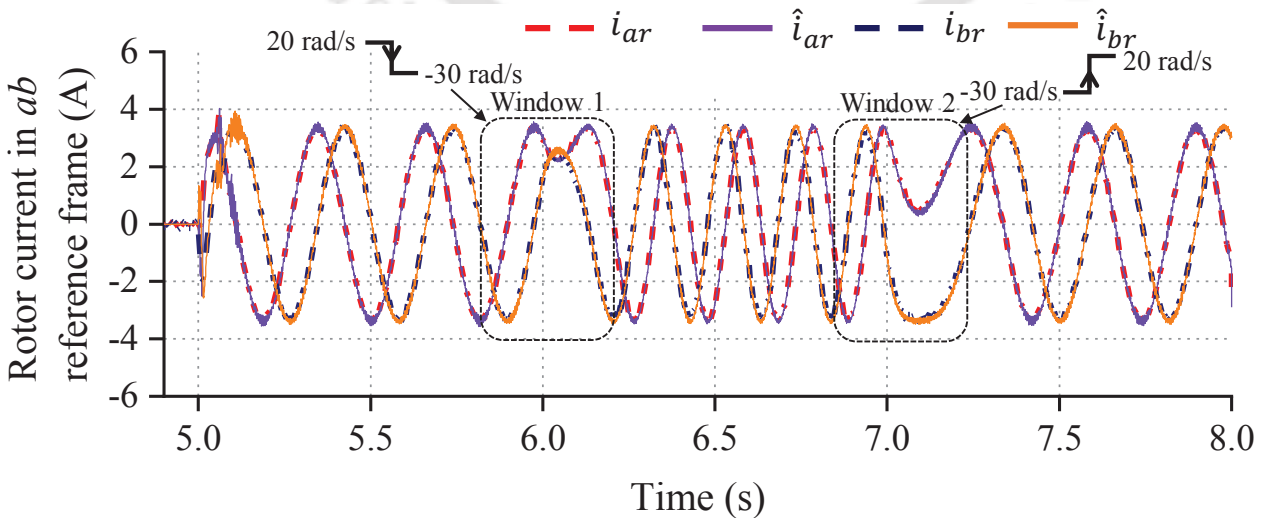


Figure 4.11: Estimated and actual rotor current components in ab reference frame

measured i_{ar} and i_{br} respectively as shown in Figure 4.11, which ensures the correct estimation of the slip position. It is also noted that i_{ar} lags i_{br} in the sub-synchronous mode, but relation reverses in the super-synchronous mode. This is due to the change in the slip direction while speed changes from sub-synchronous to super-synchronous speed range and vice-versa.

The above simulation results show a stable performance of the proposed algorithm during speed transition of sub-synchronous to super-synchronous range and vice-versa. The proposed H_∞ based algorithm shows better performance near the synchronous speed.

4.4.1.2 Case 2: Step Changes in the Load

In this case, the per phase resistive load (250Ω) is connected in the stator terminal of the machine. The resistive load is suddenly decreased to 50Ω from 250Ω at $t = 8.0$ s for a time period of 1.0 s. Again, a step change in resistive load from 50Ω to 150Ω is applied at time $t = 9.0$ s. The resistive load variation profile is given in Figure 4.12. The corresponding estimated slip speed and actual slip speed is shown in Figure 4.13. The corresponding slip speed estimation error magnitude is plotted in Figure 4.14. The slip speed error magnitude is 0.08 rad/s during load variation. The estimated slip speed converged within 0.10 s. The estimated slip position is shown in Figure 4.15 and the corresponding error is plotted in Figure 4.16. The estimated rotor current and actual rotor current is given in Figure 4.17. The estimated rotor current components and actual rotor current components is shown in Figure 4.17. The estimated rotor current components, \hat{i}_{ar} and \hat{i}_{br} are converged to the corresponding measured values within 0.1 s. This ensures the accurate estimation of slip position. The estimation error is plotted in Figure 4.15. The proposed algorithm tracks the actual rotor slip position within an error band of 0.9×10^{-6} rad. The peak overshoot is less than $\pm 0.5 \times 10^{-3}$ rad.

4.4.2 Experimental Results

The performance of the proposed estimator is experimentally verified on a laboratory setup. Further, an MRAS based observer (as given in [62]) has also been implemented on the same setup and the performance of the two estimators have been compared. The experimental setup consists of a DC motor coupled with DFIG. Here, the DC motor acts as a prime mover for emulating the wind turbine. The parameter of DFIG used in the experimental are same as in the simulation, i.e., as given in Table A.1. A floating point DSP (TMS320F28335) and TL084 wide band opamp based signal condition

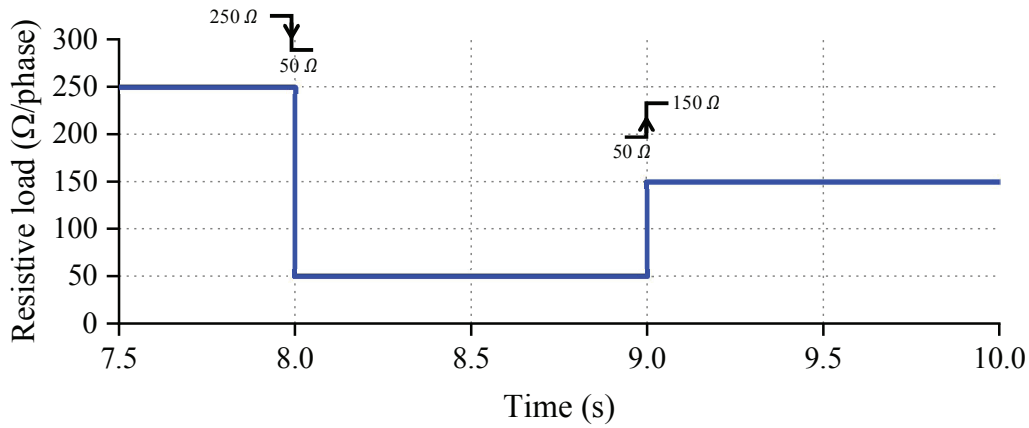


Figure 4.12: Per phase resistive load variation connected to the stator terminals during speed variation

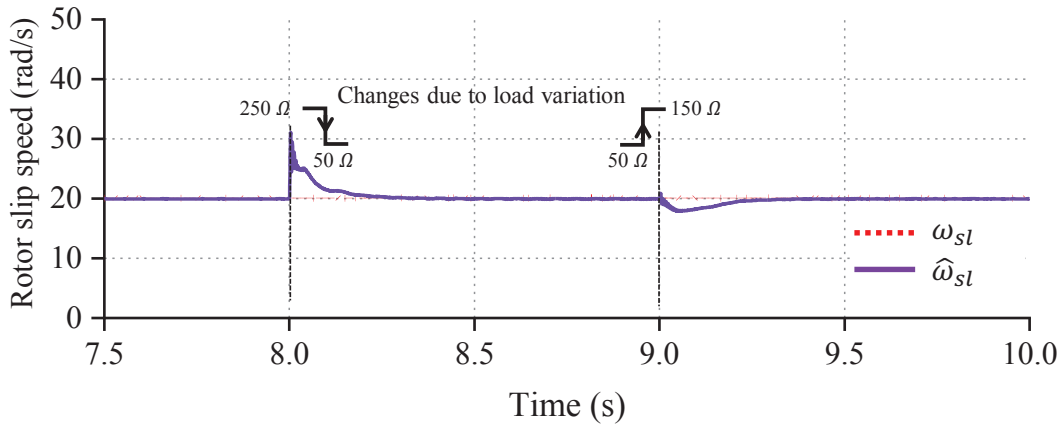


Figure 4.13: Estimated slip speed during load variation

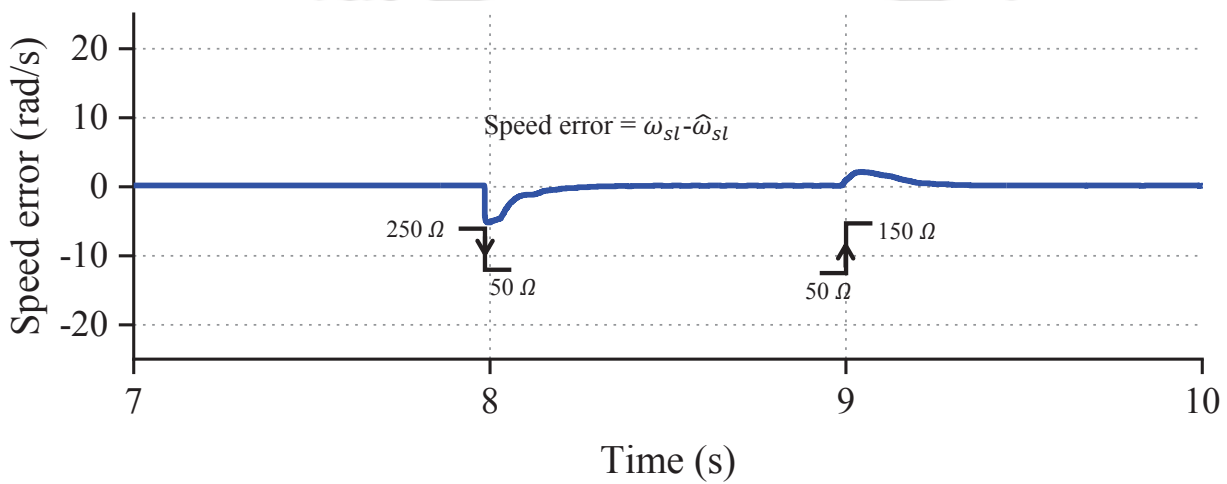


Figure 4.14: Slip speed estimation error during load variation

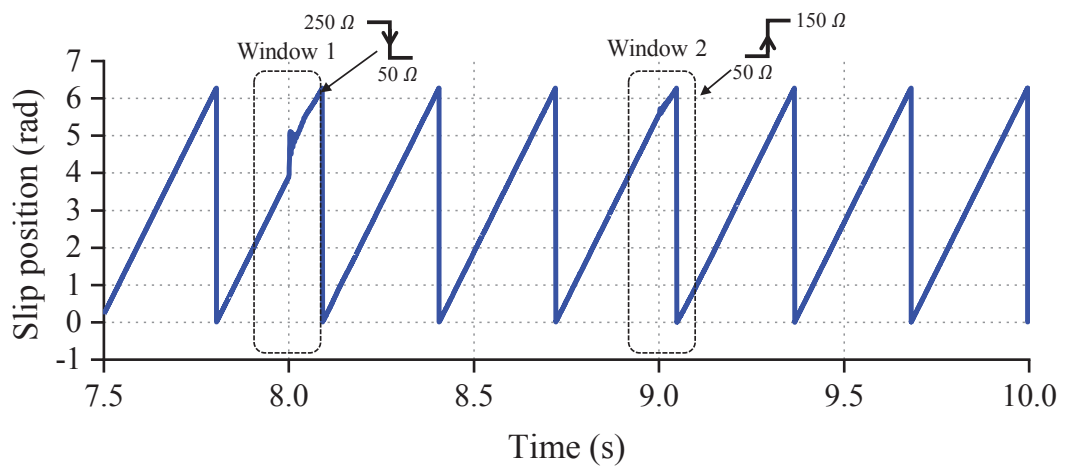


Figure 4.15: Estimated slip position

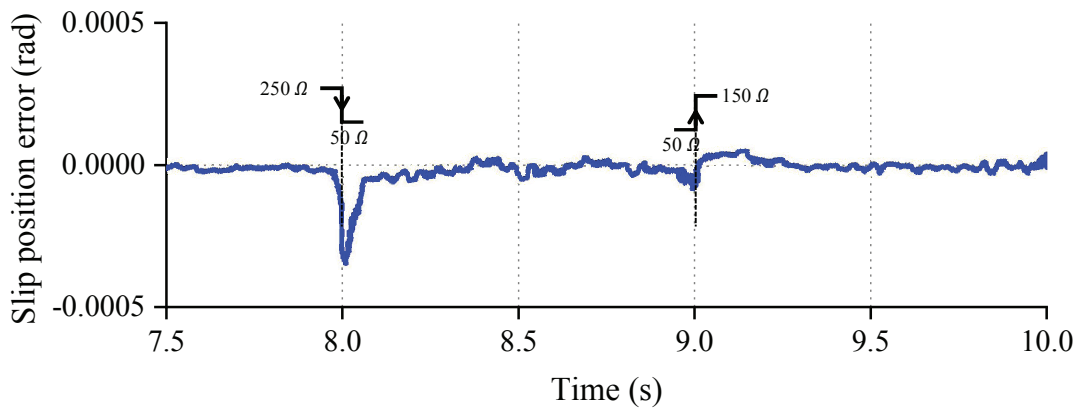


Figure 4.16: Slip position estimation error

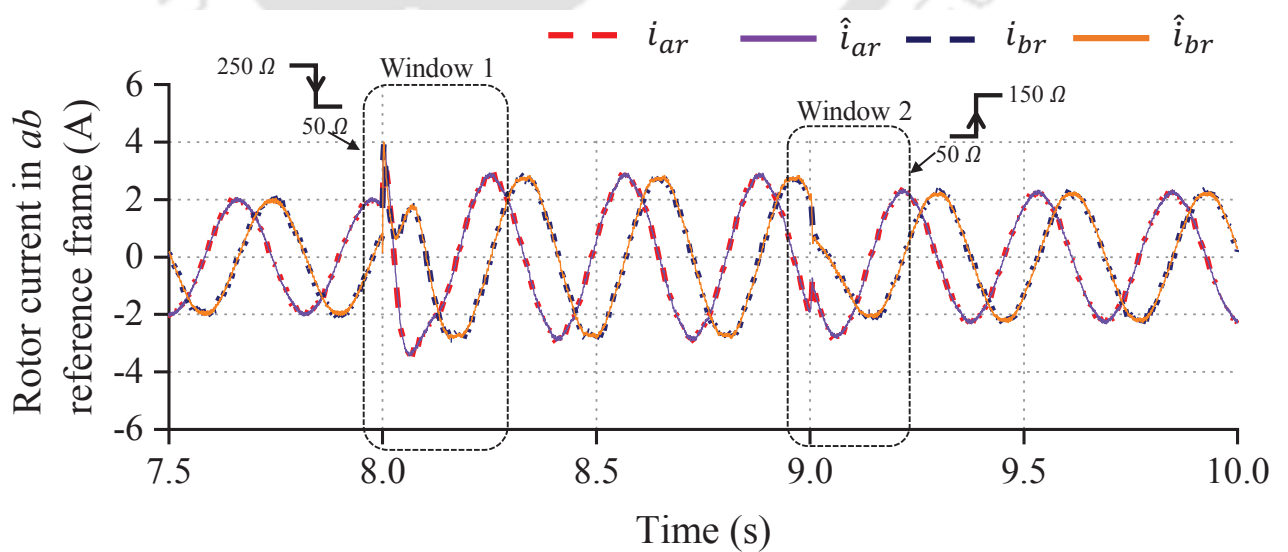


Figure 4.17: Estimated and actual rotor current components in ab reference frame during load variation

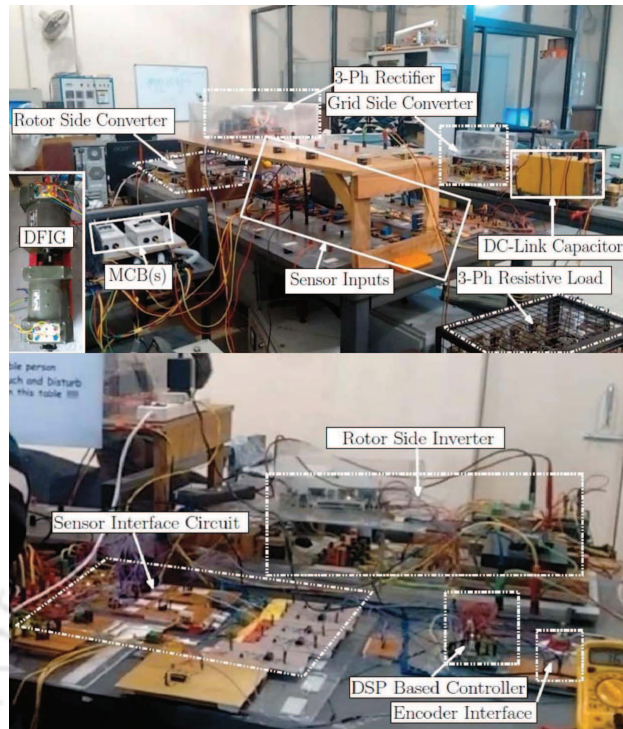


Figure 4.18: Laboratory Experimental setup for DFIG system

circuit is used to implement the proposed algorithm. In the implementation of algorithms, the PWM switching frequency is set at 2 kHz and the sampling time (T_s) of the ADC is set as $500 \mu s$, respectively. The estimated slip angle, by the proposed and MRAS estimators are converted to analog value using 12 bit four channel PWM DAC, and is displayed in the CRO along with other measurements obtained from voltage, current and speed sensor. For implementing inverter, Integrated Power Module (IPM) is used in the experimental setup.

As the DFIG is running in stand along mode, the grid is simulated as $3-\phi$, 50 Hz voltage source inside the DSP processor, and the voltage signal are given to SRF-PLL to provide ω_s and θ_s .

The performance of the estimator has been tested under the following conditions : 1) DFIG with constant rotor speeds of 1350 rpm and 1185 rpm 2) Change of the operating mode of the system from super-synchronous to sub-synchronous, and 3) A sudden load change from 300Ω to 150Ω .

4.4.2.1 Case 1: Constant Rotor Speed Operation

Figure 4.19 shows the slip angle estimated by the proposed and the MRAS based observer at 1350 rpm. The corresponding error plots are shown in Figure 4.20. To show the time correspondence between the two plots i.e., Figure 4.19 and Figure 4.20, the field current plot is shown in both Figures.

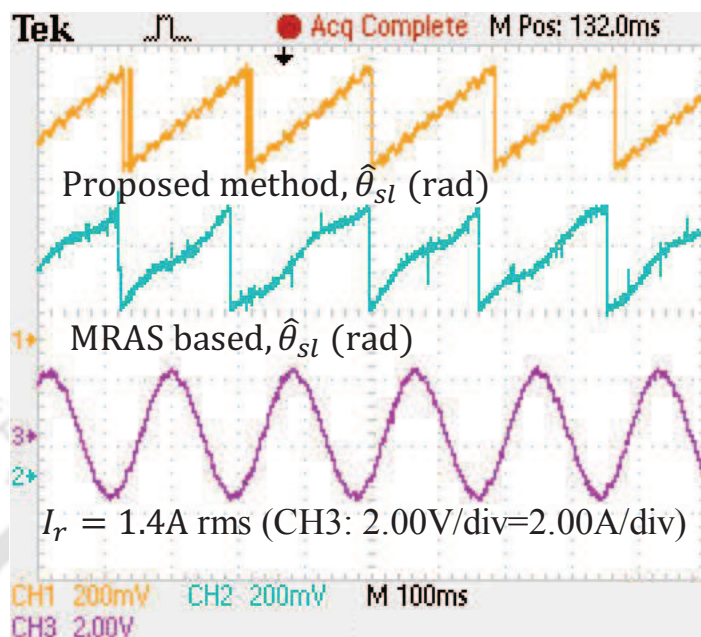


Figure 4.19: Performance of the proposed H_∞ based observer relative to MRAS based observer at a speed of 1350 rpm

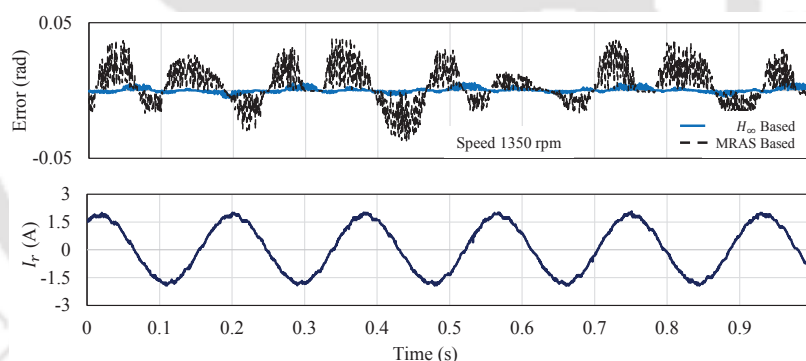


Figure 4.20: Error between H_∞ and MRAS observer at a speed of 1350 rpm

It can be observed from Figure 4.20, the deviation in the error for the MRAS estimator is higher than that of the proposed estimator. The maximum error for the MRAS estimator is 0.0421 rad at time $t = 0.3555$ s, whereas for the proposed estimator it is 0.002 rad at time $t = 0.525$ s. Thus the maximum error for the proposed estimator is approximately 20 times less than that for the MRAS estimator.

The slip angles estimated by the proposed and MRAS based observer at a speed of 1185 rpm are shown in 4.21. The corresponding error plots are given in Figure 4.22. The maximum error for the MRAS estimator is 0.04884 rad at time $t = 0.0244$ s, whereas for the proposed estimator it is 0.01339

rad at time $t = 0.46$ s. Thus the maximum error for the proposed estimator is approximately 4 times less than that for the MRAS observer.

4.4.2.2 Case 2: Change of the Operating Mode of the System from Super-synchronous to Sub-synchronous

Figure 4.23 shows the slip angles estimated by the proposed and the MRAS based observers (along with the rotor current) when the speed changes from 1550 rpm (super-synchronous) to 1485 rpm (sub-synchronous). The corresponding error plots are given in Figure 4.24. It can be observed that the error for the proposed estimator increases during the transition. However, this is significantly less than the corresponding error for the MRAS estimator. Hence, the proposed estimator is quite

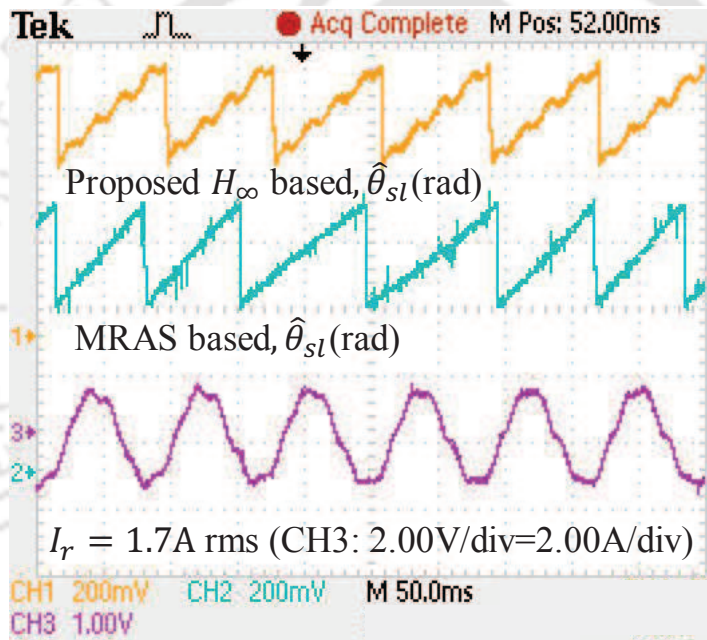


Figure 4.21: Performance of the proposed H_∞ based observer relative to MRAS based observer at a speed of 1185 rpm

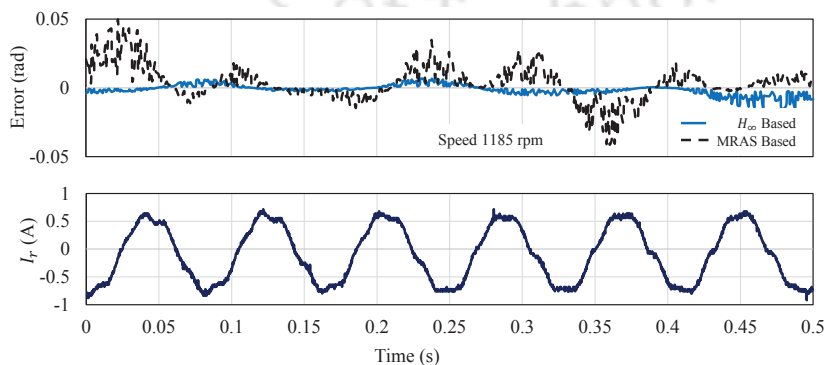


Figure 4.22: Error between H_∞ and MRAS observer at a speed of 1185 rpm

effective when the machine shifts from the super-synchronous to the sub-synchronous mode.

4.4.2.3 Case 3: Operation in Sudden Load Change

Figure 4.25 shows the slip angles estimated by the proposed observer and the MRAS based observer (along with the rotor current), when there is a step change of resistive load from 300 Ω to 150 Ω. From the error plot given in Figure 4.26, it can be observed that in the immediate aftermath of the change of load at $t = 1.15\text{sec}$, the error for the MRAS estimator increases to around 0.047rad . On the other hand, the corresponding error for the proposed estimator is much lower. Thus, the proposed estimator is more accurate than the MRAS estimator during a sudden load variation.

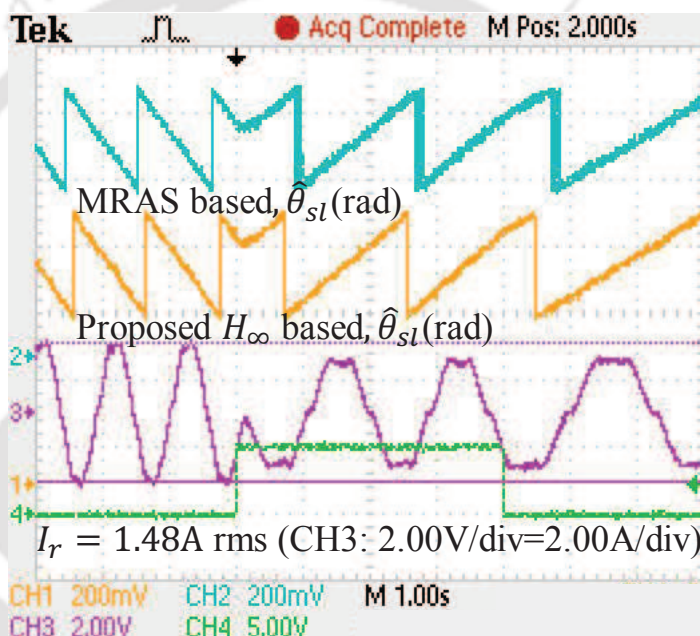


Figure 4.23: Relative performance of the proposed H_∞ based observer at close to synchronous speed with respect to MRAS based observer and the rotor phase current.

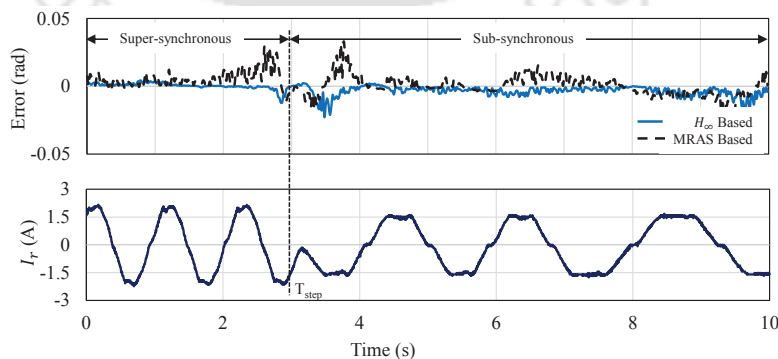


Figure 4.24: Error between H_∞ and MRAS observer during changed from subsynchronous to supersynchronous

w

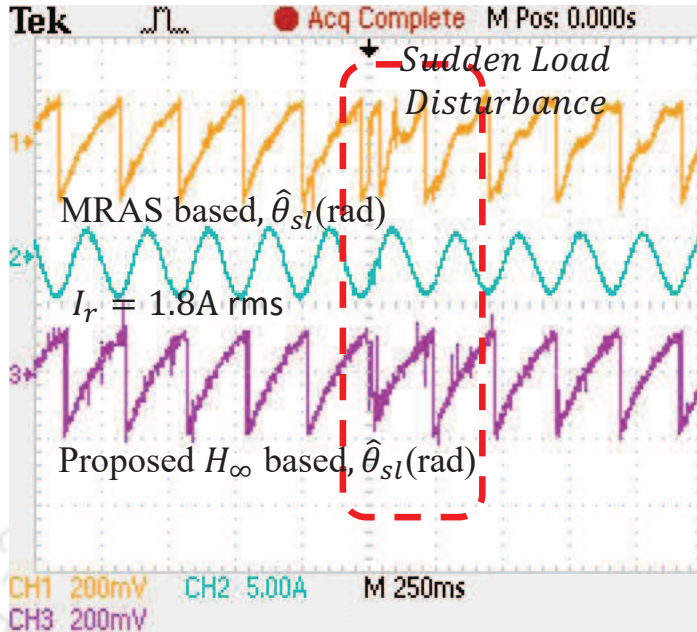


Figure 4.25: Slip position estimator results during sudden load variation.

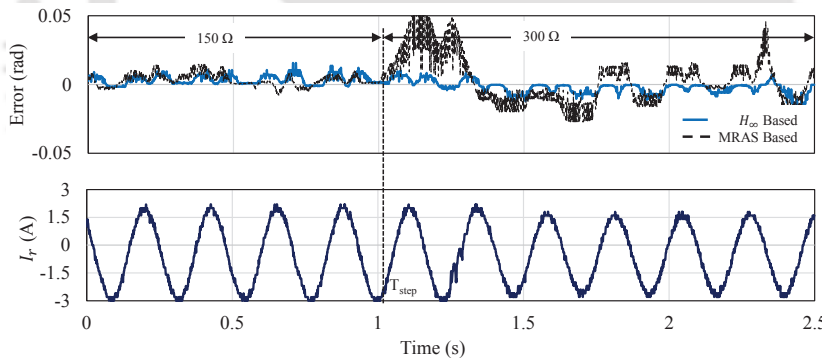


Figure 4.26: Error between H_∞ and MRAS observer during sudden load variation

4.5 Conclusion

This Chapter has proposed a robust slip angle and speed observer for variable speed constant frequency DFIG system. The effectiveness of the observer has been tested on a laboratory 3 Hp DFIG system. The proposed observer provides an accurate estimate of the slip position and speed of the rotor, which is robust to load disturbance and speed changes.

In addition, the paper also provides an tuning procedure of the gain values of the observer.

5

State Estimation of DFIG using an Extended Kalman Filter with an Augmented State Model

Contents

5.1	Introduction	92
5.2	Extended Kalman Filter	92
5.3	Augmented State Model of DFIG	94
5.4	Simulation Results	96
5.5	Conclusion	102

5.1 Introduction

The stochastic behavior of wind flow and the nonlinearity of wind turbine model gives rise to various challenges in design and control of WECS [4]. Field oriented control (FOC) is commonly used to control the dynamics of DFIG which enables decoupled control of active and reactive power. The performance of FOC strategy depends on the accurate information of rotor position. Usually, both rotor position and rotor speed can be acquired using encoders. Due to various limitations in rotor position sensing using mechanical encoders, a sensorless approach is considered. A predictor-corrector based closed loop rotor slip-position estimator is discussed in chapter 2. The proposed slip-position estimator algorithm is mainly based on the stator flux based estimation technique.

However, the speed estimation of DFIG is not dealt with in chapter 2. Several literature on the research area of rotor position and speed estimation are presented. Open loop speed and position estimators have been dealt with in [31, 52]. The use of closed loop observers have been discussed in [43, 54, 55, 58]. They are mainly based on the model reference adaptive systems (MRAS). The performance of an MRAS based observer is highly sensitive to the inductance value [53]. Another possible way of estimating the dynamic states of a DFIG is by the use of recursive methods like the Extended Kalman Filter [63].

In this chapter, an Extended Kalman Filter based method is proposed that uses an augmented state model in order to dynamically obtain an accurate estimate of rotor position and speed. The dynamic model of a DFIG system is discussed in details in APPENDIX B. The proposed augmented state model for the Extended Kalman Filter (EKF) is presented in this chapter. The effectiveness of the proposed EKF model is demonstrated through simulation results.

5.2 Extended Kalman Filter

Extended Kalman Filter is widely used for estimating unmeasured states in a nonlinear process. Consider a nonlinear system with the following state space equations,

$$\mathbf{x}(\mathbf{k}) = f\{\mathbf{x}(\mathbf{k} - 1), \mathbf{u}(\mathbf{k} - 1)\} + \mathbf{w}(\mathbf{k} - 1) \quad (5.1)$$

$$\mathbf{z}(\mathbf{k}) = h\{\mathbf{x}(\mathbf{k})\} + \mathbf{v}(\mathbf{k}) \quad (5.2)$$

where, $\mathbf{x}(\mathbf{k})$ and $\mathbf{z}(\mathbf{k})$ be the process state vector and measurement output vector respectively. \mathbf{w} and \mathbf{v} are assumed zero mean normal distributed noise perturbations. These perturbations could be model uncertainties or external disturbances. The process and measurement noise covariance matrices are given by:

$$\text{cov}(\mathbf{w}) = E\{\mathbf{w}\mathbf{w}^T\} = \mathbf{Q}$$

$$\text{cov}(\mathbf{v}) = E\{\mathbf{v}\mathbf{v}^T\} = \mathbf{R}$$

The Extended Kalman Filter is a two step algorithm. The first step involves the prediction, and the second one is the correction step. For the Extended-Kalman Filter, the predictor step is given by,

$$\hat{\mathbf{x}}(\mathbf{k})^- = f\{\mathbf{x}(\mathbf{k}-1), \mathbf{u}(\mathbf{k}-1)\}$$

$$\mathbf{P}_k(\mathbf{k})^- = \mathbf{F}(\mathbf{k}-1)\mathbf{P}_k(\mathbf{k}-1)\mathbf{F}^T(\mathbf{k}-1) + \mathbf{Q}(\mathbf{k})$$

where, the Jacobians are defined as,

$$\mathbf{F}(\mathbf{k}) = \left. \frac{\partial f(\mathbf{x}, \mathbf{u})}{\partial \mathbf{x}} \right|_{x(\mathbf{k}-1), u(\mathbf{k}-1)} \quad (5.3)$$

$$\mathbf{H}(\mathbf{k}) = \left. \frac{\partial h(\mathbf{x})}{\partial \mathbf{x}} \right|_{x(\mathbf{k}-1)} \quad (5.4)$$

$\hat{\mathbf{x}}(k)^-$ and $\mathbf{P}_k(k)^-$ are apriori states, and the corrector step is given by,

$$\mathbf{K}_g(\mathbf{k}) = \mathbf{P}_k(\mathbf{k})^- \mathbf{H}^T(\mathbf{k}) \left\{ \mathbf{H}(\mathbf{k})\mathbf{P}_k(\mathbf{k})^- \mathbf{H}^T(\mathbf{k}) + \mathbf{R}(\mathbf{k}) \right\}^{-1}$$

$$\hat{\mathbf{x}}(\mathbf{k}) = \hat{\mathbf{x}}(\mathbf{k})^- + \mathbf{K}_g(\mathbf{k})\{\mathbf{z}(\mathbf{k}) - h\{\mathbf{x}(\mathbf{k})^-\}\}$$

$$\mathbf{P}_k(\mathbf{k}) = \{\mathbf{I} - \mathbf{K}_g(\mathbf{k})\mathbf{H}(\mathbf{k})\}\mathbf{P}_k(\mathbf{k})^-$$

In the above equations $\mathbf{P}_k(\mathbf{k})$ is an estimate of the covariance of the measurement error and $\mathbf{K}_g(\mathbf{k})$ is called the Kalman gain. After both the prediction and correction steps have been performed then $\hat{\mathbf{x}}(\mathbf{k})$ is the current estimate of the states and $\hat{\mathbf{z}}(\mathbf{k})$ can be calculated directly from it. Both $\hat{\mathbf{x}}(\mathbf{k})$ and $\mathbf{P}_k(\mathbf{k})$ are stored and used in the predictor step of the next time period.

5.3 Augmented State Model of DFIG

The dynamic model of DFIG is a set of continuous-time nonlinear differential equations as expressed by Eq. (B.27)-(B.42). Based on the nonlinear dynamic model of DFIG, the following process state vector and measurement output vector can be defined [63]:

$$\begin{aligned}\mathbf{x} &= [i_{\alpha s}; i_{\beta s}; i_{\alpha r}; i_{\beta r}; \omega_r; \theta_r] \\ &= [x_1; x_2; x_3; x_4; x_5; x_6]\end{aligned}\quad (5.5)$$

$$\mathbf{z} = [i_{\alpha s} \ i_{\beta s} \ i_{\alpha r} \ i_{\beta r}]^T \quad (5.6)$$

By using the state vector in Eq. (5.5), the steady state error is persistent while estimating the rotor position in presence of transient dynamics. To mitigate the steady state error we partially augmented the state vector with integral of currents as given by:

$$\begin{aligned}\mathbf{x} &= \left[i_{\alpha s}; i_{\beta s}; i_{\alpha r}; i_{\beta r}; \omega_r; \theta_r; \int i_{\alpha s} dt; \int i_{\beta s} dt; \right. \\ &\quad \left. \int i_{\alpha r} dt; \int i_{\beta r} dt \right] \\ &= [x_1; x_2; x_3; x_4; x_5; x_6; x_7; x_8; x_9; x_{10}]\end{aligned}\quad (5.7)$$

To further mitigate the steady state error, we augment the state vector with integral of square of currents which is as given below:

$$\begin{aligned}\mathbf{x} &= \left[i_{\alpha s}; i_{\beta s}; i_{\alpha r}; i_{\beta r}; \omega_r; \theta_r; \int i_{\alpha s} dt; \int i_{\beta s} dt; \right. \\ &\quad \left. \int i_{\alpha r} dt; \int i_{\beta r} dt; \int i_{\alpha s}^2 dt; \int i_{\beta s}^2 dt; \right. \\ &\quad \left. \int i_{\alpha r}^2 dt; \int i_{\beta r}^2 dt \right] \\ &= [x_1; x_2; x_3; x_4; x_5; x_6; x_7; x_8; x_9; x_{10}; \\ &\quad x_{11}; x_{12}; x_{13}; x_{14}]\end{aligned}\quad (5.8)$$

Eq. (5.5), (5.7) and (5.8) are denoted as EKF, EKF normal and EKF improvement. The EKF normal is a modification of EKF with addition of integral of currents. The EKF improvement is an modification of EKF normal with addition of square of integral of currents. The addition of integral

states by augmenting the state equations will reduce the steady-state error.

For implementation of Extended Kalman Filter, the DFIG model should be discretized. Using backward Euler's method,

$$\frac{dx(t)}{dt} = \frac{x(k) - x(k-1)}{\Delta t}; \quad (k-1)\Delta t \leq t \leq k\Delta t,$$

we can get discrete form of machine state equations are as follows:

$$x_1(k) = x_1(k-1) + \Delta t \left. \frac{dx_1}{dt} \right|_k \quad (5.9)$$

$$x_2(k) = x_2(k-1) + \Delta t \left. \frac{dx_2}{dt} \right|_k \quad (5.10)$$

$$x_3(k) = x_3(k-1) + \Delta t \left. \frac{dx_3}{dt} \right|_k \quad (5.11)$$

$$x_4(k) = x_4(k-1) + \Delta t \left. \frac{dx_4}{dt} \right|_k \quad (5.12)$$

$$x_5(k) = x_5(k-1) + \Delta t \left\{ \frac{K_t P}{2J} \{x_3(k)x_2(k) - x_1(k)x_4(k)\} - \frac{K_t P}{2J} T_t \right\} \quad (5.13)$$

$$x_6(k) = x_6(k-1) + \Delta t x_5(k) \quad (5.14)$$

where, $K_t = \frac{3}{2} \frac{P}{2} L_m$. The discrete time integral states are defined using bilinear transform as:

$$x_{i+6}(k) = x_{i+6}(k-1) + \Delta t \left\{ \frac{x_i(k) + x_i(k-1)}{2} \right\} \quad (5.15)$$

$$x_{i+10}(k) = x_{i+10}(k-1) + \Delta t \left\{ \frac{x_i^2(k) + x_i^2(k-1)}{2} \right\} \quad (5.16)$$

where, Δt is the sampling time and i varies from 1 to 4. The derivatives used in Eq. (5.9) - (5.12) correspond to the Eq. (B.37) - (B.42).

The input and measurement state vectors are as follows:

$$\mathbf{u} = [V_{\alpha s} \ V_{\beta s} \ V_{\alpha r} \ V_{\beta r}]^T \quad (5.17)$$

$$\mathbf{z} = [i_{\alpha s} \ i_{\beta s} \ i_{\alpha r} \ i_{\beta r}]^T \quad (5.18)$$

In this work, the values of \mathbf{Q} and \mathbf{R} are determined with extensive simulation to achieve satisfactory results. Note that the initial value of $\mathbf{P}_k (\neq \mathbf{0})$ is chosen to converge the Extended Kalman Filter.

The \mathbf{Q} , \mathbf{R} and \mathbf{P}_k are given as follows:

$$\mathbf{Q} = \text{diag}([1.5 \ 1.5 \ 1.5 \ 1.5 \ 1e-4 \ 1e-6 \ 10e-10 \ 10e-10 \ 10e-10 \ 10e-10 \ 10e-10 \ 10e-10 \ 10e-10 \ 10e-10 \ 10e-10 \ 10e-10]);$$

$$\mathbf{R} = \text{diag}([10e-2 \ 10e-2 \ 10e-2 \ 10e-2]);$$

$$\mathbf{P}_k(\text{initial}) = \text{diag}([1 \ 1 \ 1 \ 1 \ 1 \ 1 \ 1 \ 1 \ 1 \ 1 \ 1 \ 1 \ 1 \ 1 \ 1]);$$

5.4 Simulation Results

The effectiveness of proposed estimator using Extended Kalman Filter is validated by simulation using *MATLAB/Simulink*. For simulating the proposed algorithm, DFIG parameters used are given in Appendix A. The proposed algorithm is tested under the following test conditions,

- 1) Initial operation at constant speed reference of 325 rad/s.
- 2) Step change of Speed reference from 325 rad/s to 360 rad/s.
- 3) Short Circuit of Stator terminals.
- 4) Step change of Speed reference from 360 rad/s to 310 rad/s.
- 5) Step reduction of turbine torque reference by 50%.

5.4.1 Case 1: Operation at Constant Speed Reference

At initial phase, the rotor speed reference is maintained at 325 rad/s. The rotor speed corresponding to this reference is 1553 rpm. The rotor completes one revolution in a duration of 0.0193 s. The rotor speed response is given in Window-1 of Figure 5.1. It is observed that the proposed observer converges to the given reference in 2.5 s. The estimated rotor speed is shown in Window-1 of Figure 5.2. The turbine torque and the DFIG torque are plotted in Window-1 of Figure 5.3.

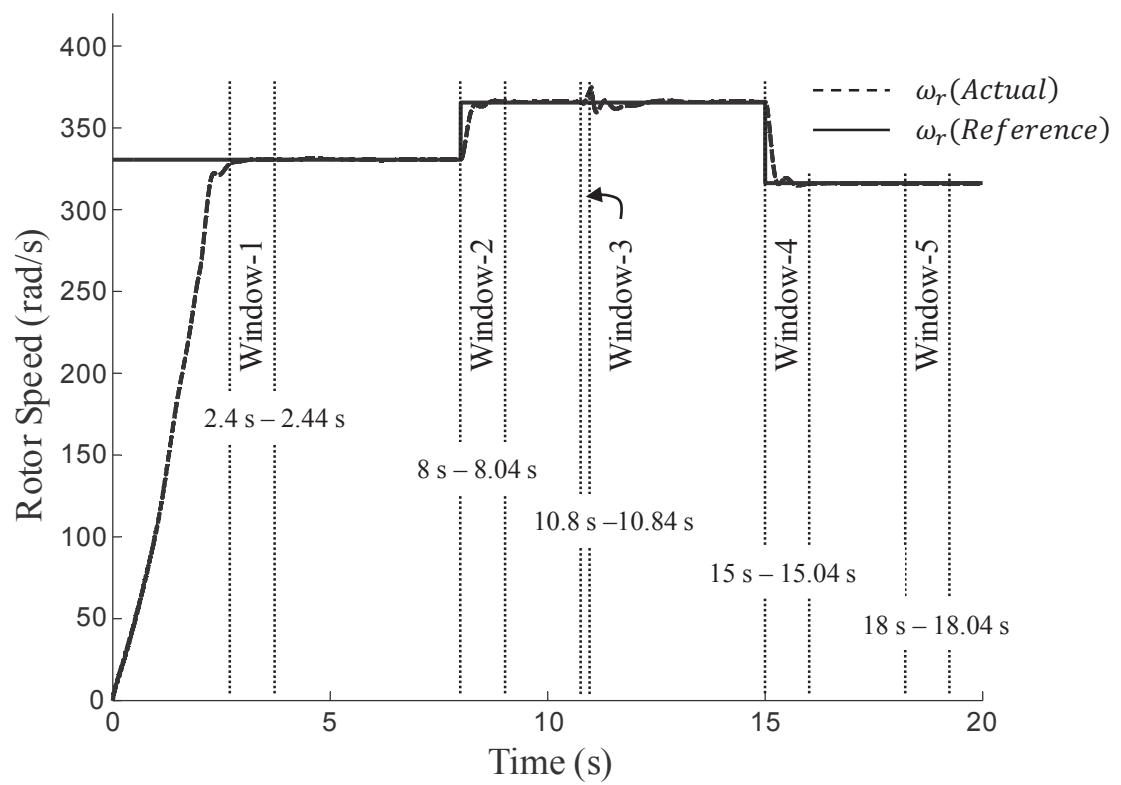


Figure 5.1: Speed profile of DFIG.

5.4.2 Case 2: Step Change of Speed Reference in Super-synchronous Mode

In simulation, a step command is applied from 325 rad/s to 360 rad/s to achieve the speed control response, at time $t = 8$ s. At 360 rad/s, the rotor speed is at 1720 rpm. One complete revolution of rotor is completed in 0.0174 s. In Window-2 of Figure 5.1 and Figure 5.2, the rotor speed response and the estimated rotor speed are given respectively. The Window-2 of Figure 5.3 shows the plot of the turbine torque and the DFIG torque.

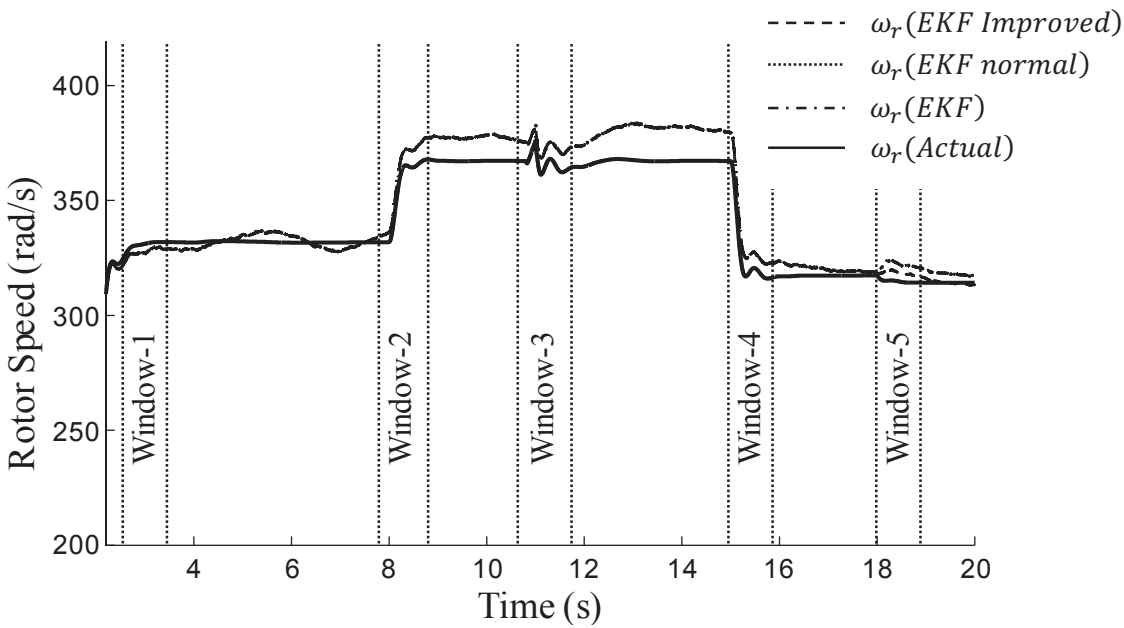


Figure 5.2: Estimated and actual rotor speeds of DFIG.

5.4.3 Case 3: Short Circuit of Stator Terminals at Super-synchronous Speed

At time $t = 10.8$ s, the stator terminal was short circuited. It is observed that after 200ms, the machine retrieved it's rated voltage. The rotor speed response during this condition is given in Window-3 of Figure 5.1 and the turbine torque and the DFIG torque are given in Window-3 of Figure 5.3. The output of the proposed estimator is given in Window-3 of Figure 5.2.

5.4.4 Case 4: Step Change of Speed Reference from Super-synchronous to Sub-synchronous Mode

A step change in speed reference is applied from supersynchronous speed of 360 rad/s to subsynchronous speed of 310 rad/s at time $t = 15$ s. Under above simulation scenario, the speed response of the DFIG is shown in Window-4 of Figure 5.1. The turbine torque and DFIG torque of the system are

given in Window-4 of Figure 5.3. The estimator response is shown in Window-4 of Figure 5.2.

5.4.5 Case 5: Step Reduction of Turbine Torque Reference

A step reduction in the turbine torque by 50% is set at time $t = 18$ s. Window-5 of Figure 5.3 shows the torque response of the turbine. In this case small amount of white gaussian noise $\sim \mathcal{N}(0, \sigma^2)$ is added to get turbine torque dynamics. The actual speed response of the rotor and the estimator response during this condition are shown in Window-5 of Figure 5.1 and Figure 5.2 respectively.

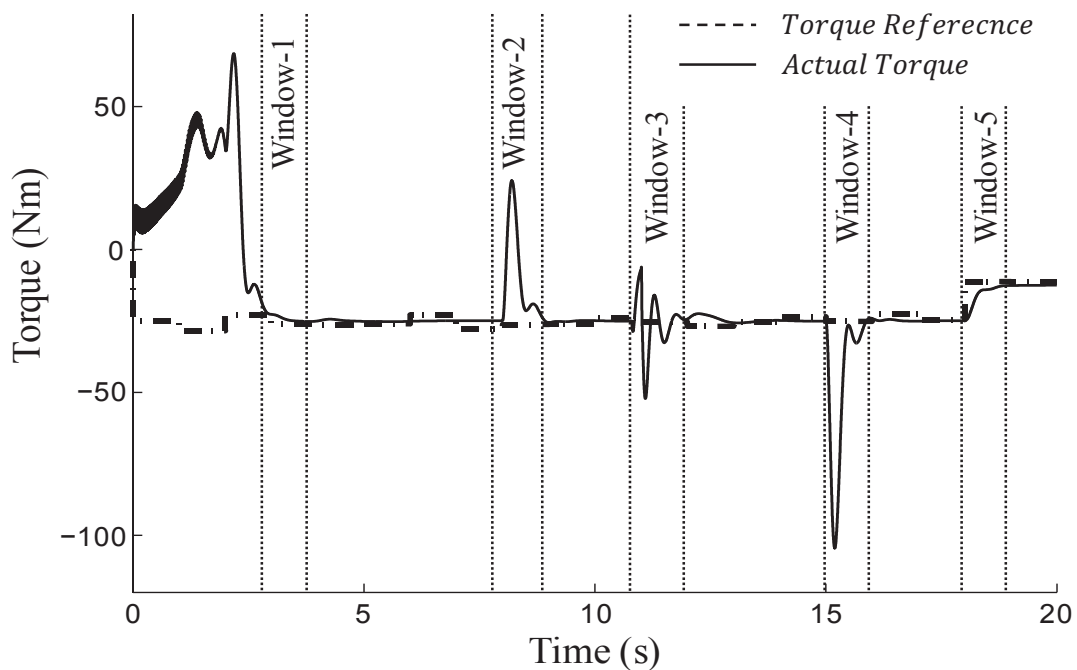


Figure 5.3: Turbine torque (T_t) and DFIG Torque (T_e) responses.

The simulation stop time is fixed at 20 s with sampling time, $\Delta t = 0.0005$ s. Continuously prediction and correction steps are iterated which allows the on-line estimation of the DFIG state vector.

The estimated and actual rotor speeds are shown in the Figure 5.2. It is observed that a small error is present in the estimated speed.

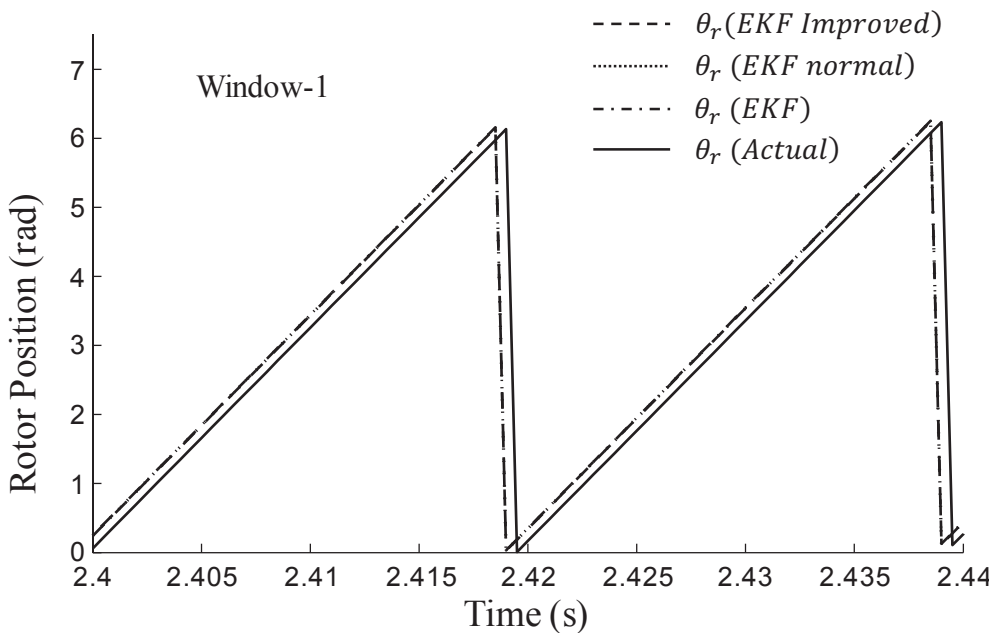


Figure 5.4: Estimated and actual rotor positions during starting of DFIG.

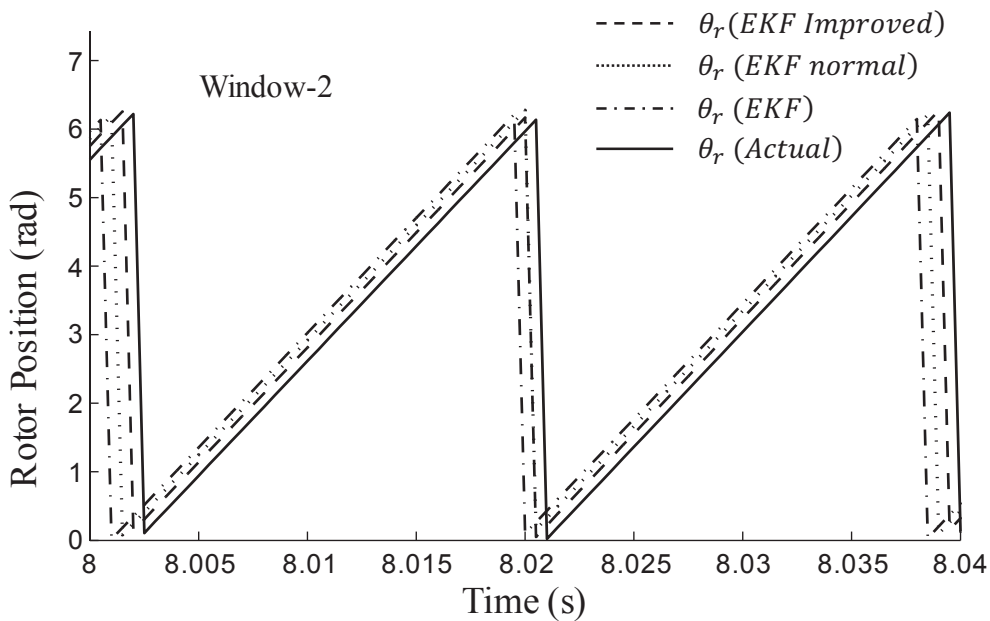


Figure 5.5: Estimated and actual rotor positions during step change of DFIG rotor speed.

The estimated and actual rotor positions are shown in Figures 5.4 - 5.8. It was observed that the proposed state model achieves less error with introduction of both both integral of stator and rotor current vectors and integral of square of the stator and rotor current vectors as defined in the (5.8).

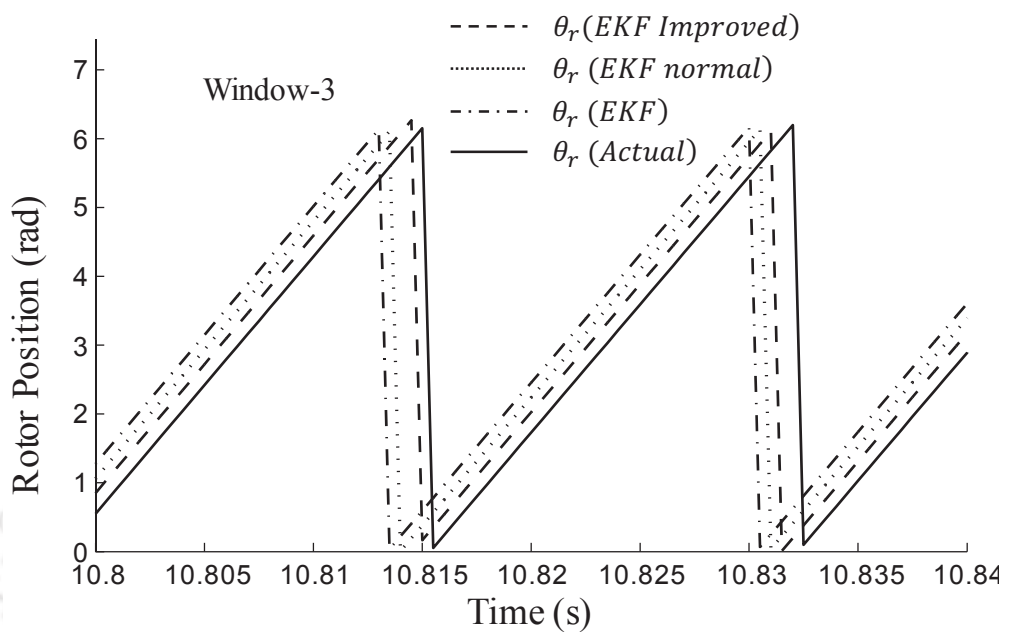


Figure 5.6: Estimated and actual rotor positions during short circuit of stator terminals.

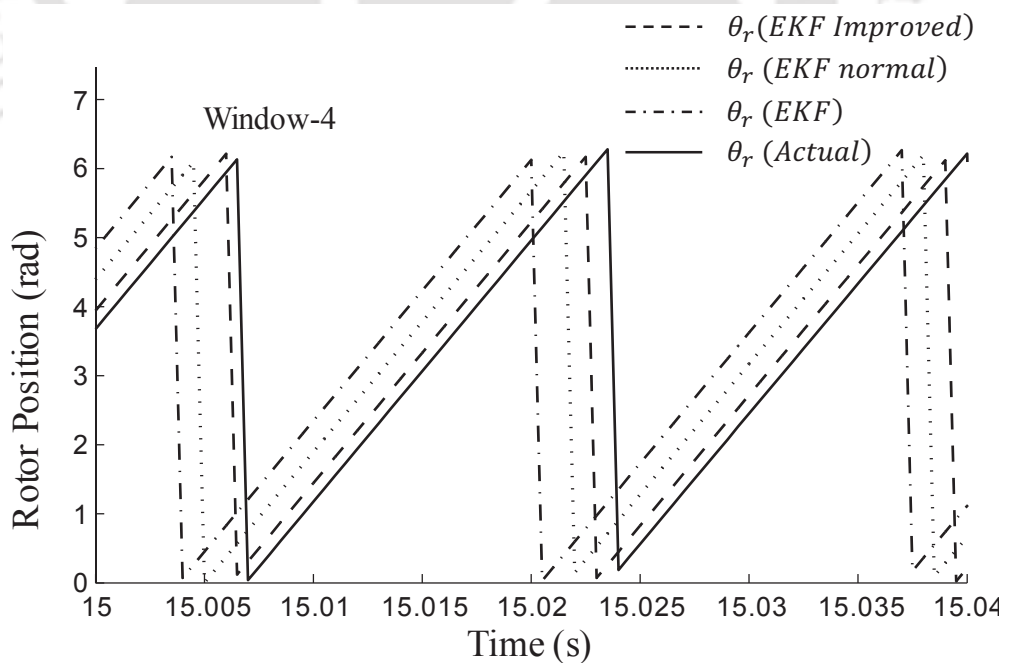


Figure 5.7: Estimated and actual rotor positions during rotor speed almost equal to the synchronous speed.

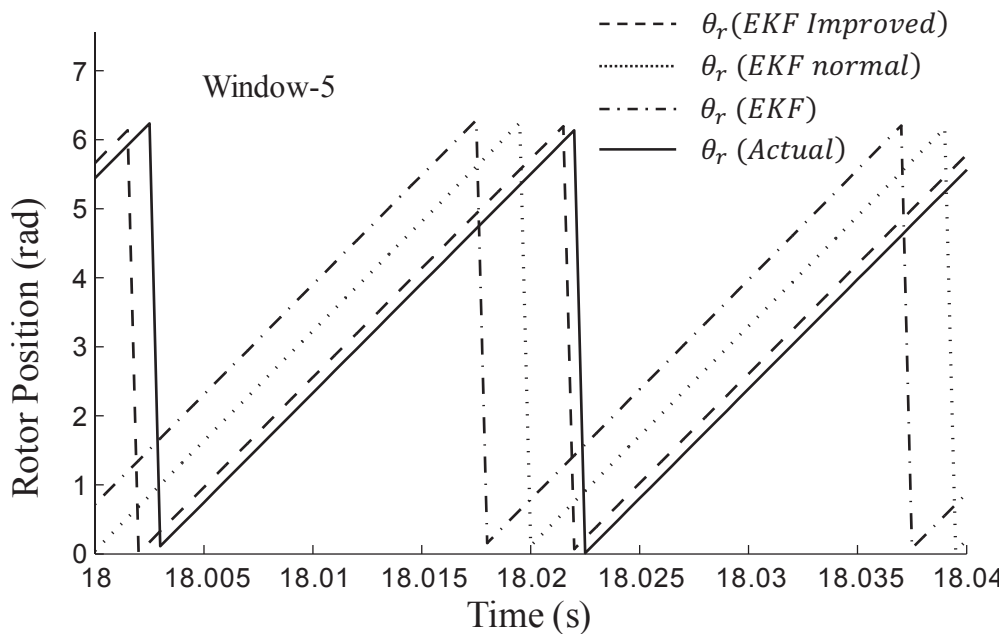


Figure 5.8: Estimated and actual rotor positions during step change of turbine torque.

5.5 Conclusion

In this chapter, we have proposed an Extended Kalman Filter based rotor speed and position estimator using an augmented state model. A comparative analysis of the performance of an Extended Kalman Filter was done for the following three types of state model: (a) without integral states (non-augmented state model) (b) with integral of stator and rotor current (partially augmented state model), and (c) with integral of stator and rotor current and integral of square of the stator and rotor currents (augmented state model). The performance of the estimators have been analyzed under various dynamic conditions. For the cases simulated, the proposed augmented state estimator showed the best performance.

6

Conclusion and Future Works

Contents

6.1	General	104
6.2	Summary of Important Findings	104
6.3	Scope of Future Research Work	106

6.1 General

DFIG is an attractive solution for a variable speed constant frequency drive system. Since the power converter is connected to the rotor circuit, an accurate rotor position estimate is critical to the performance of the control strategy for the rotor side converter. Further, to avoid the drawbacks of a mechanical encoder, sensorless operation is preferred. However, to develop a sensorless control system, transformation from the synchronous reference frame to the rotor reference frame is mandatory. This needs an accurate estimation of the slip position. The main contribution of this thesis is the design and development of robust slip position and speed estimation methods for a standalone DFIG system. The estimation schemes are validated and analyzed using a simulation study. Further, these schemes have been tested on a real-time hardware setup of a standalone DFIG system in the laboratory. The estimation algorithms are implemented on a TMS320F28335 DSP kit. The sampling and PWM switching frequencies are set at 2 kHz.

6.2 Summary of Important Findings

Chapter 2 proposes a simple predictor-corrector based rotor slip position estimator. This PCSPE algorithm is based on the estimation of stator flux and measured speed. The main conclusions of the work, in this chapter, are as follows:

- For the stable operation of the PCSPE algorithm, a permissible range of the gain is designed. The stability analysis for the proposed observer is done to set the feasible gains.
- A DFIG system is modeled in PSCAD to evaluate the dynamic performance of the proposed observer. From the simulation results, it is observed that the proposed estimator shows a good dynamic response within $\pm 30\%$ of the synchronous speed range. Further, the proposed estimator shows stable performance under a sudden variation of speed reference and load variation of the machine.
- The performance of the proposed estimator is also verified on the developed laboratory-scale experimental setup of DFIG. The results were satisfactory.
- The performance of the scheme is limited by the estimation of flux, which is affected by integral

drift.

In Chapter 3, a new two stage adaptive slip position estimator for a standalone variable speed DFIG system is presented. This estimator requires a minimal number of machine parameters. The main conclusions of this proposed work are as follows:

- The proposed ASSPE includes stator leakage inductance and turns ratio, which improves the estimation accuracy.
- This ASSPE does not depend on the estimation of the stator or rotor flux. This makes the algorithm immune to integral drift. The algorithm is suitable for the variable speed operation of the DFIG.
- Stability of convergence of the algorithm has been analyzed.
- It is observed from the simulation and hardware results that the performance and accuracy of the proposed ASSPE is better than the flux-based estimator discussed in Chapter 2.

In Chapter 4, a new robust two-stage observer is proposed to eliminate the effects of sudden changes in speed and load, parametric uncertainty, and noise. The main conclusions are summarized as:

- In this work, a new estimation scheme is proposed to estimate the slip position and speed of a standalone DFIG system. The proposed estimator has two stages. In both the stages, the effects of noise parameter uncertainties and change in operating point are modeled using disturbance signal. Robustness is achieved by limiting the H_∞ gain of these signals.
- The observer gain values are obtained by solving LMIs. For the second stage, the gain values are selected such that the observer system is passive.
- The tuning procedure of the gain values for the proposed estimator is also provided in this Chapter.
- The working of the proposed observer is simulated in PSCAD to validate its performance. It is observed that the estimator shows good performances under different operating conditions.

The effectiveness of the proposed observer has been verified on a laboratory test bench with a 2.2 kW standalone DFIG system, and compared with the model-based adaptive scheme. In both cases, the proposed estimator provides an accurate estimate of the slip position and speed of the rotor, which is robust to load disturbance and speed changes. The performance of this scheme is found to be superior to that of the model-based adaptive scheme.

Chapter 5 has proposed an Extended Kalman Filter based rotor speed and position estimator using an augmented state model. The main conclusions of the work are as follows:

- An EKF has been designed for three different statespace model: (a) without integral states (non-augmented state model) (b) with integral of stator and rotor current (partially augmented state model), and (c) with integral of stator and rotor current and integral of square of the stator and rotor currents (augmented state model). A comparative analysis is done for these models.
- The performance of the estimators have been analyzed under various dynamic conditions, such as a sudden change in speed, load, turbine torque, and short circuit of the stator terminals.
- From the simulation results, it is seen that the augmented state model showed the best performance as compared to the non-augmented state model and partially augmented state model.
- This algorithm is useful for estimating all states of the grid-connected DFIG system.

6.3 Scope of Future Research Work

In this thesis, the design and development of different types of slip position and speed estimation algorithm for the standalone DFIG system are discussed. The work done in this thesis can be extended along with the following lines:

- The present work is focused on developing the observers. The work can be extended by developing the controllers based on these observers.
- The present work proposes an EKF based state estimation, which uses augmented state models. The proposed algorithm is validated through simulation study. The work can be extended by evaluating its performance through real-time implementation.

- The present work can be extended for developing a robust controller, which can work efficiently during grid disturbances.
- Further, the impact of harmonics on developing the controllers could be studied.







Power Circuit Components and Specifications

Contents

A.1	Specification of Slip Ring Induction Machine	110
A.2	DFIG Parameters	110
A.3	Power Converters	110
A.4	Sensors and Signal Conditioning	111
A.5	Microcontroller:	111
A.6	Grid Filter:	112
A.7	DC Motor:	112
A.8	Starting Procedure for PSCAD/EMTDC Software Based Developed DFIG System	112
A.9	Starting Procedure for Laboratory Based Developed DFIG System	112
A.10	Experimental Setup	114

APPENDIX A

A.1 Specification of Slip Ring Induction Machine

Machine specification: 3-phase, 3 Hp, 415 V, 4 pole 50 Hz.

Make: BENN Electricals

Stator: 415 V Y-connected 4.7 A.

Rotor: 200 V Y-connected 7.8 A.

A.2 DFIG Parameters

The DFIG parameters are given in Table A.1.

Table A.1

Stator Voltage	415 V
Stator Current	4.7 A
Rotor Voltage	200 V
Rotor Current	7.8 A
Number of poles	4
R_s	10.26 Ω
R_r	1.46 Ω
L_s	10.11 mH
L_r	10.11 mH
L_m	365.0 mH

A.3 Power Converters

A.3.1 Power Device:

IPM (IGBT based)

Specifications: 1200 V 25 A

Make: Mitsubishi

A.3.2 Driver:

Optocoupler

Specifications: HCPL4503, High speed: 1 Mb/s

Make: Broadcom

A.3.3 DC-link Capacitor:

5 X 470 μ F, Electrolytic, 450 V

1 X 0.47 μ F 2500 V, Snubber capacitor.

A.4 Sensors and Signal Conditioning

A.4.1 Current Sensor:

LA55P

Specification: Hall effect, Closed loop 50 A, 100 kHz bandwidth

Make: LEM

A.4.2 Voltage Sensor:

LV25P

Specification: Hall effect, Closed loop 500 V, 100 kHz bandwidth

Make: LEM

A.4.3 Signal Conditioning & Sensor Interface Circuit:

TL084 Opamp based

Input: ± 3.3 V

output: 0-3.3 V range

Specification: Wide Common-Mode and Differential voltage ranges High Slew Rate(13 V/ μ s Typical) Output Short-Circuit Protection

Make: Texas Instruments

A.5 Microcontroller:

DSP processor: TMS320F28335

Specification: Floating point, 32-bit, 150 MHz

Make: Texas Instruments

A.6 Grid Filter:

3 X 10 mH, 15 A, Iron core

A.7 DC Motor:

Separately excited DC motor

3 hp, 220 V, 15 A, 1500 RPM

Field: 220 V, 1 A

A.8 Starting Procedure for PSCAD/EMTDC Software Based Developed DFIG System

In simulation, the machine runs at the speed control mode for a given speed reference. Initially, the rotor side converter is in off-mode until machine reaches to the reference speed. Then, the DC bus switch is ON to charge the DC-link capacitor. At time $t = 3.5$ s, the RSC is turned on with a fixed

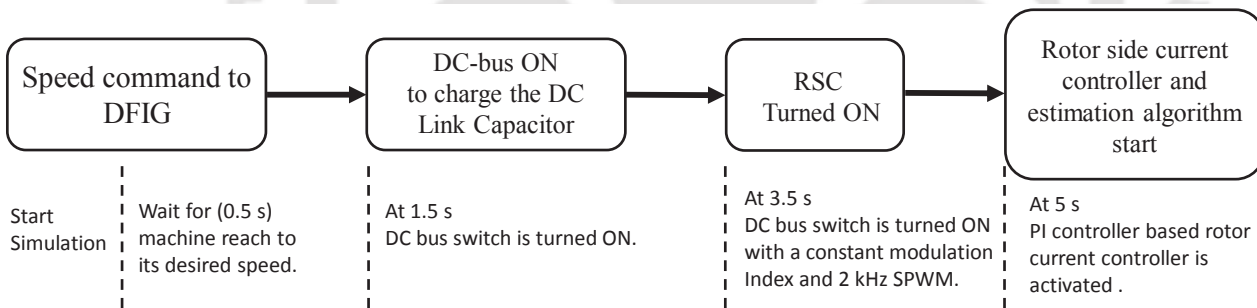


Figure A.1: Starting procedure of the DFIG system (simulation) for estimator algorithm testing.

modulation index, $m_{dr}^* = -0.25$ and $m_{qr}^* = 0$. At $t = 5.0$ s, the rotor current controller is turned on along with the proposed estimator to control the rotor side converter for achieving the desired stator voltage. Figure A.1 shows the starting procedure of the DFIG system in PSCAD software for testing of the estimator algorithm.

A.9 Starting Procedure for Laboratory Based Developed DFIG System

A laboratory based hardware setup for DFIG system is developed. Figure A.2 shows the starting sequence of the DFIG system in the laboratory. In practice, the following steps are required to start

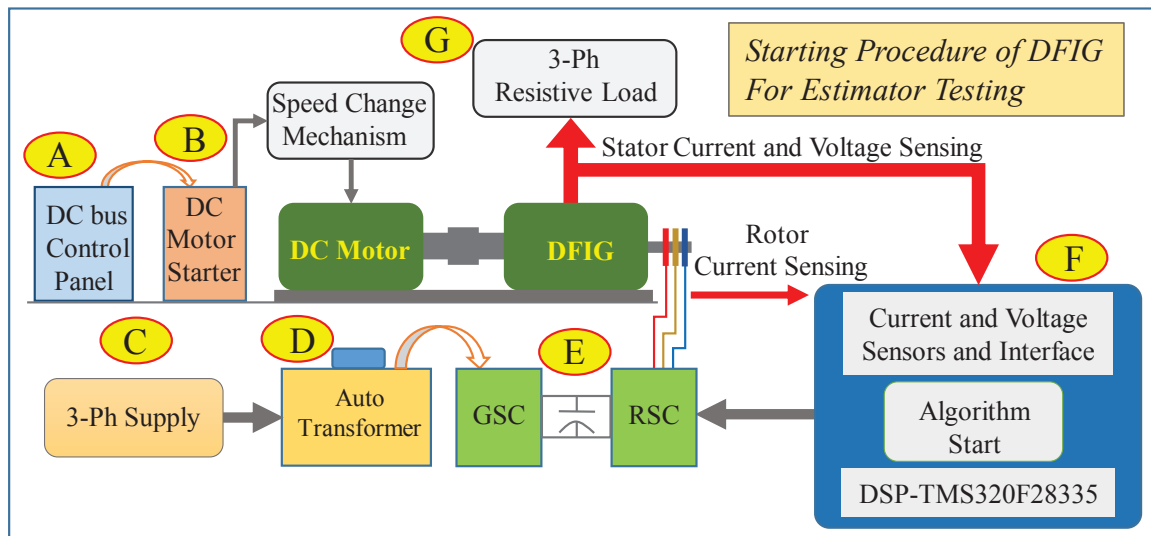


Figure A.2: Starting procedure of the DFIG system (hardware) for estimator algorithm testing.

the standalone DFIG setup for estimation algorithm testing,

- A. Initially turn on the DC bus control and slowly increase the dc voltage up to 185V, which provides the DC power supply for the DC motor starting.
- B. To avoid large starting current, the DC motor is started by using a 3-point starter. The rotor side and grid side converters are in off-mode till the shaft speed reaches at reference sub-synchronous speed range (1400 RPM).
- C. Once the machine reaches desired sub-synchronous speed range, a 3-Phase supply mains is turned on which is connected to the input side of the auto-transformer.
- D. Then, the auto-transformer is turned on and supply is given to the input of GSC which acts as a 3-Phase rectifier is used to convert AC to DC for charging the DC-link capacitor.
- E. At the input of rotor side inverter, the voltage is slowly increased to apply the DC link voltage at the RSC input.
- F. Initialize the control power supply (5V, 15V DC) for the gate driver circuit and sensor interface circuits to execute the proposed estimation algorithm. In hardware setup, a waiting time of 120 s is introduced to settle the SRFPLL at start, which gives the θ_s and ω_s at 50Hz. After 120 s,

A. Power Circuit Components and Specifications

the estimator algorithm is started to estimate the rotor slip position and speed of the machine with a fixed modulation index (m_{dr}^* and m_{qr}^*).

- G. Once the machine successfully runs at a constant speed (sub-synchronous), a test load is changed to validate the algorithm performance and robustness. A speed change mechanism is implemented to emulate the speed variation of the prime mover. The speed change mechanism mainly works based on the variation of applied voltage in the DC motor terminal.

A.10 Experimental Setup

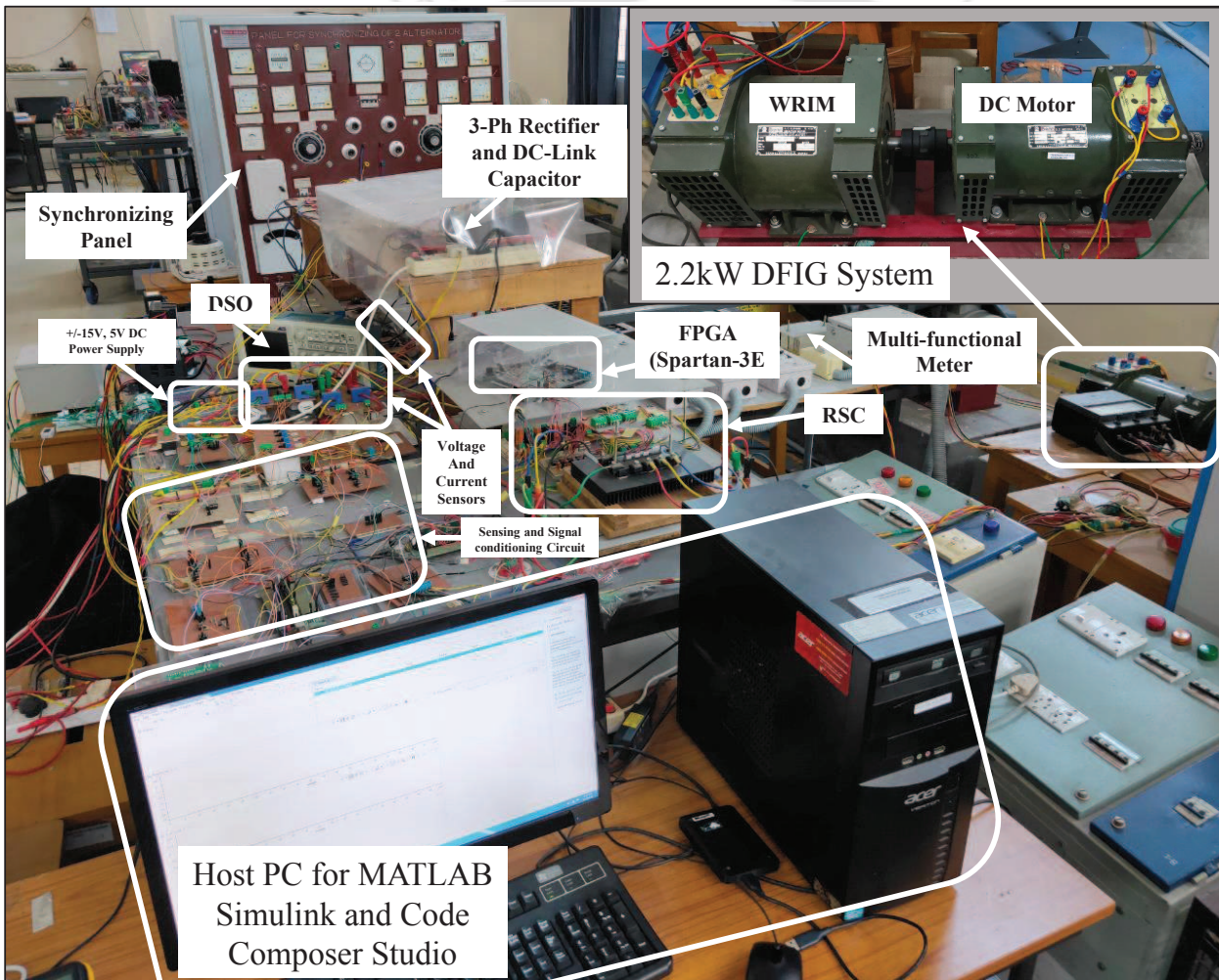


Figure A.3: Experimental setup.

B

DFIG Model in Different Reference Frame

Contents

B.1	Reference Frame Transformation	116
B.2	Synchronous Reference Frame Phase Locked Loop (SRFPLL)	120
B.3	DFIG Model in $\alpha\text{-}\beta$ Reference Frame	121
B.4	DFIG Model in $d - q$ Reference Frame	123
B.5	Design of Low Pass Filter as an integrator	124

APPENDIX B

B.1 Reference Frame Transformation

The dynamic model of the DFIG is needed for dynamic analysis and control system design. The DFIG is a time varying high order non linear system. In order to derive the DFIG model, following assumptions are introduced:

- Three phase coils (120° phase shift between each other in space), both on the stator and rotor of the machine are symmetrical and balanced.
- The magnetic saturation and iron loss of the stator and rotor core are neglected.
- The resistance of both stator and rotor windings are unchanged with the temperature and frequency variations.

With the above assumptions and generalized machine theory, the DFIG model can be represented as three static stator coils and three rotor coils rotating with angular frequency ω_r , as depicted in figure

B.1

The 3 phase stator currents are given by the following space vector notation,

$$I_{As} = I_{sm} \sin \theta_s \quad (\text{B.1})$$

$$I_{Bs} = I_{sm} \sin \left(\theta_s - \frac{2\pi}{3} \right) \quad (\text{B.2})$$

$$I_{Cs} = I_{sm} \sin \left(\theta_s + \frac{2\pi}{3} \right) \quad (\text{B.3})$$

The 3 phase rotor currents are given by the following space vector notation,

$$I_{Ar} = I_{rm} \sin \theta_{sl} \quad (\text{B.4})$$

$$I_{Br} = I_{rm} \sin \left(\theta_{sl} - \frac{2\pi}{3} \right) \quad (\text{B.5})$$

$$I_{Cr} = I_{rm} \sin \left(\theta_{sl} + \frac{2\pi}{3} \right) \quad (\text{B.6})$$

where, I_{sm} = peak magnitude of the stator phase current and I_{rm} = peak magnitude of the rotor phase current.

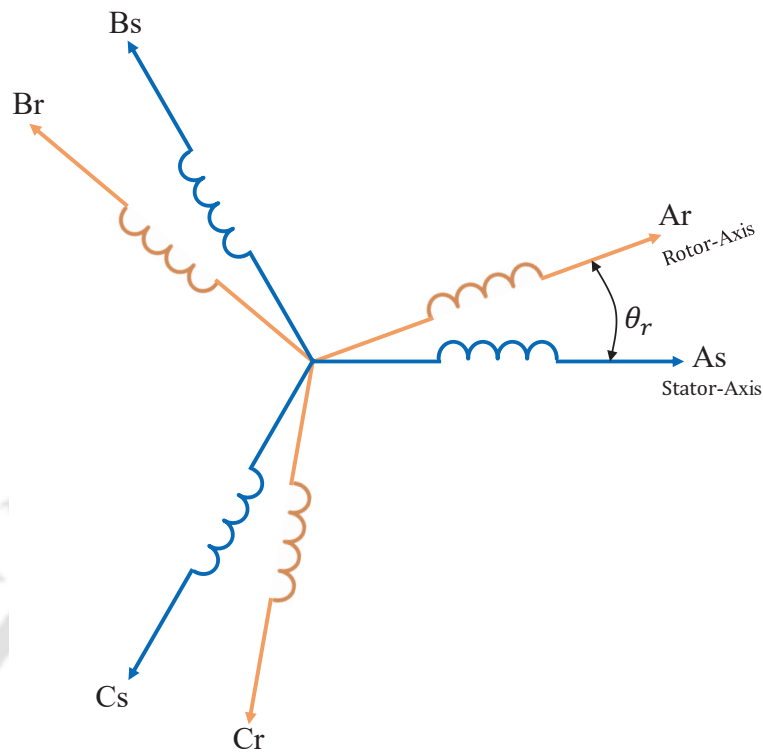


Figure B.1: Three phase stator and rotor coils of the DFIG.

The superscript notation is used to denote the space vector in reference to one specific reference frame. The notation for the three different frames are introduced in the following,

- Stator Reference Frame ($\alpha\text{-}\beta$): The rotational speed of the reference frame is zero (stationary) as it is aligned with stator. The space vector rotates at synchronous speed ω_s with respect to it.

The stator current I_s and stator voltage V_s representation in $\alpha\text{-}\beta$ frame is given by

$$I_s = i_{\alpha s} + j i_{\beta s} \quad (\text{B.7})$$

$$V_s = V_{\alpha s} + j V_{\beta s}. \quad (\text{B.8})$$

- Rotor Reference Frame ($a\text{-}b$): The rotating speed of the reference frame is equal to electric speed of the rotor, since it is aligned with the rotor. The space vector rotates at slip speed ω_{slip} referred to it. The rotor current I_r representation in $a\text{-}b$ frame is given by

$$I_r = i_{ar} + j i_{br}. \quad (\text{B.9})$$

B. DFIG Model in Different Reference Frame

The transformation of rotor current to α - β reference frame is given by

$$[I_r]^{\alpha\beta} = \{i_{ar} + ji_{br}\}e^{-j\theta_r}. \quad (\text{B.10})$$

- Synchronous reference frame ($d - q$): The reference frame rotates at synchronous speed ω_s . The space vector is stationary with respect to it.

$$[I_s]^{dq} = I_s e^{j\theta_s} \quad (\text{B.11})$$

$$[V_s]^{dq} = V_s e^{j\theta_s} \quad (\text{B.12})$$

$$[I_r]^{dq} = \{i_{ar} + ji_{br}\}e^{j(\theta_s - \theta_r)} = I_r e^{j\theta_{sl}}. \quad (\text{B.13})$$

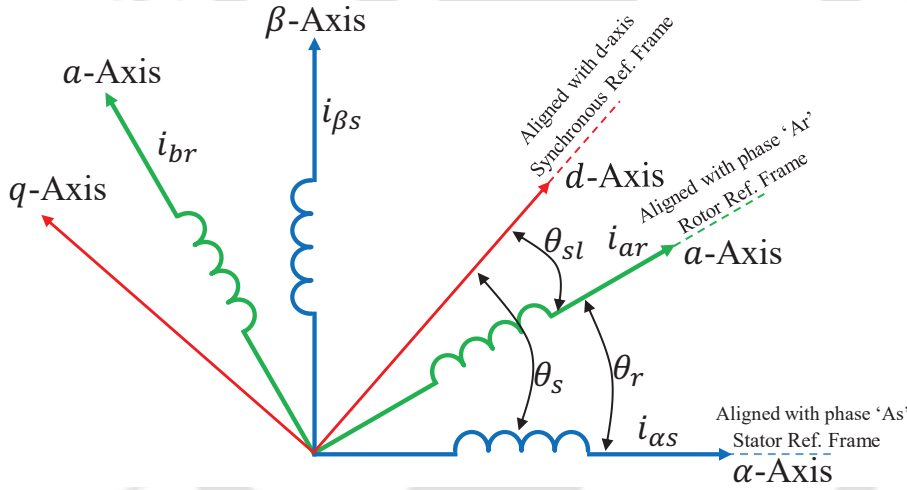


Figure B.2: Space vector representation of the reference frames.

The transformation matrix for 3 phase rotor current in rotor reference frame (ab) and stator stationary reference ($\alpha\beta$) frame are as follows

$$\begin{bmatrix} i_{ar} \\ i_{br} \end{bmatrix} = \begin{bmatrix} 1 & -\frac{1}{2} & -\frac{1}{2} \\ 0 & \frac{\sqrt{3}}{2} & -\frac{\sqrt{3}}{2} \end{bmatrix} \begin{bmatrix} i_{Ar} \\ i_{Br} \\ i_{Cr} \end{bmatrix} \quad (\text{B.14})$$

$$\begin{bmatrix} i_{ar} \\ i_{br} \end{bmatrix} = \begin{bmatrix} \cos(\theta_r) & \sin(\theta_r) \\ -\sin(\theta_r) & \cos(\theta_r) \end{bmatrix} \begin{bmatrix} i_{ar} \\ i_{br} \end{bmatrix} \quad (\text{B.15})$$

The rotor current in synchronous (dq) reference frame is given by

$$\begin{bmatrix} i_{dr} \\ i_{qr} \end{bmatrix} = \begin{bmatrix} \cos(\theta_s) & \sin(\theta_s) \\ -\sin(\theta_s) & \cos(\theta_s) \end{bmatrix} \begin{bmatrix} i_{ar} \\ i_{br} \end{bmatrix} \quad (\text{B.16})$$

In order to transform rotor current from dq reference frame to ab reference frame, the inverse rotational transformation is used. The transformation is given as follows,

$$\begin{bmatrix} i_{ar} \\ i_{br} \end{bmatrix} = \begin{bmatrix} \cos(\theta_{sl}) & -\sin(\theta_{sl}) \\ \sin(\theta_{sl}) & \cos(\theta_{sl}) \end{bmatrix} \begin{bmatrix} i_{dr} \\ i_{qr} \end{bmatrix} \quad (\text{B.17})$$

The 3-phase stator voltage and current are transformed into stator stationary ($\alpha\beta$) frame using the given transformation matrix,

$$\mathbf{T} = \begin{bmatrix} 1 & -\frac{1}{2} & -\frac{1}{2} \\ 0 & \frac{\sqrt{3}}{2} & -\frac{\sqrt{3}}{2} \end{bmatrix} \quad (\text{B.18})$$

The stator voltage and current in $\alpha\beta$ reference frame are given by the following equations,

$$\begin{bmatrix} i_{\alpha s} \\ i_{\beta s} \end{bmatrix} = \mathbf{T} \begin{bmatrix} I_{As} \\ I_{Bs} \\ I_{Cs} \end{bmatrix} \quad (\text{B.19})$$

$$\begin{bmatrix} V_{\alpha s} \\ V_{\beta s} \end{bmatrix} = \mathbf{T} \begin{bmatrix} V_{As} \\ V_{Bs} \\ V_{Cs} \end{bmatrix} \quad (\text{B.20})$$

The transformation of stator voltage and current to dq reference frame from $\alpha\beta$ frame are given by,

$$\begin{bmatrix} i_{ds} \\ i_{qs} \end{bmatrix} = \mathbf{T}(\theta_s) \begin{bmatrix} i_{\alpha s} \\ i_{\beta s} \end{bmatrix} \quad (\text{B.21})$$

$$\begin{bmatrix} V_{ds} \\ V_{qs} \end{bmatrix} = \mathbf{T}(\theta_s) \begin{bmatrix} V_{\alpha s} \\ V_{\beta s} \end{bmatrix} \quad (\text{B.22})$$

where, $T(\theta_s) = \begin{bmatrix} \cos(\theta_s) & \sin(\theta_s) \\ -\sin(\theta_s) & \cos(\theta_s) \end{bmatrix}$.

In order to transform the stator quantities to $\alpha\beta$ frame from dq reference frame, inverse transformation matrix $[T(\theta_s)]^{-1}$ is used. Further, the $\alpha\beta$ frame to 3 phase quantities are calculated using matrix $[T]^{-1}$, known as inverse Clarke transformation. The stator voltage and current transformation equations are as follows,

$$\begin{bmatrix} i_{\alpha s} \\ i_{\beta s} \end{bmatrix} = T(\theta_s) \begin{bmatrix} i_{ds} \\ i_{qs} \end{bmatrix} \quad (\text{B.23})$$

$$\begin{bmatrix} V_{\alpha s} \\ V_{\beta s} \end{bmatrix} = T(\theta_s) \begin{bmatrix} V_{ds} \\ V_{qs} \end{bmatrix} \quad (\text{B.24})$$

where, $[T(\theta_s)]^{-1} = \begin{bmatrix} \cos(\theta_s) & -\sin(\theta_s) \\ \sin(\theta_s) & \cos(\theta_s) \end{bmatrix}$ and $[T]^{-1} = \begin{bmatrix} 1 & 0 \\ -\frac{1}{2} & \frac{\sqrt{3}}{2} \\ -\frac{1}{2} & -\frac{\sqrt{3}}{2} \end{bmatrix}$.

B.2 Synchronous Reference Frame Phase Locked Loop (SRFPLL)

Synchronous reference frame phase locked loop (SRFPLL) works by synchronizing the voltage space vector along d axis. In stand alone operation, the grid voltage space vector is generated as reference to the SRF PLL system for laboratory implementation. In order to achieve synchronization, the following transformation matrix is used.

$$T(\theta_{PLL}) = \begin{bmatrix} \cos(\theta_{PLL}) & \sin(\theta_{PLL}) \\ -\sin(\theta_{PLL}) & \cos(\theta_{PLL}) \end{bmatrix} \quad (\text{B.25})$$

where θ_{PLL} is the estimated phase angle obtained from SRF PLL. The transformed vector components for Voltage vector is obtained as follows

$$\begin{bmatrix} V_{ds} \\ V_{qs} \end{bmatrix} = \begin{bmatrix} V_m \cos(\theta_s - \theta_{PLL}) \\ V_m \sin(\theta_s - \theta_{PLL}) \end{bmatrix}. \quad (\text{B.26})$$

From (B.26), it can be noted that on synchronization, the $\theta_s = \theta_{PLL}$ and stator voltage is aligned with the d -axis of the grid voltage reference. The q component of the stator voltage will be zero. In order to estimate θ_s , the error between θ_s and θ_{PLL} should be minimized through a PI controller. The estimated grid frequency is the summation of the PI-output and the reference frequency ω_{ref} (50 Hz). Figure B.3 shows the structure of the SRFPLL. The gain of the PI controller should be set such that the response has less oscillations and reduced settling time.

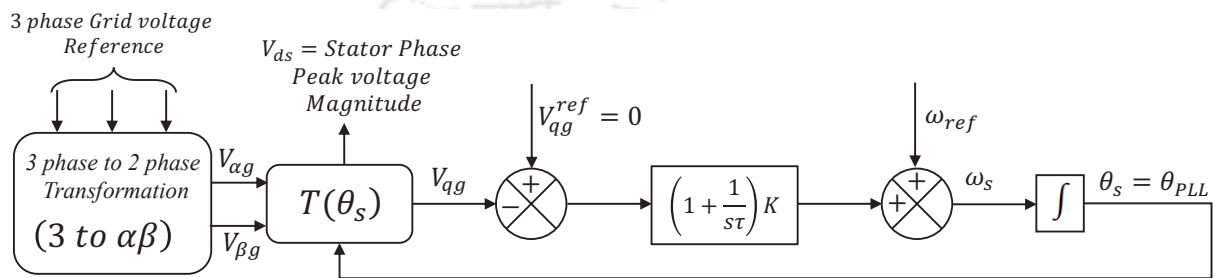


Figure B.3: Structure of SRFPLL

The SRFPLL has been implemented in TMS320F28335 DSP kit for laboratory setup.

B.3 DFIG Model in α - β Reference Frame

The equivalent circuit of the machine in $\alpha\beta$ reference frame is shown in the Figure B.4.

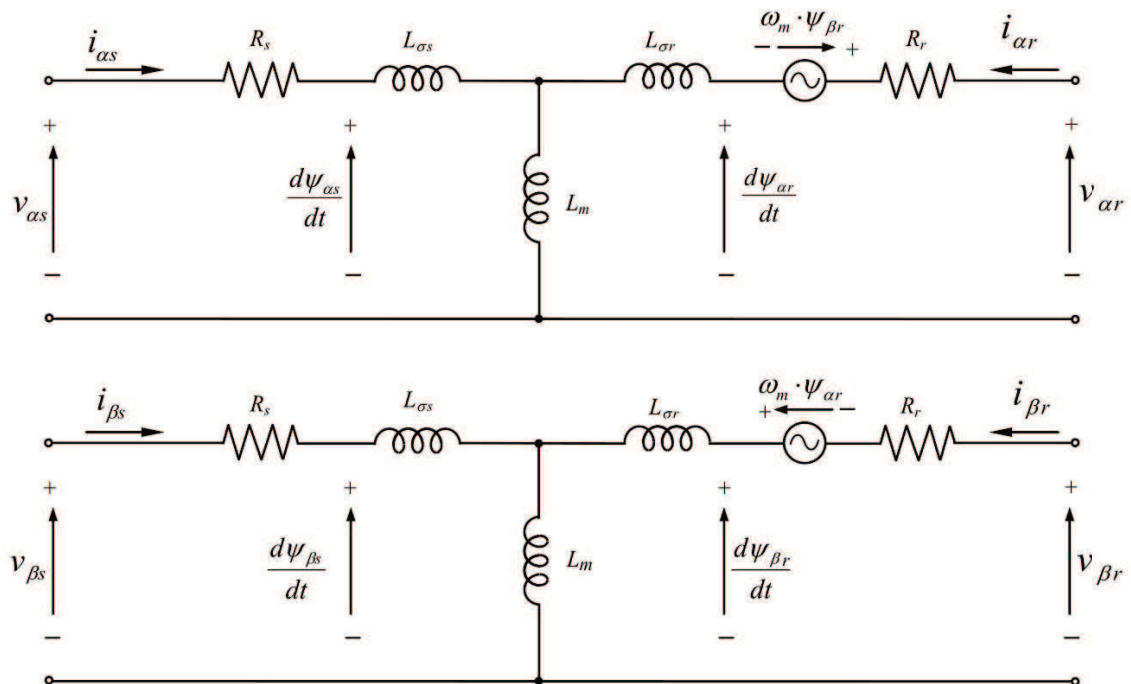


Figure B.4: $\alpha\beta$ Model of the DFIG in stator reference frame.

B. DFIG Model in Different Reference Frame

The mathematical model of the DFIG is developed using the space vector representation in the stator reference frame. The flux is created by the current flow through the mutual magnetizing and leakage inductances. Hence, the stator flux expressions in the stator reference frame are given by

$$\psi_{\alpha s} = L_s i_{\alpha s} + L_m i_{\alpha r} \quad (\text{B.27})$$

$$\psi_{\beta s} = L_s i_{\beta s} + L_m i_{\beta r} \quad (\text{B.28})$$

$$\psi_{\alpha r} = L_r i_{\alpha r} + L_m i_{\alpha s} \quad (\text{B.29})$$

$$\psi_{\beta r} = L_r i_{\beta r} + L_m i_{\beta s} \quad (\text{B.30})$$

where L_s and L_r are the stator and rotor inductances. The magnetizing inductance, stator leakage and rotor leakage inductances are denoted by L_m , L_{ls} and L_{lr} . The relation among all the inductances are given by

$$L_s = L_{ls} + L_m \quad (\text{B.31})$$

$$L_r = L_{lr} + L_m \quad (\text{B.32})$$

The voltage equations for the stator and rotor coils in stator stationary reference frame ($\alpha\beta$) can be written as

$$V_{\alpha s} = R_s i_{\alpha s} + \frac{d\psi_{\alpha s}}{dt} \quad (\text{B.33})$$

$$V_{\beta s} = R_s i_{\beta s} + \frac{d\psi_{\beta s}}{dt} \quad (\text{B.34})$$

$$V_{\alpha r} = R_r i_{\alpha r} + \frac{d\psi_{\alpha r}}{dt} + \omega_r \psi_{\beta r} \quad (\text{B.35})$$

$$V_{\beta r} = R_r i_{\beta r} + \frac{d\psi_{\beta r}}{dt} - \omega_r \psi_{\alpha r} \quad (\text{B.36})$$

where R_s is the stator resistance and R_r is the rotor resistance. Combining equations (B.27) to (B.36),

the statespace model of the machine can be written as

$$\frac{di_{\alpha s}}{dt} = \frac{1}{\sigma L_s L_r} (-R_s L_r i_{\alpha s} + \omega_r L_m^2 i_{\beta s} + R_r L_m i_{\alpha r} + \omega_r L_m L_r i_{\beta r} + L_r V_{\alpha s} - L_m V_{\alpha r}) \quad (\text{B.37})$$

$$\frac{di_{\beta s}}{dt} = \frac{1}{\sigma L_s L_r} (-\omega_r L_m^2 i_{\alpha s} - R_s L_r i_{\beta s} - \omega_r L_m L_r i_{\alpha r} + R_r L_m i_{\beta r} + L_r V_{\beta s} - L_m V_{\beta r}) \quad (\text{B.38})$$

$$\frac{di_{\alpha r}}{dt} = \frac{1}{\sigma L_s L_r} (R_s L_m i_{\alpha s} - \omega_r L_s L_m i_{\beta s} - R_r L_s i_{\alpha r} - \omega_r L_s L_r i_{\beta r} - L_m V_{\alpha s} + L_s V_{\alpha r}) \quad (\text{B.39})$$

$$\frac{di_{\beta r}}{dt} = \frac{1}{\sigma L_s L_r} (\omega_r L_s L_m i_{\alpha s} + R_s L_m i_{\beta s} + \omega_r L_s L_r i_{\alpha r} - R_r L_s i_{\beta r} - L_m V_{\beta s} + L_s V_{\beta r}), \quad (\text{B.40})$$

where leakage factor, $\sigma = 1 - \frac{L_m^2}{L_s L_r}$. The electromagnetic torque and the mechanical motion are given

by

$$T_e = \frac{3P}{2} L_m (i_{\alpha r} i_{\beta s} - i_{\alpha s} i_{\beta r}) \quad (\text{B.41})$$

$$\frac{d\omega_r}{dt} = \frac{P}{2J} (T_e - T_l) \text{ neglecting frictional loss} \quad (\text{B.42})$$

Equations (B.37)-(B.42) have been used to obtain the dynamic model of the DFIG. The active and reactive powers on the stator side and rotor side are given as follows

$$P_s = \frac{3}{2} (V_{\alpha s} i_{\alpha s} + V_{\beta s} i_{\beta s}) \quad (\text{B.43})$$

$$P_r = \frac{3}{2} (V_{\alpha r} i_{\alpha r} + V_{\beta r} i_{\beta r}) \quad (\text{B.44})$$

$$Q_s = \frac{3}{2} (V_{\beta s} i_{\alpha s} - V_{\alpha s} i_{\beta s}) \quad (\text{B.45})$$

$$Q_r = \frac{3}{2} (V_{\beta r} i_{\alpha r} - V_{\alpha r} i_{\beta r}). \quad (\text{B.46})$$

B.4 DFIG Model in $d - q$ Reference Frame

The mathematical model of the DFIG in dq reference frame can be derived using transformation matrix given above. The dynamic equation of a DFIG machine can be described by the following set

B. DFIG Model in Different Reference Frame

of equations in a synchronously rotating reference frame.

$$V_{ds} = R_s i_{ds} + \frac{d\psi_{ds}}{dt} - \omega_s \psi_{qs} \quad (\text{B.47})$$

$$V_{qs} = R_s i_{qs} + \frac{d\psi_{qs}}{dt} + \omega_s \psi_{ds} \quad (\text{B.48})$$

$$V_{dr} = R_r i_{dr} + \frac{d\psi_{dr}}{dt} - (\omega_s - \omega_r) \psi_{qr} \quad (\text{B.49})$$

$$V_{qr} = R_r i_{qr} + \frac{d\psi_{qr}}{dt} + (\omega_s - \omega_r) \psi_{dr} \quad (\text{B.50})$$

The electromagnetic torque is given by

$$T_e = \frac{3}{2} p (\psi_{ds} i_{qs} - \psi_{qs} i_{ds}) \quad (\text{B.51})$$

$$\psi_{ds} = L_s i_{ds} + L_m i_{dr} \quad (\text{B.52})$$

$$\psi_{qs} = L_s i_{qs} + L_m i_{qr} \quad (\text{B.53})$$

$$\psi_{dr} = L_r i_{dr} + L_m i_{ds} \quad (\text{B.54})$$

$$\psi_{qr} = L_r i_{qr} + L_m i_{qs} \quad (\text{B.55})$$

where the stator and rotor voltages are presented in (B.47)-(B.50). From (B.52)-(B.55) describe the flux-linkage of the machine.

B.5 Design of Low Pass Filter as an integrator

A low pass filter is used as an integrator instead of the pure integrator. The low pass filter compensates for the phase magnitude and the phase shift of the stator flux estimation. This compensation depends on the frequency of the stator flux (50Hz). The transfer function of the pure integrator and

low pass filter are as follows,

$$G_i(S) = \frac{1}{S} \quad (\text{B.56})$$

$$G_{lp}(S) = \frac{1}{S + \omega_c} \quad (\text{B.57})$$

Since grid frequency is constant, it is possible to calculate the magnitude and phase angle deviations:

$$\left. \begin{aligned} |G_i(j\omega)| &= \frac{1}{\omega} \\ |G_{lp}(j\omega)| &= \frac{1}{\sqrt{\omega^2 + \omega_c^2}} \end{aligned} \right\}, \quad \left. \begin{aligned} \angle G_i(j\omega) &= -90^\circ \\ \angle G_{lp}(j\omega) &= -\arctan \frac{\omega}{\omega_c} \end{aligned} \right\}$$

From this above, the phase magnitude (P_{mag}) and phase angle deviation (P_{ang}) can be calculated

$$\frac{|G_i(j\omega)|}{|G_{lp}(j\omega)|} = \sqrt{\frac{\omega^2 + \omega_c^2}{\omega^2}} = \sqrt{1 + \frac{\omega_c^2}{\omega^2}} = P_{mag}$$

and

$$\angle G_i(j\omega) - \angle G_{lp}(j\omega) = -90^\circ + \arctan \frac{\omega}{\omega_c} = P_{ang}$$

The estimation of stator flux using Low Pass Filter is shown in figure B.5.

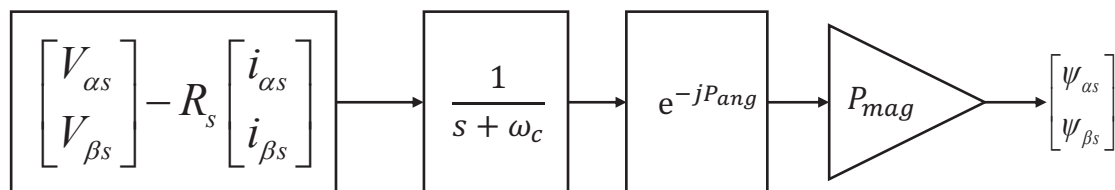
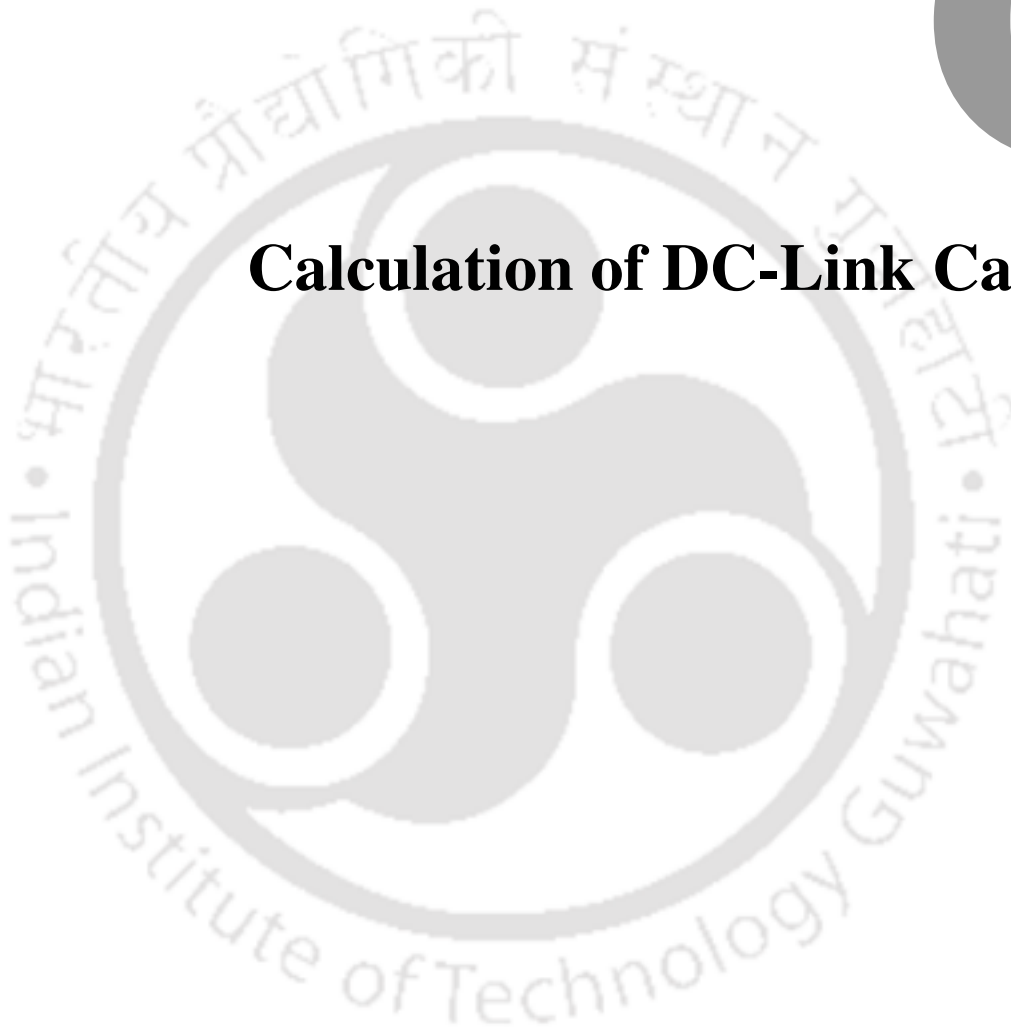


Figure B.5: Stator flux estimation using Low Pass Filter



C

Calculation of DC-Link Capacitor



Contents

C.1 Calculation of DC-link Capacitor	128
--	-----

APPENDIX C

C.1 Calculation of DC-link Capacitor

The required amount of reactive power drawn by the DFIG is supplied by the DC link capacitor. The DC-link capacitor is used to balance the instantaneous power difference between the input source and output load, and minimize the voltage ripple in the DC link. The size of the DC link capacitor determines the magnitude of the voltage switching ripple.

The instantaneous inverter input current can be expressed as

$$i(t) = I_{dc} + \Delta i(t) + \text{low frequency component} \quad (\text{C.1})$$

where I_{dc} is the dc current which flows through the inverter. The ripple current $\Delta i(t)$ is bypassed through the DC link capacitor. The low frequency component is zero for the balanced load condition. Neglecting the inverter's losses and considering the input-output power balance, the DC current can be written as

$$I_{dc} = \frac{3}{2} m I_p \cos \phi. \quad (\text{C.2})$$

The ripple current can be calculated as

$$\Delta i(t) = i(t) - \frac{3}{2} m I_p \cos \phi. \quad (\text{C.3})$$

The voltage ripple can be determined by integrating the $\Delta i(t)$ over the switching time interval, T_{sw} . Considering $\Delta i(t)$ constant within the specific time interval, the simplified switching voltage ripple expression is given by

$$\Delta v_{pp} = \frac{1}{C} \int_0^{T_{sw}} \Delta i(t) dt = \frac{1}{C} \Delta I T_{sw}. \quad (\text{C.4})$$

In order to trade off between the capacitor size and the switching voltage ripple, the allowable maximum voltage ripple is 0.125 for a grid connected inverter application. For the unity powerfactor, the voltage ripple can be written as

$$\Delta v_{pp} = \frac{1}{8} \frac{1}{C f_{sw}}. \quad (\text{C.5})$$

The value of the capacitor should be estimated for the maximum reactive power drawn by the load at the rated frequency. The condition for the calculated capacitor value is given by

$$C \geq \frac{1}{8 C f_{sw} \Delta v_{pp}}. \quad (C.6)$$

The rms value of the ripple current can be derived as

$$I_{rip} = \frac{I_p}{\sqrt{3}}. \quad (C.7)$$





D

Nonlinear Variable Speed Variable Pitch Wind Turbine System

Contents

D.1 Nonlinear Variable Speed Variable Pitch Wind Turbine System	132
--	------------

APPENDIX D

D.1 Nonlinear Variable Speed Variable Pitch Wind Turbine System

Variable pitch wind turbine [64] is used to extract more wind energy within the wide range of wind speed. Aerodynamic blade pitch angle β is continuously controlled to regulate the turbine rotor speed ω_t as well as captured wind energy. The mechanical power P_{mech} produced by the wind turbine is defined as

$$P_{mech} = T_t \omega_t \quad (D.1)$$

$$T_t = \frac{1}{2} \rho A R^3 \frac{C_p(\lambda, \beta)}{\lambda^3} \omega_t^2, \quad (D.2)$$

Where $T_t, A, C_p(\lambda, \beta)$ and ρ is the turbine aerodynamic torque, rotor swept area, power coefficient for a variable pitch wind turbine and air density, respectively. The tip speed ratio, $\lambda = \frac{R\omega_t}{\vartheta}$ where R and ϑ stands for turbine rotor radius and wind speed respectively. Using blade element momentum (BEM) [64, 65] theory the pitch angle dynamics can be derived as

$$\dot{\beta} = K_1(\omega_t - \omega_r) \left(1 - \frac{\beta}{K_2}\right) \quad (D.3)$$

The turbine rotor position can be expressed by δ and the dynamic model [64] of variable pitch variable speed wind turbine can be written as

$$\dot{\delta} = \omega_t \quad (D.4)$$

$$\dot{\omega}_t = \frac{1}{J} [-K_r \delta - B_r \omega_t + T_t - T_e] \quad (D.5)$$

$$\dot{\beta} = K_1(\omega_t - \omega_r) \left(1 - \frac{\beta}{K_2}\right) \quad (D.6)$$

where K_r, B_r, J and T_e is the rotor shaft torsion, rotor shaft friction, rotor inertia and electromagnetic torque respectively. K_1 and K_2 is integration constant and the gain reduction constant that reduces the pitch rate at high pitch angles, respectively. The parameters are not precisely known and depending on several factors such as aerodynamic conditions, in addition introduces uncertainty in the nonlinear wind turbine dynamics [66, 67].

Bibliography

- [1] www.gwec.net, 2012.
- [2] *Electrical India*, 2012.
- [3] G. J. Herbert, S. Iniyar, E. Sreevalsan, and S. Rajapandian, "A review of wind energy technologies," *Renewable and Sustainable Energy Reviews*, vol. 11, no. 6, pp. 1117 – 1145, 2007.
- [4] M. Tazil and V. Kumar et.al, "Three-phase doubly fed induction generators: an overview," *IET Electric Power Appl.*, vol. 4, pp. 75–89, 2010.
- [5] Boldia, *Variable Speed Generators: the electrical hand book*. Taylor and francis, New York, USA, 2006.
- [6] B. A. Chen, T. K. Lu, Y. Y. Hsu, W. L. Chen, and Z. C. Lee, "An analytical approach to maximum power tracking and loss minimization of a doubly fed induction generator considering core loss," *IEEE Trans. Energy Convers.*, vol. 27, no. 2, pp. 449 –456, june 2012.
- [7] J. Hu, H. Nian, B. Hu, Y. He, and Z. Q. Zhu, "Direct active and reactive power regulation of dfig using sliding-mode control approach," *IEEE Trans. Energy Convers.*, vol. 25, no. 4, pp. 1028 –1039, dec. 2010.
- [8] T. Sun, Z. Chen, and F. Blaabjerg, "Flicker study on variable speed wind turbines with doubly fed induction generator," *IEEE Trans. Power Electron.*, vol. 26, no. 1, pp. 896–905, 2011.
- [9] Daniel G. Forchetti, Guillermo O. G, and Maria Ines Valla, "Adaptive observer for sensorless control of stand-alone doubly fed induction generator," *IEEE Trans. Ind. Electron.*, vol. 56, no. 10, pp. 4174 – 4180, Oct 2009.
- [10] W. Leonard, *Control of Electrical Drives*. Springer, New York, USA, 1985.
- [11] P. Vas, *Sensorless Vector and Direct Torque Control*. Oxford University Press, 1998.
- [12] M. Yamamoto and O. Motoyoshi, "Active-reactive power control for doubly fed wound rotor induction generator," *IEEE Trans. Power Electron.*, vol. 6, no. 4, pp. 624–629, 1991.
- [13] N. Mohan, T. M. Undeland, and W. P. Robbins, "*Power Electronics: Converters, Applications and Design*". Clarendon Press, Oxford, UK, 1989.
- [14] R. Pena, J. C. Clare, and G. M. Asher, "Doubly fed induction generator using back-to-back pwm converters and its application to variable-speed wind-energy generation," *IEEE Proc. Elect. Power Appl.*, vol. 143, pp. 231–241, 1996.
- [15] Datta R. and Ranganathan V.T., "A simple position sensorless algorithm for rotor side field oriented control of wound rotor induction machine," *IEEE Trans. Ind. Electron.*, vol. 48, no. 4, pp. 710–718, 2001.
- [16] R. Cardenas, R. Pena, G. Asher, J. Clare, and J. Cartes, "Mras observer for doubly fed induction machines," *IEEE Trans. Energy Convers.*, vol. 19, no. 2, pp. 467–468, 2004.

BIBLIOGRAPHY

- [17] L. Xu and W. Cheng, "Torque and reactive power control of a doubly fed induction machine by position sensorless scheme," *IEEE Trans. Ind. Appl.*, vol. 31, no. 3, pp. 636–641, 1995.
- [18] L. Morel, H. Godfroid, A. Mirzaian, and J.M. Kauffmann, "Doubly fed induction machine: converter optimization and field orientated control without position sensor," *Proc. Inst. Electr. Eng. Electr. Power Appl.*, vol. 145, no. 4, pp. 360–368, 1998.
- [19] B. Hopfensperger, D. J. Atkinson, and R. A. Lakin, "Stator-flux oriented control of a doubly-fed induction machine with and without position encoder," *Proc. Inst. Electr. Eng. Electr. Power Appl.*, vol. 147, no. 4, pp. 241–250, 2000.
- [20] M. Abolhassani, P. Enjeti, and H. Toliyat, "Intregrated doubly fed elctric alternator/active filter (idea), a variable power quality solution, for wind energy conversion system," *IEEE Trans. Energy Convers.*, vol. 23, no. 2, pp. 642–650, 2008.
- [21] Sheng Y. and Venkataramana A., "A speed-adaptive reduced-order observer for sensorless vector control of doubly fed induction generator-based variable speed wind turbine," *IEEE Trans. Energy Convers.*, vol. 25, no. 3, 2010.
- [22] J. Lopez, Sanchis P., Roboam X., and Marroyo L., "Dynamic behaviour of the doubly fed induction generator during three phase voltage dips," *IEEE Trans. Energy Convers.*, vol. 22, pp. 709–717, 2007.
- [23] A. Mullane, Lightbody G., and Yacamini R., "Wind-turbine fault ride-through enhancement," *IEEE Trans. Power Syst.*, vol. 20, pp. 1929–1937, 2005.
- [24] O. Abdel Baqi and A. Nasiri, "A dynamic lvrvt solution for doubly fed induction generators," *IEEE Trans. Power Electron.*, vol. 25, no. 1, pp. 193–196, Jan 2010.
- [25] Z. Wang, Y. Sun, G. Li, and B. T. Ooi, "Magnetude and frequency control of grid connected doubly fed induction generator based on synchronised model for wind power generation," *IET Renewable Power Generation*, vol. 4, no. 3, pp. 232–241, may 2010.
- [26] L. Xu and Y. Wang, "Dynamic modeling and control of dfig-based wind turbines under unbalanced network conditions," *IEEE Trans. Power Syst.*, vol. 22, no. 1, pp. 314–323, Feb 2007.
- [27] Bon-Gwan Gu and K. Nam, "A dc link capacitor minimization method through direct capacitor current control," *IEEE Trans. Ind. Appl.*, vol. 42, no. 2, 2006.
- [28] J. Yao, H. Li, and Z. Chen, "An improved control strategy of limiting the dc-link voltage fluctuation for doubly fed induction wind generator," *IEEE Trans. Power Electron.*, vol. 23, no. 3, 2008.
- [29] A. G. Abo-Khalil, "Current injection-based dc-link capacitance estimation using support vector regression," *IET Power Electron.*, vol. 5, pp. 53–58, 2012.
- [30] R. Pena, J. Clare, and G. Asher, "Doubly fed induction generator using back-to-back pwm converters and its application to variable-speed wind-energy generation," *IEE Proc. - Electric Power Appl.*, vol. 143, no. 3, pp. 231–241, 1996.
- [31] R. Datta and V. T. Ranganathan, "A simple position-sensorless algorithm for rotor-side field-oriented control of wound-rotor induction machine," *IEEE Trans. Ind. Electron.*, vol. 48, no. 4, pp. 786–793, 2001.
- [32] S. Arnalte, J. C. Burgos, and J. L. Rodríguez-Amenedo, "Direct torque control of a doubly-fed induction generator for variable speed wind turbines," *Electric Power Components and Systems*, vol. 30, no. 2, pp. 199–216, 2002.

- [33] B. B. Pimple, V. Y. Vekhande, and B. G. Fernandes, "A new direct torque control of doubly-fed induction generator under unbalanced grid voltage," in *2011 Twenty-Sixth Annual IEEE Applied Power Electronics Conference and Exposition (APEC)*, March 2011, pp. 1576–1581.
- [34] Y. Zhang, J. Hu, and J. Zhu, "Three-vectors-based predictive direct power control of the doubly fed induction generator for wind energy applications," *IEEE Transactions on Power Electronics*, vol. 29, no. 7, pp. 3485–3500, July 2014.
- [35] D. Zhi and L. Xu, "Direct power control of dfig with constant switching frequency and improved transient performance," *IEEE Transactions on Energy Conversion*, vol. 22, no. 1, pp. 110–118, March 2007.
- [36] B. Singh and N. K. Swami Naidu, "Direct power control of single vsc-based dfig without rotor position sensor," *IEEE Transactions on Industry Applications*, vol. 50, no. 6, pp. 4152–4163, Nov 2014.
- [37] R. Datta and V. T. Ranganathan, "Decoupled control of active and reactive power for a grid-connected doubly-fed wound rotor induction machine without position sensors," in *Conference Record of the 1999 IEEE Industry Applications Conference. Thirty-Forth IAS Annual Meeting (Cat. No.99CH36370)*, vol. 4, Oct 1999, pp. 2623–2630 vol.4.
- [38] A. B. Ataji, Y. Miura, T. Ise, and H. Tanaka, "Machine parameter independent control of a grid-connected variable speed doubly-fed induction generator for gas engine generation systems," in *2013 IEEE ECCE Asia Downunder*, June 2013, pp. 1348–1354.
- [39] M. T. Abolhassani, P. Niazi, H. A. Toliyat, and P. Enjeti, "A sensorless integrated doubly-fed electric alternator/active filter (idea) for variable speed wind energy system," in *38th IAS Annual Meeting on Conference Record of the Industry Applications Conference, 2003.*, vol. 1, Oct 2003, pp. 507–514 vol.1.
- [40] L. Morel, H. Godfroid, A. Mirzaian, and J. M. Kauffmann, "Double-fed induction machine: converter optimisation and field oriented control without position sensor," *IEE Proceedings - Electric Power Applications*, vol. 145, no. 4, pp. 360–368, July 1998.
- [41] B. Hopfensperger, D. J. Atkinson, and R. A. Lakin, "Stator-flux-oriented control of a doubly-fed induction machine with and without position encoder," *IEE Proceedings - Electric Power Applications*, vol. 147, no. 4, pp. 241–250, July 2000.
- [42] Longya Xu and Wei Cheng, "Torque and reactive power control of a doubly fed induction machine by position sensorless scheme," *IEEE Transactions on Industry Applications*, vol. 31, no. 3, pp. 636–642, May 1995.
- [43] D. Forchetti, G. Garcia, and M. Valla, "Adaptive observer for sensorless control of stand-alone doubly fed induction generator," *IEEE Trans. Ind. Electron.*, vol. 56, no. 10, pp. 4174–4180, 2009.
- [44] G. Marques and D. Sousa, "Air-gap-power-vector-based sensorless method for dfig control without flux estimator," *IEEE Trans. Ind. Electron.*, vol. 58, no. 10, pp. 4717–4726, 2011.
- [45] I. Benlaloui, S. Drid, L. Chrifi-Alaoui, and M. Ouriagli, "Implementation of a new mras speed sensorless vector control of induction machine," *IEEE Transactions on Energy Conversion*, vol. 30, no. 2, pp. 588–595, June 2015.
- [46] V. Verma, M. J. Hossain, T. Saha, and C. Chakraborty, "Performance of mras based speed estimators for grid connected doubly fed induction machines during voltage dips," in *2012 IEEE Power and Energy Society General Meeting*, July 2012, pp. 1–8.

BIBLIOGRAPHY

- [47] G. Iwanski, M. Szyplski, T. Luszczuk, and P. Pura, "Cross and dot product based mras observer of the rotor position of doubly fed induction machine," in *2014 Ninth International Conference on Ecological Vehicles and Renewable Energies (EVER)*, March 2014, pp. 1–5.
- [48] G. Marques, V. Pires, S. Sousa, and D. Sousa, "A dfig sensorless rotor-position detector based on a hysteresis controller," *IEEE Trans. Energy Convers.*, vol. 26, no. 1, pp. 9–17, 2011.
- [49] S. M. Gadoue, D. Giaouris, and J. W. Finch, "Mras sensorless vector control of an induction motor using new sliding-mode and fuzzy-logic adaptation mechanisms," *IEEE Transactions on Energy Conversion*, vol. 25, no. 2, pp. 394–402, June 2010.
- [50] Cardenas, R., Pena, R., Clare, J., Asher, G., and Proboste, J., "Mras observers for sensorless control of doubly-fed induction generators," *IEEE Trans. Power Electron.*, vol. 23, no. 3, pp. 1075–1084, 2008.
- [51] W. Cheng and L. Xu, "Torque and reactive power control of a doubly-fed induction machine by position sensorless scheme," in *Industry Applications Society Annual Meeting, 1994., Conference Record of the 1994 IEEE*, 1994, pp. 496–502 vol.1.
- [52] L. Morel, H. Godfroid, A. Mirzaian, and J.-M. Kauffmann, "Double-fed induction machine: converter optimisation and field oriented control without position sensor," *IEE Proc. - Electric Power Appl.*, vol. 145, no. 4, pp. 360–368, 1998.
- [53] R. Cardenas, R. Pena, S. Alepuz, and G. Asher, "Overview of control systems for the operation of dfigs in wind energy applications," *IEEE Trans. Ind. Electron.*, vol. 60, no. 7, pp. 2776–2798, July 2013.
- [54] M. Pattnaik and D. Kastha, "Comparison of mras based speed estimation methods for a stand alone doubly fed induction generator," in *Energy, Automation, and Signal (ICEAS), 2011 International Conference on*, 2011, pp. 1–6.
- [55] F. Dezza, G. Foglia, M. Iacchetti, and R. Perini, "An mras observer for sensorless dfim drives with direct estimation of the torque and flux rotor current components," *IEEE Trans. Power Electron.*, vol. 27, no. 5, pp. 2576–2584, 2012.
- [56] G. Marques and D. Sousa, "New sensorless rotor position estimator of a dfig based on torque calculations-stability study," *IEEE Trans. Energy Convers.*, vol. 27, no. 1, pp. 196–203, 2012.
- [57] G. Marques, D. Sousa, and M. Iacchetti, "An open-loop sensorless slip position estimator of a dfim based on air-gap active power calculations-sensitivity study," *IEEE Trans. Energy Convers.*, vol. 28, no. 4, pp. 959–968, 2013.
- [58] G. Marques and D. Sousa, "Sensorless direct slip position estimator of a dfim based on the air gap pq vector-sensitivity study," *IEEE Trans. Ind. Electron.*, vol. 60, no. 6, pp. 2442–2450, 2013.
- [59] Pena, R., Clare, J.C., and Asher, G.M., "A doubly fed induction generator using back-to-back pwm converters supplying an isolated load from a variable speed wind turbine," *IEE Proc. - Electric Power Appl.*, vol. 143, no. 5, pp. 380–387, 1996.
- [60] M. Gopal, *Digital Control and State Variable Methods: Conventional and Neural-fuzzy Control Systems Front Cover.* Tata McGraw-Hill, New Delhi, 2003.
- [61] G.-R. Duan and H.-H. Yu, *LMIs in control systems analysis, design and applications.* Taylor and francis group, New York, USA, 2013.

- [62] A. B. Ataji, Y. Miura, T. Ise, and H. Tanaka, "Direct voltage control with slip angle estimation to extend the range of supported asymmetric loads for stand-alone dfig," *IEEE Transactions on Power Electronics*, vol. 31, no. 2, pp. 1015–1025, Feb 2016.
- [63] I. Perez, J. Silva, E. Yuz, and R. Carrasco, "Experimental sensorless vector control performance of a dfig based on an extended kalman filter," in *IECON 2012 - 38th Annual Conference on IEEE Industrial Electronics Society*, 2012, pp. 1786–1792.
- [64] J.K. Sethi, D. Deb, and M. Malakar, "Modeling of a wind turbine farm in presence of wake interactions," *2011 Int. Conf. Energy Automation Signal (ICEAS)*, pp. 1–6, 2011.
- [65] J. F. Manwell, J. G. McGowan, and A. L. Rogers, "Wind energy explained: Theory, design and application". John Wiley and Sons Ltd., UK, 2004.
- [66] R. Vepa, "Nonlinear, optimal control of a wind turbine generator," *IEEE Trans. Energy Convers.*, vol. 26, no. 2, pp. 468–478, 2011.
- [67] Salman S. K. and Teo A. L. J., "Wind mill modeling consideration and factors influencing the stability of a grid connected wind power based embedded generator," *IEEE Trans. Power Syst.*, vol. 18, no. 2, pp. 793–802, 2003.



Curriculum Vitae

Mridul Kanti Malakar

Doctor of Philosophy(Ph.D.): From the Department of Electronics & Electrical Engineering, Indian Institute of Technology Guwahati, India. Thesis submission: October 2019, Cumulative Performance Index(CPI): 7.6/10.

M.Tech: In Power Electronics and Drives (Under Electrical Engineering Department), National Institute of Technology Agartala, India. Year of completion 2010. Cumulative Performance Index(CPI): 8.5/10

B.Tech: In Electrical Engineering, National Institute of Technology Agartala, India. Year of completion 2008. Cumulative Performance Index(CPI): 67.18%

Conference Proceedings:

1. M. K. Malakar and P. Tripathy, "Review on Wind Power Generation With Doubly Fed Induction Generator" in Power Systems Conference(NPSC), 2014 Eighteenth National, Dec 2012,.
2. M. K. Malakar, P. Tripathy, and S. Krishnaswamy, "State estimation of DFIG using extended kalman filter with an augmented state model" in Power Systems Conference(NPSC), 2014 Eighteenth National, Dec 2014, pp.1–6.
3. M. K. Malakar, P. Tripathy, and S. Krishnaswamy, "A predictor-corrector based rotor slip position estimation technique for a DFIG" 2017 7th International Conference on Power Systems (ICPS), Dec 2017, pp 424-429.

Manuscript Communicated:

1. M. K. Malakar, P. Tripathy, and S. Krishnaswamy, "Robust Slip Position and Speed Observer for Sensorless Operation of a DFIG: An LMI Approach" IEEE Trans. Sustain. Energy.
2. M. K. Malakar, P. Tripathy, and S. Krishnaswamy, "Robust slip angle and speed estimation technique using measured rotor currents for sensorless operation of a standalone DFIG system" IET Renew. Power Gener.

